Rapid Orthophoto Development System

Prepared by:
Charles Toth
and
Dorota A. Grejner-Brzezinska

Prepared for:
The Ohio Department of Transportation,
Office of Statewide Planning & Research

State Job Number 134414

June 2013

Final Report

Technical Report Documentation Page

1. Report No.	2. Government Accession No.	3. Recipient's Catalog No.
FHWA/OH-2013/6		

4. Title and Subtitle	5. Report Date
Rapid Orthophoto Development System	**June 2013**
	6. Performing Organization Code

7. Author(s)	8. Performing Organization Report No.
Charles Toth **Dorota A. Grejner-Brzezinska**	

9. Performing Organization Name and Address	10. Work Unit No. (TRAIS)
Center for Mapping **Department of Civil and Environmental and Geodetic Engineering** **The Ohio State University** **470 Hitchcock Hall** **2070 Neil Avenue, Columbus, OH 43210-1275**	11. Contract or Grant No. **SJN 134414**

12. Sponsoring Agency Name and Address	13. Type of Report and Period Covered
Ohio Department of Transportation **Research Section** **1980 West Broad St., MS 3280** **Columbus, OH 43223**	**Final Report**
	14. Sponsoring Agency Code

15. Supplementary Notes

16. Abstract

The DMC system procured in the project represented state-of-the-art, large-format digital aerial camera systems at the start of project. DMC is based on the frame camera model, and to achieve large ground coverage with high spatial resolution, the output image is formed from four independent images acquired by four cameras. DMC procured for OCMS was carefully tested to assess its performance level. From test flights by ODOT, three different blocks were selected, representing different flying condition and flight geometry. Five methods were used for the performance evaluation, including two methods where self-calibration was also introduced. The analysis of the results confirmed that the DMC meets the manufacturer's specification. To maintain consistent performance in normal operations, periodical calibration flights and the use of ground controls as check points is highly recommended. In addition to further support QA/QC, the use of automated aerial triangulation is also suggested.

The main product of the ODOT Office of Mapping and CADD Services is orthophoto, which is widely used in many applications at ODOT and other State offices. Since ODOT primarily acquires data over the transportation network, the orthophoto production has some specific needs, such as dealing with bridges and occlusions, besides the general tasks of the orthoimage workflow. In this project, an innovative method was developed to support the orthoimage generation at bridges. The concept is built around the development of a precise bridge model, which is formed from the DMC imagery and LiDAR data. In addition, a true orthophoto generation process was implemented. The initial versions of both software tools installed at Office of CADD and Mapping Services for testing provided valuable feedback for algorithmic refinements.

17. Key Words	18. Distribution Statement
Large-format digital aerial camera systems, camera calibration, performance evaluation, orthoimage production, LiDAR, precise bridge model	**No restrictions. This document is available to the public through the National Technical Information Service, Springfield, Virginia 22161**

19. Security Classif. (of this report)	20. Security Classif. (of this page)	21. No. of Pages	22. Price
Unclassified	**Unclassified**	**104**	

Form DOT F 1700.7 (8-72) **Reproduction of completed pages authorized**

Rapid Orthophoto Development System

Prepared by:
Charles Toth
and
Dorota A. Grejner-Brzezinska
of The Ohio State University

June 2013

Prepared in cooperation with the Ohio Department of Transportation
and the U.S. Department of Transportation, Federal Highway Administration

Acknowledgments

The authors thank the staff of the ODOT Office of CADD and Mapping Services for their contributions to this project. In particular, we want to express our gratitude to Rachel Lewis and John Ray, Administrators, Office of CADD and Mapping Services, respectively for their continuing support and coordination of the system acquisition and the field testing. The authors greatly appreciate the support of Susana Kroman for her sharing her experiences and collaboration on the interface design and implementation.

Contents

List of Figures

List of Tables

1. INTRODUCTION

In recent years, orthophoto products have become the standard for almost any mapping deliverables. Their phenomenal success is due to the fact that they combine mapping performance with image representation. In other words, an orthoimage has the map scale and orientation, as well as accuracy attributes of a conventional map, but instead of cartographic symbols, it uses images to describe the object space. In fact, orthophotos are so popular, that there is hardly any mapping product in current practice that would not come, at least, with a basic ortho background image. For example, most GIS and conventional vector data are customarily supplemented with an ortho layer, which provides a tremendous help for professional as well as novice users. Similarly, LiDAR data, the predominant technology for terrain surface extraction, are also frequently complemented with a basic background ortho image, which greatly aids most of the data interpretation, since LiDAR data lack the visual information.

Besides their obvious visual attractiveness, orthophotos have several other advantages. Most importantly, their production can be automated to a large extent; an entry level quality orthophoto can be created with practically no human intervention. The other main advantage of orthophotos is that they can be produced in rather short time. In fact, it is technically feasible to create orthos in near real-time; note that it is practically neither needed in most applications nor affordable in civilian mapping. To exploit the benefits of automated and fast production, however, there is one condition: the mapping system should be entirely digital. In other words, all the system components, including data acquisition, georeferencing, and various data processing tasks, should be based on digital implementation, such as using digital cameras and softcopy workstations.

The Office of CADD and Mapping Services (OCMS) has been producing orthophotos for a long time. The aerial imagery is acquired by a Jena LMK large format film-based aerial camera; although a medium format digital camera is also available, but it is mainly used as a companion sensor for the Optech 30/70 LiDAR system. The processing environment in the OCMS office is reasonably up-to-date; there is a strong hardware base, powerful PC-based workstations with massive processing capabilities, and a state-of-the-art softcopy system, which provides all the basic capabilities needed for map production, including orthoimage production. Obviously, the staff with many years of experiences has the expertise to cover every step of creating orthos. Reviewing the status of the overall orthophoto production in the OCMS office, the bottleneck of further improvement in the efficiency is clearly the lack of a high performance optical image sensor.

The objective of this proposal is to recommend an update, including hardware and software components, for the OCMS mapping system that would result in significant improvement of the orthophoto production. A key element of the proposed system is a large-format digital aerial camera, which is an absolute necessity to achieve better production efficiency, measured in terms of shortened delivery time and reduced operational cost. Since the images produced by a digital camera have quite different characteristics, as compared to the film-based camera system, the whole office processing practice should be reevaluated and adjustments should be made. The implementation of both components, hardware and software, is equally essential to bring the

OCMS orthophoto production capabilities to the state-of-the-art. It is important to note that besides the substantially improved orthophoto production capabilities, most of the other mapping capabilities will benefit from the new system in terms of enhancing products and reducing cost. An important aspect of the digital sensor is the significant improvement in image quality, which is demonstrated by better processing performance and superior visualization.

2. RESEARCH OBJECTIVES

The ultimate objective of the proposed research is to introduce to the OCMS an entirely digital map production technology, which will primarily serve the growing needs of the OCMS clientele for rapid orthophoto products, but additionally, it will enhance the general mapping capabilities within OCMS. The totally digital design is a precondition for achieving the secondary objective of the research effort, the competence in delivering ortho products in a timely manner, which is defined in hours compared to weeks, which is the current practice in the OCMS. The entirely digital mapping system will allow for 1) the elimination of time-consuming and labor-intensive tasks that are associated with analog system components, 2) fast data transfer between the major processing units, and 3) high level automation of various processes, all needed to achieve an efficient orthophoto production.

1. Studying the current practice of orthophoto production in the OCMS. This is necessary to identify the critical steps, which are either time-consuming or problematic in terms of efficiency, such as the low level of automation that demands excessive operator involvement, which increases both delivery time and cost.

2. Digital camera procurement. Since the Jena LMK analog large-format film-based camera represents the last non-digital component of the OCMS mapping technology, the most important task is to identify a high-performance large-format digital aerial camera that should be acquired for OCMS. It is important to note that a digital camera is not just a single replacement for the old analog camera, as it does outperform the old system in a significant way that will be discussed at detail later. From the two basic types of digital camera solutions, frame and line scanners, frame camera was selected for the OCMS, as line cameras, such as three-line scanners are not likely to consistently meet the stringent requirements for high-accuracy large-scale mapping products.

3. GPS/IMU-based georeferencing. In recent years, sensor positioning and attitude determination systems have become the primary tools for airborne image sensor orientation. Most importantly, they provide a fast and direct way to obtain airborne platform orientation under almost any condition, and represent a cost-effective solution to the ground control point-based aerial triangulation. Although, a GPS/IMU-based georeferencing is not strictly required for a frame-based digital camera, yet the economic benefits are so substantial that the acquisition of a GPS/IMU-based georeferencing system to integrate it with the digital camera on the hardware level was not a choice but a necessity.

4. Digital camera configuration. Based on points (2) and (3), the actual digital camera configuration was developed based on the specifics of the OCMS production needs. The considerations took into account the flight planning parameters, including flying height, ground coverage and resolution (GSD), image overlap, consistency with the LiDAR operations; and product requirements, such as image specifics mapping accuracy.

5. Orthoproduction workflow development. The proper composition of the various building blocks of the orthoimage generation process is essential to achieve both fast delivery and accurate products at an acceptable cost. Although, the OCMS has a significant expertise is orthophoto production, which is based on the Intergraph softcopy system, due to the past data characteristics, such as dodged analog imagery, only a subset of the complete ortho functionality has been used. With the introduction of the direct digital imagery, however, there was a need to use all the tools in the Intergraph softcopy ortho environment. For example, the better radiometric behavior of the direct digital imagery certainly require color-balancing to achieve a seamless image tone of the composite image. In addition, there are several ODOT OCMS-specific application conditions that require additional processing capabilities to achieve a better performance; basically, functions dedicated to the specific data processing requirements of OCMS do reduce the operator's involvement, resulting in lower cost and faster delivery. Based on the available information, two tasks were identified and implemented as add-on tools to the existing systems, as discussed next.

6. Limitation of the occlusion effect in orthoimagery. Occlusions, in general, are difficult to handle in mapping, and orthophoto production is certainly no exception. In particular, this problem is severe in large scale applications, where the extent of the occlusion is relatively high to the object distance, which is measured from the camera. The visible effect is the dark gaps in the output product. This problem can be mitigated by proper algorithmic design, which does not follow the standard sequential generation pattern (row by row of the DEM matrix), but instead, starting from the nadir position, the orthoimage is created in a spiral fashion that is less subject to occlusions due to the always "looking outward from the inside" approach. The implementation of this technique is feasible as a stand-alone utility or in cooperation with some of the software vendors that supply softcopy technology to OCMS.

7. Treatment of bridges. By the specific application field of OCMS, the most troublesome objects with respect to automated mapping are bridges. For example, LiDAR data can easily cover the surface of the bridge and pick up points under the bridge, which can cause problems for any algorithm that are not specifically designed to avoid "double-mapping". Due to their frequency, a dedicated tool has been developed that can better support the operator's work, by substantially reducing the editing, and thus, resulting in important cost savings. Similarly, to point (6), the implementation of this function is feasible as a stand-alone utility or in cooperation with some of the software vendors that supply softcopy technology to OCMS.

8. QA/QC processes. Although OCMS has a strong desire to implement strict QA/QC processes, the current practice is exclusively operator-based, which means that it is time-consuming and subject to individual factors. Therefore, implementing tools in the fast orthophoto production that can relieve the operator's involvement was essential for product validation purposes.

9. Testing and performance optimization. An extensive testing, in close collaboration with the OCMS, was needed for validation and performance optimization of the developed tools, and the overall rapid orthophoto production technology. First, the digital camera was tested, which was executed by the vendor, and subsequently checked by the OCMS and OSU experts. Then, additional flights included dedicated missions to acquire reference imagery taken over a test range, such as the ODOT-maintained Madison test field. The algorithm was refined and the workflow modified as needed during this effort.

10. Preparing detailed report, operation workflow, and user manual for the developed workflow, algorithms and software utilities.

The above tasks include a balanced amount of algorithmic research, initial implementation, testing, data analysis (data acquisition by ODOT), software developments and technical report preparation. Most of the algorithmic developments were implemented in the Matlab environment, while some deliverable programs was also compiled with Microsoft Visual C++ on the Windows platform. The format of DEM data considers both conventional representation as well as the LiDAR data exchange format, i.e., the industry standard LAS format. The latter one is important for rapid production, as LiDAR data are frequently acquired simultaneously with the imagery.

3. GENERAL DESCRIPTION OF RESEARCH, BACKGROUND

The introduction of metric quality digital aerial cameras at the beginning of the new millennium completed the decade-long transition process of moving from analog to a totally digital technology in airborne surveying. To approach and, eventually, to surpass the high performance of analog cameras was a difficult task, as these aerial cameras were absolutely perfected masterpieces of their class. Despite the rapid acceptance of the new technology, a long conversion period is expected before large-format metric digital cameras will finally dominate the airborne market, due primarily to a large installed base of film cameras that are expected to be used along with the new digital camera systems. The fundamental difference between analog and digital cameras is that a solid-state sensor, rigidly installed in the camera focal-plane, replaces the film (Toth, 2004). The first large-format digital aerial cameras were introduced at the ISPSR Congress in Amsterdam in 2000. However, the actual acceptance in production took a significant time, and, in fact, the transition time ended at the ISPSR Congress in 2004, at which time the digital camera systems have established themselves as a proven and productive technology. In the following, the relevant features of the digital cameras with respect to the film-

based systems will be discussed, which is essential for selecting the right camera system for the rapid orthoimage production system, and to understand the implications on the office processing.

Test data were collected in suburban tree-covered environments of Columbus, Ohio and in dense forestry areas of Wayne National Forest in Athens County, Ohio. Figure 3.2 shows an example data collection environment in the Wayne National Forest.

3.1 Imaging Sensors Used in Digital Cameras

The photo or imaging sensor of a digital camera is typically a CCD (Charge-Coupled Device) or a CMOS (Complementary Metal-Oxide Semiconductor) chip. Both solid-state devices can convert light into electrons that can be easily measured, resulting in a radiometric intensity value. Sensor arrays are built by arranging individual sensor elements, pixels (picture elements), into rectangular or linear formats on a silicon base. All the medium- and large-format aerial digital camera systems are currently based on CCD sensors. The performance gap between the two technologies, however, is rapidly closing.

CCD, the most common type of imaging sensors, captures the light using individual photo-diode sensors. The photons that strike the sensor are converted to a near equal number of electrons, which are then stored in the individual sensor cells. During the read-out process the stored electrons, the accumulated charges, are read electronically. The charge content of each pixel in a line is shifted through the other pixels toward the outside of the array. At each step the charge reaching the end of the line is converted to a digital value. In contrast, for CMOS sensors, the conversion of the accumulated charges from analog to digital is done within the individual image sensor element. Consequently, it is possible to randomly read the values of the individual sensor cells. The manufacturing of CCD chips is an especially complex process, as very high charge transfer efficiency should be achieved. For example, a 0.99999 value results in less than a 5% loss in the charge during its travel through a 4,096 pixel row. On the contrary, CMOS chips are produced by traditional manufacturing technologies that are widely used for microprocessor and memory mass production. The differences in the manufacturing technologies result in obvious differences between CCD and CMOS sensors. The important dissimilarities currently are: 1) CCD sensors tend to produce high-quality, low-noise images, while CMOS is still more susceptible to noise, 2) CMOS sensors are less sensitive, as their sensing area is smaller (0.5 vs. 0.9 fill factor – the actual sensing area of a pixel), 3) CMOS uses significantly less power than a CCD, and 4) CCD sensors have been produced for a long time and thus have higher image resolution, while CMOS is relatively new and still rapidly evolving. In fact, CMOS promises to deliver better performance (including very low noise) at a lower cost.

3.2 Imaging Sensor Parameters

The characterization of the solid-state focal plane imaging sensors is very different from the film. For example, instead of grain size and speed, there are pixel size, number of pixels, and spectral sensitivity of the data sheet. CCD/CMOS sensors are comprised of thousands of pixels grouped in either a linear or matrix array to record the light intensity of each point in a scene. The first sensor parameter is the number of pixels, which is usually defined in rows and columns and usually expressed in megapixels [MP]. Pixel size, measured in microns, with a typical range of

5-15 microns, is another important parameter, which is usually correlated to sensor sensitivity, optical resolving power, and image noise. The physical size of the sensor, which defines the pixel size and the number of pixels, depends primarily on the manufacturing process (the diameter of the silicon bar, which reflects the semiconductor production technology level). For a given wafer size, there is a trade-off between the pixel size and the number of pixels. The smaller the pixel size, the larger the number of pixels that can be integrated onto the chip. However, with shrinking pixel size the number of photons striking a pixel will decrease to the point that noise will become a serious problem. In addition, approaching smaller pixel sizes will lead to diffraction effects. In contrast, a larger pixel size results in low noise image and faster exposure times, but has a negative effect on optical resolution (discussed later). Increasing the number of pixels presents a manufacturing challenge, as more elements are implemented on the silicon wafer, the higher the chance for defunct or improperly functioning pixels.

Both CMOS and CCD sensors are constructed from silicon, and thus have a comparable light sensitivity over the visible and near-infrared spectrum, as both convert incident light into electronic charge by the same photo-conversion process. The typical spectral sensitivity of a CCD is different from that of a simple silicon photodiode, as certain structures built for charge transfer absorb shorter wavelengths, resulting in a slightly decreased blue sensitivity. Using back-illuminated CCDs, where the light falls on the back of the CCD has, a very thin (about 10-15 microns) transparent silicon layer covering the pixels, can almost totally eliminate the channel-related absorption effects and the sensitivity approaches 100%.

The CCD sensitivity has a linear characteristic (radiometric); the amount of photons striking the surface of a pixel is converted to electrons, which are then measured during the read-out process. This is very different from how the human eye senses light intensity or how film converts light intensity, as both have a logarithmic characteristic. The sensitivity of film is measured in optical density, OD. A CCD with an 8-bit output, 256 intensity levels, can cover an OD range of 0-2.4, provided that the noise is smaller than the least significant bit. A 12-bit output CCD, typical in high-end systems, can cover the range of 0-3.6, provided again that the image noise is small enough – a condition difficult to achieve. Experiences obtained by scanning film have shown that typically only 6 or 7 bits represent significant radiometric information (0-1.8, 0-2.1 OD range). Therefore, the 10-12 bit CCD sensors represent a higher dynamic range with excellent radiometric performance with respect to film. However, it is important to point out that with respect to the OD scale, the bits are very unevenly used (the logarithmic characteristic). For instance, for the 12-bit case, only 10 vs. 3,686 levels are used to cover the first and last OD range, respectively. For that reason, selecting the proper exposure time is very critical for CCD sensors, as it is easy to over- and under-expose images.

3.3 Color Image Formation

There are several solutions to obtain color or multispectral information with CCD sensors. In most cases, an optical filter is placed between the incoming light and the CCD sensor; either putting a thin filter layer directly on the surface of the pixels or placing the filter in the optical system of the digital camera. The use of color filters results in reduced intensity in both cases, except for the latter. The five typical solutions are:

- The rotating filter wheel was most commonly used in the first systems for remote sensing applications. Color filters were mounted on a fast rotating wheel that was placed in the optical path near the lens system. At typical airspeeds and at about a 2-sec image acquisition rate, a sequence of images could be acquired with about 80-90% overlap. Obviously, the images had different exterior orientations and additional processing was required to produce a combined color image product.
- The optical beam splitter with multiple arrays design uses a single optical system, combined with beam splitting optics to project the image on separate CCD sensors. Usually, three spectral bands are separated. The advantage of this solution is that the images are acquired at the very same moment. The minor discrepancies in the alignment of the sensor can be calibrated and the formation of a single color image is simple. A small disadvantage to this solution is that during the beam splitting and filtering the intensity of the light is significantly attenuated.
- The multi-camera head configuration is another multiple array design, except instead of the beam splitter, complete cameras are bundled together. The operation of the cameras is synchronized to provide for simultaneous image acquisition. At the price of the increased hardware cost, these systems offer the flexibility of using different resolution CCDs for the different bands. In a typical solution there is a high-resolution monochrome sensor and three medium resolution sensors for the color bands. Similar to the beam splitting solution, the spatial relationship between the cameras, as well as the individual optical systems, must be calibrated to automate the color image formation process.
- The on-chip color filter layer-based sensor is the most widely used design for conventional photographic color cameras. A thin layer of dye is applied to the pixels of a CCD sensor in a variety of patterns. For example, three filtering layers are arranged in a chess-table format, green filters are in the white positions and the black positions are alternatively covered by blue and red filters. This arrangement, called a Bayer filter, is now available in hardware, so the color formation is a part of the CCD read-out process. It is important to note that by using different filters, the actual spatial resolution is reduced, as the color resolution is disproportionate to the intensity resolution. The mathematical reconstruction of the color information is not perfect, and digital images produced this way suffer from the reduced color resolution in comparison to film images. This color formation can also fail and result in color fringing, Moiré patterns, or false or missing details when pattern spatial frequencies in the scene are of a certain relationship to the sensor array's Nyquist frequency.
- Direct color image sensing is based on the phenomenon that the penetration of the incoming light is dependent on the wavelength; longer wavelengths penetrate deeper. This revolutionary concept, Foveon X3 technology, has been implemented first in a CMOS area sensor, which has three photodetector layers located at different depths. This technique directly measures the colors instead of using filters; all three primary colors are simultaneously captured for every pixel. Thus, the image preserves the original spatial resolution of the sensor and the typical color artifacts associated with the Bayer pattern are eliminated.

3.4 Photogrammetric Processing

There are several characteristics of imagery acquired by digital cameras that are important to understand when direct digital imagery is used in applications. Clearly, the practitioners are primarily concerned with the impact of using CCD/CMOS sensors on the photogrammetric process, as opposed to the intricacies of solid-state technologies. The following discussion provides the relevant aspects of using digital imagery acquired by airborne surveying:

- The optical resolving power of a camera system, characterized by the Modulation Transfer Function (MTF) is probably the most frequently used quantitative measure of image quality of a system. The digital nature of solid-state sensors provides a very simple basis for the traditional lp/mm (line pairs per mm) measure. Simply, at least two pixels are needed to differentiate between two lines, for example, the typical 9-micron pixel size translates into 55 lp/mm (the spatial Nyquist frequency of the CCD sensor). In theory, the neighboring pixels of a solid-state sensor are totally independent and thus it is possible to measure a high and low radiometric value, which would mean about a 100% MTF level. In reality, this is rarely the case, as a larger charge in a cell tends to spill over to neighboring pixels, which in effect is amplified by the large number of shifting charges from pixel to pixel in a line of pixels. There are other sensor-specific characteristics that may further decrease the MTF value of a sensor. In general, the resolving power at about f90=50 lp/mm value compares well with high quality film. Experts believe that at the current technology level, the optimum pixel size is in the 6-9 micron range.
- The production of large area sensors, containing tens of millions of identically behaving sensor elements is a very complex and difficult task. Due to several environmental factors, the manufacturing of a “perfect” sensor is simply impossible. In general, a CCD sensor is considered of high quality if the pixels have a good uniformity, which means that the variations in gain between photodiodes are less than a few percent. In large arrays, there could be totally defunct pixels that produce either zero output or maximum intensity output, no matter what the exposure is (dead or stuck pixels). In very extreme situations, this may lead to totally defunct columns in an array. Manufactures grade their sensors based on the number of inactive pixels. Continuing technological advancements improve the production yield and the relative frequency of totally defunct pixels has steadily decreased. Even for the highest grade CCDs, there is always a small variation in the output signal level for the properly working pixels. In extreme cases, however, this non-uniformity can be severe, such as overly sensitive pixels will produce maximum output or pixels with a reduced gain will produce a low output for a normal exposure. Linear sensors, due to their small numbers of pixels, can be manufactured with high quality, no defunct pixels and with very uniform gain values for all the pixels.
- Since most of the variations in pixel gain are permanent (although minor long-term changes can be expected during the lifetime of a sensor), it is easy to apply corrections to improve the output image quality. The defunct pixels can be mapped out during the initial testing. Based on this list a local interpolation can be performed to create the “missing” pixel values. For the active pixels with very different gain characteristics, individual corrections can be applied, which is usually based on a simple linear model containing

bias and scale factors. After calibration, the correction factors are stored with the location and the raw output signal is scaled during processing.

- The dark current is a very important performance parameter of a solid-state sensor and represents the amount of charge the sensor senses under dark (no light) conditions, where there should be no charge converted by the photodiodes. The source of this charge accumulation is electrons generated by thermal interaction. The amount of dark current (in electron/sec/pixels) can be expressed by an equation, which is based on various physical constants and temperature. The characteristic is non-linear and, for example, changing the sensor temperature from 25°C to 8°C will reduce the dark current by half. The only way to decrease the effect of dark current is either by cooling the sensor or by using a short exposure time. The second solution is preferred for airborne operations, as the faster shutter time has the additional benefit of reducing motion blur.

- Electronic shutter can be implemented on linear and low- and medium-sized area sensors. The basic concept is that there is a secondary pixel array created on the chip that can store and move the charges under some shield. The pixels of the primary layer are always exposed to the incoming light and a drain mechanism is activated to remove the charges from the pixels. During exposure, the draining stops and at the end of the exposure the charges are moved into the secondary layer from where they will be shifted out in the normal way. There are several designs to implement the concept. Unfortunately, the complexity of the extra circuitry currently prohibits the implementation of electronic shutters for larger area arrays. Linear sensors are usually equipped with an electronic shutter.

- Electronic motion compensation can be implemented in high-performance sensors used in airborne applications, provided that the charge transfer direction of the sensor is aligned with the flight direction. CCD arrays with TDI (Time Delay Integration) functionality allow for overlapped exposure and transfer operations. Orienting the sensor, so that the charge transfer direction is opposite to the flying direction, provides an opportunity to form a picture by exposing the pixels for a certain time period between consecutive charge transfers. For example, an image pixel can accumulate light in three positions as it steps through three neighboring pixels. This type of operation requires a good synchronization of the camera and aircraft operations.

From the processing perspective, the photogrammetric preprocessing of digital imagery can be characterized as:

- There are specific corrections that are applied to sensor level digital imagery and they have no equivalent in analog film imagery. These corrections are usually applied right after the data download and are, generally, transparent to the users. The main steps include interpolation for defunct pixels, pixel-based intensity corrections, removal of camera lens distortion, and additional processing steps for multihead camera system, such as virtual image formation from multiple images, color space reconstruction, etc.

- One of the main advantages of the totally digital camera design is that there are no moving parts in the focal plane; the mechanical shutter is practically the only moving part in an area sensor-based system. The rigid connection between the lens assembly and a solid-state sensor means that the interior orientation for all the images remains the same. There is no need for fiducial marks, although they can be easily inserted for legacy workflow compatibility. In fact, all the pixels can be used for interior orientation purposes. For example, at a minimum, pixels at the usual eight fiducial locations can be used, or a reseau pattern of pixels can be used for better spatial modeling. Furthermore, all the pixels can be individually calibrated (obviously an unnecessary extreme in most cases). The reason why any pixel can be easily used as a fiducial point is the extraordinary geometric precision of the CCD/CMOS chips. The manufacturing of pixels on the silicon base requires a sub-micron accuracy mask technology to produce the various circuit elements, therefore, the grid of pixels has a better than a micron accuracy. The only problem that may impact the exceptional geometric parameters of the sensor is that during the various processing steps of manufacturing, the wafer is heated up and cooled down several times and thus the final sensor chip may have warped; there is very limited data available on sensor deformations. An early version of the first 4K by 4K frame CCD, with about 60 mm by 60 mm sensor size, was reported to have less than a 10-micron deviation from flatness. Obviously, if the sensor warping is significant, then it can be calibrated to remove this effect. It is important to note that having an image with a complete interior orientation at the sensor level eliminates the sources of several errors usually associated with analog film, such as film processing, film shrinkage, scanning, and operator measurement errors.

- The options for obtaining the exterior orientation of the frame digital cameras are identical to that of analog cameras, while linear CCD-based airborne scanners, however, require direct georeferencing. Obviously, the use of GPS/IMU-based positioning is advantageous for the frame cameras, too.

- The proper exposure time selection is critical for digital cameras. With their linear characteristic the over- and under-exposure situation can easily result in an unacceptable image quality. This phenomenon has an impact of ortho mosaic formation, as ortho images may require sufficient tone-balancing to improve the visual value. To control exposure time, accurate light intensity information should be obtained from previously recorded images or by using independent light meters. The triggering and event marking of the image exposures are similar to that of the large-format analog aerial cameras, except that the sensor supporting electronics is closely synchronized to the shutter actuator. In general, the shorter the exposure time the smaller the image noise and the less the impact of motion blur, if no forward motion compensation is available. As long as the exposure time is not infinite (i.e., the sensor motion during the exposure time is not negligible to ground pixel size or GSD), image blur is a problem that needs to be addressed to achieve better image quality.

3.5 Digital Camera Systems

There is a large number of various digital camera systems used for airborne surveying and remote sensing. Smaller format systems, with less than 15 MP size, have been widely used for a long time, mainly for terrain and vegetation classification. Medium-format digital cameras are typically equipped with the older 16 MP (4K by 4K) or more recently with 22, 32 and 39 MP sensors and are available from many vendors. This category currently represents the largest segment of the installed airborne digital camera systems. The large-format digital camera systems reflect the state-of-the-art technology and their market share is rapidly growing. They not only approach, but surpass the performance of the large-format film-based aerial cameras. Only the last two categories are discussed. Good reviews of available systems can be found in Petrie (2003, 2004, 2005, 2006, and 2007). Table 1 provides a listing for the commercially leading large-format aerial cameras. Note that the large-format, single head camera systems were not available when the camera procurement investigation was conducted. In Table 1, Yellow marks the selected system, gray shows the two other systems evaluated, and, finally, orange marks the current most sophisticated system (DMC-II).

The large-format digital frame camera systems available at the beginning of the project were based on using multiple-area CCDs to achieve the required large ground coverage. Although the Z/I Imaging DMS and Vexcel UltraCAM systems are based on quite different concepts, they fall into the same category. Here only the DMC solution is briefly discussed, as its camera parameters fall close to the required specification of the RFP. To achieve simultaneous ground coverage of all the camera heads, the camera heads are slightly tilted to cover a distinct ground area. The high-resolution version of the DMC is equipped with four 7K x 4K large area chips and f/4 high performance lenses with a focal length of 120 mm for the panchromatic channel. Special care has been taken to ensure a homogenous and flat response of the MTF over the entire image field of the lenses. The resulting resolution of the system on the ground is >13,000 pixels across track and approximately 8,000 pixels along track. The resulting cross track coverage angle for the system is 74°. The relative position of the camera heads, (a), and the complete camera, (b) are shown in Figure 1.

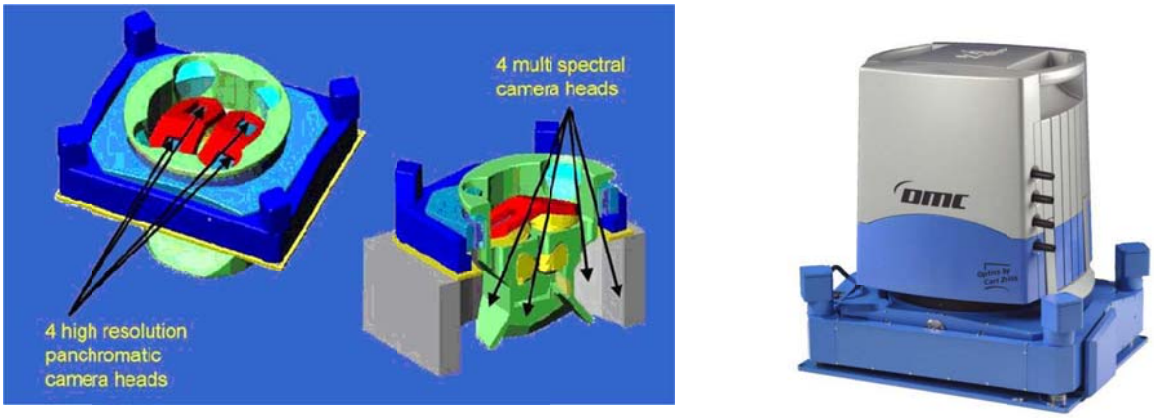

(a) (b)

Figure 1 Concept of eight-head DMC camera system (a), and camera housing (b).

Table 1 Digital camera systems

Large-Format, Single head, Frame Cameras									
System	**CCD**	**Image Size**	**Number of Sensors**	**Pixel Size [micron]**	**Dynamic Range [bits]**	**Maximum Frame Rate [image/sec]**	**FOV**	**GPS/IMU**	**Software**
DMC-II 140/250 Intergraph		12,096 x 11,200 16,768 x 14,016	1 + 4	7.2 5.6	12	0.4	45° x 39°	Optional Integrated	Any system (frame camera model)
SI5 Spectral Instruments		10,580 x 10,560	1	9	16	2	74° x 74°	Optional	Any system (frame camera model)
Large-Format, Multihead, Frame Cameras									
System	**Image Size**	**CCD Sensor Size**	**Number of Sensors**	**Pixel Size [micron]**	**Dynamic Range [bits]**	**Maximum Frame Rate [image/sec]**	**FOV**	**GPS/IMU**	**Software**
DMC Digital Mapping Camera Intergraph Z/I Imaging www.intergraph.com/earthimaging	13,824 x 7,680	7,000 x 4,000 (pan) 3,000 x 2,000 (multispectral)	4 + 4	12	12	2.1	74° x 44°	Optional Integrated	Any system (frame camera model)
*** UltraCam X** Vexcel www.vexcel.com	14,430 x 9,420	5,043 x 3,340	9 + 4	7.2	14	1.3	55° x 37°	Optional Integrated	Any system (frame camera model)
*** DiMAC** DIMAC Systems www.dimacsystems.com	10,500 x 7,200	7,216 x 5,412	2-4	6.8	16	2.1	66° x 48°	Optional Integrated	Any system (frame camera model)
Large-Format, Linescanner Cameras									
System	**Image Size**	**CCD Sensor Size**	**Number of Sensors**	**Pixel Size [micron]**	**Dynamic Range [bits]**	**Maximum Frame Rate [image/sec]**	**FOV**	**GPS/IMU**	**Software**
ADS40 Airborne Digital Sensor Leica GeoSystems http://gi.leica-geosystems.com	12,000 x any	12,000 (2x)	3 + 4	6.5 (3.25)	14	n/a	64°	Mandatory Integrated	GPro ORIMA SOCET SET
*** JAS150** Jena Airborne Scanner Jena-Optronik www.jena-optronik.de	12,000 x any	12,000	5 + 4	6.5	16	n/a	30°	Mandatory Integrated	JenaStereo, SOCET SET
*** 3-DAS-1 and 3-OC** Wehrli Associates www.wehrliassoc.com	8,002 x any	8,002	3 (x3)	9	14	n/a	36°	Mandatory Integrated	Proprietary

3.6 Orthophoto Production

In theory, the production of orthophotos from imagery acquired by digital or analog (film-based) sensors is identical. Besides the digital imagery, two types of information are needed: 1) image metadata, such as orientation (interior and exterior) and camera calibration data, and 2) surface model, such as DEM or simultaneously acquired LiDAR data. Of course, the comparison is quite different if the entire process is considered including data acquisition, in which case, the immediate availability of the direct digital imagery represents tremendous benefits, as it significantly reduces the overall processing time and eliminates several potential error sources. Obviously, there are preprocessing steps for the digital images, discussed above, that do not exist for analog images, but these processes are fully automated and their execution time is practically negligible. Clearly, rapid orthophoto production is only feasible with direct digital imagery.

One difference in image quality that has an effect on the orthophoto generation process, however, should be discussed in detail. As described earlier, the digital imaging sensor has linear characteristic and a significantly better radiometric resolution. This is, in general, advantageous for automated processing, as better intensity information can be exploited during matching, such as tie-point matching for automated aerial triangulation or mass point matching for automated DEM generation. However, better resolution also means that small changes in the lighting conditions can be observed in overlapping imagery, even if they were taken close to each other in time. Therefore to achieve a seamless outlook of an orthophoto, created from several orthoimages, adequate attention should be paid to tone-balancing the images around the seam lines. Figure 2 illustrates the striking difference between analog (scanned digital) and direct digital (digital sensor) images.

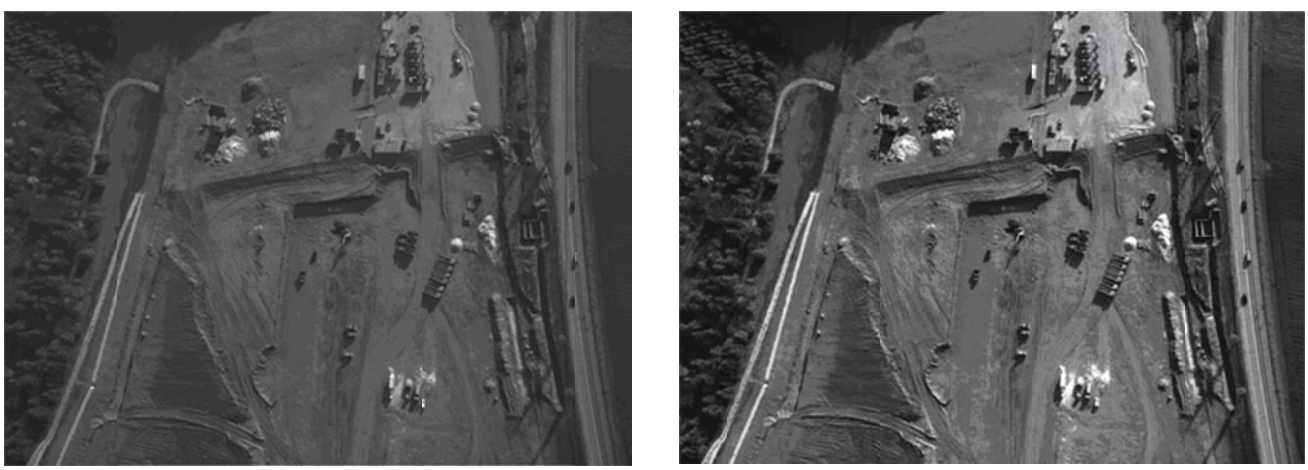

(a) (b)

Figure 2 Analog film scanned (a), and direct digital image (b).

4. DIGITAL CAMERA SYSTEM SELECTION

The success of the Rapid Orthophoto Development Project was of paramount importance, which required The Ohio State University (OSU) to formulate a solution that had the highest probability of success. Beyond this fundamental criterion, OCMS required a long-term solution that maximized the benefit to the State of Ohio. Primary considerations included: digital sensor/camera unit technical specifications, annual maintenance considerations, and pricing for the complete digital camera system.

Telephone interviews were given to current Department of Transportation (Tennessee and Florida) users of the Vexcel Ultra Cam and the Intergraph DMC. A procurement of this magnitude required an evaluation of ownership for each sensor. TDOT is the first DOT to use the Vexcel sensor while FDOT was the first to use the DMC sensor. While both TDOT and FDOT have older versions of the respective sensors, a general impression could be made from their experience. Selection of the digital camera system for the Rapid Orthophoto Development research was determined collectively by OSU, OCMS, and the ODOT Research Section.

4.1 Evaluation of the Digital Sensor/Camera Technical Specifications

Three large format aerial digital camera manufacturers were asked to provide technical specifications and price quotes in response to the ODOT request for proposal (RFP). The following companies were contacted: Intergraph (now Hexagon, as it was bought up by Hexagon), Leica (now Hexagon, as it was bought up by Hexagon), and Vexcel. The suppliers submitted detailed technical specifications to OSU and to the OCMS. The submitted technical specifications were compared to the requirements in the RFP by OSU.

Of the three digital sensor /camera manufacturers, the Intergraph DMC camera and the Vexcel Ultra Cam Xp camera met the requirements specified in the RFP for the digital sensor/camera. The Leica digital camera was eliminated from the selection because the sensor is not frame based, which is a paramount technical requirement of the RFP. The technical specifications of the three camera manufacturers are listed in Table 2.

The Intergraph DMC digital sensor/camera included a complete bundled package that fully met the technical requirements of the RFP. Since, the Vexcel Ultra Cam Xp camera did not include a complete bundled package that met the technical requirements of the RFP, additional third party hardware and software price quotes were required for the GPS/INS subsystem, the gyrostabilized base, and the flight management system for the Ultra Cam Xp camera to fully meet the RFP.

Table 2 Technical specification of the three camera systems.

RFP Technical Requirements	Intergraph DMC	Leica ADS80	Vexcel UltraCamXp
Frame camera model-based sensor	Yes	No	Yes
Gyrostabilized sensor/camera	Included (Z/I)	Included (PAV30)	Third party item; not included (!)
High accuracy GPS/INS subsystem	POS AV 510	IPAS20	Third party item; not included (!)
True color images	RGB (NIR)	RGB (NIR)	RGB (NIR)
Ability to store a minimum of 500 images per mission	1,200 (max)	Yes (pixel carpet!)	6,600 (max)
Ground pixel size of 2 inches at 1,500 ft AGL (nadir)	2.7 cm	4.7 cm	2.7 cm
Cross track image width of at least 2,000 ft	2,072 ft	1,874 ft (!)	1,562 ft (!)
Minimum of 60% overlap at 110 knots airspeed	73% (0.5 FPS)	100% (3-line sensor)	69% (0.5 FPS)

! marks items that needed additional attention, as the parameters may not exactly match the requirements of the RFP

4.2 Annual Maintenance Considerations

Annual maintenance was a consideration for the OCMS. The OCMS required a long-term solution that minimized the "down-time" of the sensor while maximizing the use of public funds. The OCMS reviewed the annual maintenance costs and the annual maintenance requirements for each sensor, see Table 3. Annual maintenance costs were approximated for 6 years of ownership since the first year is included for both systems. This time frame was chosen because this is the anticipated life-span of the GPS/INS subsystem. The Vexcel Ultra Cam Xp sensor requires annual shipment to Graz, Austria for cleaning, inspection, and calibration that was not included in the above cost analysis. According to the documentation, shipping and insurance is incurred by the Customer (i.e.: The State of Ohio) for the annual maintenance. Annual maintenance for the DMC sensor is performed at the Customer's location. According to Intergraph, the sensor was built in modules so it can be easily serviced in the field and only under extreme circumstances would it require shipment to their facility.

Table 3 Annual maintenance.

Annual Maintenance Item Description	Intergraph System (U.S. Dollars)	Vexcel System (U.S. Dollars)
Frame Based Sensor	$60,000 x 5= $300,000	$85,290 x 5 = $426,450
GPS/INS	$27,120 x 5= $135,750	[(($2,250+$17,960) x 2)+(($2,250+$22,450) x 3)) = $114,520
Gyrostablized Base	Included	$10,200 x 5=51,000
Flight Management	Included	Included in GPS/INS
Post Processing Software	$10,104 x 5=50,520	Included
Annual Maintenance Total for 6 years	**$486,120**	**$591,970**

4.3 Camera System Total Price

The total cost of ownership for each sensor over the course of 6 years yielded approximately the same price. Table 4 includes the pricing for the two technically feasible digital sensor/camera systems:

Table 4 Total price of camera system (6 years).

RFP Technical Requirements	Intergraph DMC (US Dollars)	Vexcel UltraCamXp (US Dollars)
Frame camera model-based sensor	$1,291,962	$867,513
Gyrostabilized sensor/camera	Included	$85,750
High accuracy GPS/INS subsystem	Included	$235,675
Flight Management Software	Included	Included in GPS/INS
Approximate Annual Maintenance Cost for 6 years (from above)	$486,120	$591,970
Total Price=	**$1,778,082**	**$1,780,908**

4.4 Department of Transportation Ownership Experience

Telephone interviews were given to TDOT and FDOT by the OCMS on January 23, 2009 to evaluate their experiences with each sensor. Table 5 summarizes the notable findings. In general, both TDOT and FDOT had a positive experience with their respective digital sensors. Some of the above comments are considered subjective, but a common problem identified with these systems appeared to be the hard-drive storage systems of both the Vexcel and DMC sensors.

Table 5 Ownership experiences at DOTs.

TDOT- Vexcel UltraCam Sensor- Ownership Comments
- Sensor was selected mainly because it worked with their current Air-Track system (DMC did not at the time) and it yielded better image resolution at their typical flying height.
- Long processing time required for imagery. Processing requires multiple steps. Not necessarily faster than using film camera.
- Image file sizes are large. Must consider file management (storage) prior to purchase.
- Technical support has been out 3 times to fix data storage/collection system problems.
- Technical support has been responsive. Primary communication/notification is via email.
- Use Intergraph mapping software without any issues.
- Interface in the aircraft is not very intuitive. Does not integrate with the flight planning software as well as they would like.
- Initial training provided by the vendor was “barely functional”
- Moving to a digital format is a good idea.
FDOT- Intergraph DMC Sensor- Ownership Comments
- Annual Maintenance is expensive.

-	There were some initial mount problems.
-	There were some problems with the hard drive data storage.
-	They, "love the imagery" from the sensor.
-	Had minor 3 band misalignment issues in the last 2 years of ownership.
-	Use Inpho mapping software without any issues. Are considering switching back to Intergraph mapping software.
-	Sensor/interface is easy to use in the aircraft.

4.5 Summary of Digital Sensor/Camera Selection

The success of the Rapid Orthophoto Development Project was the primary objective of the digital sensor selection. The primary objective could be met with either the Vexcel Ultra Cam Xp or the Intergraph DMC. However, the ease of implementing a complete bundled package with the Intergraph DMC is highly attractive and it increases the probability of a successful research project within the condensed schedule of the RFP. This is mainly due to the coordination and hardware integration between various (hardware and software) vendors, which would be required with the Vexcel Ultra Cam Xp sensor.

Equally important to the primary objective was the selection of a long-term solution that maximizes the benefit to the State of Ohio. From a cost stand point, the respective systems yield approximately the same cost when evaluated through a 6-year time span. The initial cost favors the Vexcel sensor while the annual maintenance cost favors the DMC sensor. As ownership increases beyond the 6-year time frame, the DMC sensor yields a lower total cost (assuming current value of money).

Annual maintenance is another long-term solution consideration that favors the Intergraph DMC sensor. Annual maintenance is performed at ODOT's facility and it does not require annual shipping to the vendor's facility. The sensor is modular in nature and it is easily serviced in the field. This equates to less down-time for the aircraft, which is the preferred solution.

Interviews with TDOT and FDOT indicated that the hard-drive storage may be a problem for either sensor chosen. However, Intergraph has addressed this by utilizing solid-state storage for the digital images in the most current version of the DMC. This storage system is highly attractive and it is the OCMS preferred long-term solution.

In summary, an increased probability of success was associated with the bundled package offered by the Intergraph DMC for the Rapid Orthophoto Development Project. In addition, the Intergraph DMC offered the most favorable long-term solution for the State of Ohio in the terms of ownership cost, annual maintenance, and addressing known problems with data storage. Therefore, the Intergraph DMC digital sensor/camera system was selected for the Rapid Orthophoto Development System.

The DMC camera was procured and delivered in spring 2009; the PO went out on March 5, 2009. The camera installation, however, suffered delays, as aircraft issues were identified by FAA that required significant work. The DMC camera system became fully operational by the first quarter of 2011.

5. PERFORMANCE VALIDATION OF THE DMC SYSTEM

5.1 Analysis of Expected Performance

ODOT has abundant experience using aerial images and LiDAR data to generate maps and analyze traffic information for the public usage. Clearly, orthophoto is one of the most important products. In practice, the quality of orthophoto could be weaker in areas of complex structures, such as around bridges and vegetation covered areas. In these situations, orthophoto creation requires more manual work to improve the quality of the automatically produced orthoimages. Note that limitations of the orthophoto do come from the hardware side too. Therefore, as part of this project ODOT procured the DMC (Digital Mapping System), one of dominant large format aerial digital camera systems in the world, to acquire better quality aerial images and to transfer the advantages of them into the end product, orthophoto of highway corridors.

From the photogrammetric perspective, a DMC integrated with GPS/IMU airborne mapping system represents and ideal configuration to achieve high quality images for orthophoto production. Obviously, a sensor system must be carefully calibrated to achieve the highest performance. In this section, different photogrammetric approaches devoted to performance evaluation of airborne mapping systems are presented. The factors influencing the precision and accuracy of the results are discussed. A comprehensive evaluation of the performance of the airborne mapping system can provide confidence to high quality orthophoto generation. In addition, typical difficulties in orthophoto production are presented, and, consequently, the solutions are provided.

5.1.1 DMC and GPS/IMU Integrated Mapping System

DMC is one of the most powerful digital large format camera systems. DMC captures simultaneously four high resolution panchromatic images; each is 7000×4000 pixels (across and along the track). A large high resolution panchromatic image (virtual image) of 13824×7680 pixels (across and along track) is generated by the four smaller images, see Figs. 3 and 4. Each pixel is 12μm×12μm and the focal length of each camera head is 120mm. The virtual camera focus length, f is generally freely selectable, but mostly defined to 120mm (Helmut Heier, Michael Kiefner, Wolfgang Zeitler, 2003).

DMC is designed to perform under diverse light conditions with a wide range of exposure times and utilizes electronic forward motion compensation (FMC). Furthermore, the 12-bit-per-pixel radiometric resolution enables better exposure sensitivity, allowing more details to be recorded on the CCD less dependent on the lighting condition, thus increasing the number of flying days considered acceptable and the number of tie points in the post-processing. DMC can also produce small-scale or large scale images with ground sample distance (GSD) fewer than 5cm. The image data that the camera captures is stored on three Flight Data Storage (FDS) units, whose space is large enough to hold data that will produce 2200 final output images. GPS/IMU can be also installed with DMC and DMC system software like Z/I Mission that can assist photogrammetric engineer to make a comprehensive flight plan is regarded as another advantage. Based on these state-of-art technologies integrated in DMC system, DMC is announced by

Intergraph as the industry's most innovative and precise turnkey digital camera system (Dörstel C. , 2005) (Dörstel C. , 2003) (Intergraph, 2008).

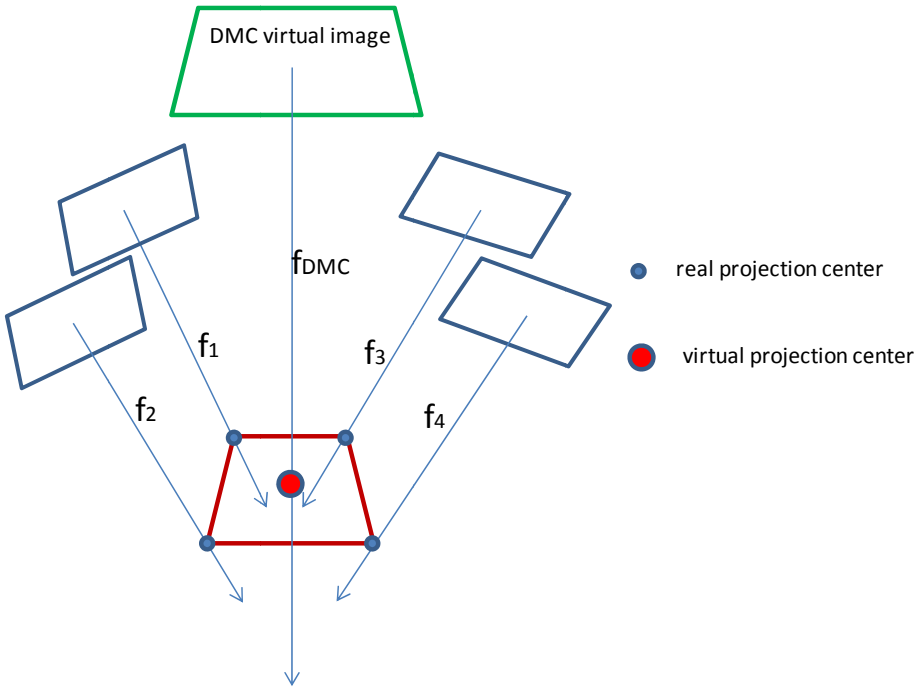

Figure 3 Four panchromatic cameras and virtual DMC image.

Figure 4 Four images and virtual image of DMC.

Features of the DMC system which are important for a photogrammetric project are:

- A complete digital workflow adds precision and efficiency to data capture
- CCD frame sensor technology delivers the best geometric accuracy
- FMC eliminates image blur
- 12-bit per pixel radiometric resolution ensures exceptional image clarity
- Large capacity data storage increase data capture capability
- Extendable with GPS/IMU system on board

GPS can provide highly accurate position information of the plane as well as the camera, while the IMU system can provide the attitude information of the camera. Due to the modest price of GPS/IMU equipment, the high level of workflow automation and the reduced processing time, GPS/IMU systems nowadays are widely applied to Aerial Photogrammetry.

5.1.2 Sensor Orientation Alternatives

Large format aerial digital mapping system integrated with GPS/IMU has challenged the traditional aerial photogrammetry practice due to its advantages of time effectiveness, fewer requirements of the ground control points (GCP) and flexible flight plan. This is because GPS/IMU can directly provide the camera position as well as attitude, which is called direct geo-referencing (DG). The object points are then extrapolated from projection centers of the imaging sensor but not provided from GCPs (called as interpolation).

Without GPS/IMU, the exterior orientation of cameras is always indirectly obtained by using aerial triangulation (AT), and this approach is usually named as indirect geo-referencing (IDG). The essential of AT is to calculate the exterior orientation using the geometric relation between image space and the ground block, and the most widely used method is the bundle block adjustment, which is a very rigorous mathematic model. However, AT requires a number of GCPs and the configuration of the block is critical to ensure the geometric stability of the block. The object points on the ground are also calculated based on GCPs. In practice, the implementation of AT in software, i.e. automatic aerial triangulation (AAT), has more challenges, as difficulties exist in image matching due to textureless areas, such as sand, water and forestry as well as shadow effects, etc. Obviously, it is possible to steer clear of those problems by using DG.

DG and AT are two totally independent approaches for the same purpose, to determine the exterior orientation and the object points on the ground. Interestingly, their different characteristics can compensate each other. For instance, the roll angle is difficult to get but the yaw angle is well known for AT. In contrast, GPS/IMU can provide roll angle but difficult to get yaw. To exploit the complementarity of two approaches, a new model called integrated sensor orientation (ISO) is developed. The basic idea of ISO is to utilize an extended bundle adjustment with involving GPS/IMU data (mostly, only GPS data) to calculate the best solution for the entire model or block. Since GPS/IMU data are also brought in the bundle adjustment, the requirements of GCPs and block configuration can be significantly reduced. Note the GPS/IMU

solution is also estimated in the model, comparison can be done. ISO may improve both accuracy and reliability of the final results, and it is still under research (Jacobsen, 2003) (K.P. Schwarz, N. El-Sheimy, 2004).

Imagery, acquired by the DMC system with the GPS/IMU georeferencing component can be oriented with all the three approaches described above. The accuracy and data collection requirements, however, vary. Most importantly, there is a quite different error characterization between the DG and the two other methods, as the first one has an extrapolation while the others have an interpolation model, respectively, see Fig. 5. Therefore, the system calibration, including sensor calibration and sensor inter-calibration, is of paramount interest, as any calibration errors directly transform into the object point errors. Table 6 shows a comparison of the different approaches.

As a recommendation, ISO is suggested for projects requiring high-accuracy and DR can be applied in less demanding projects.

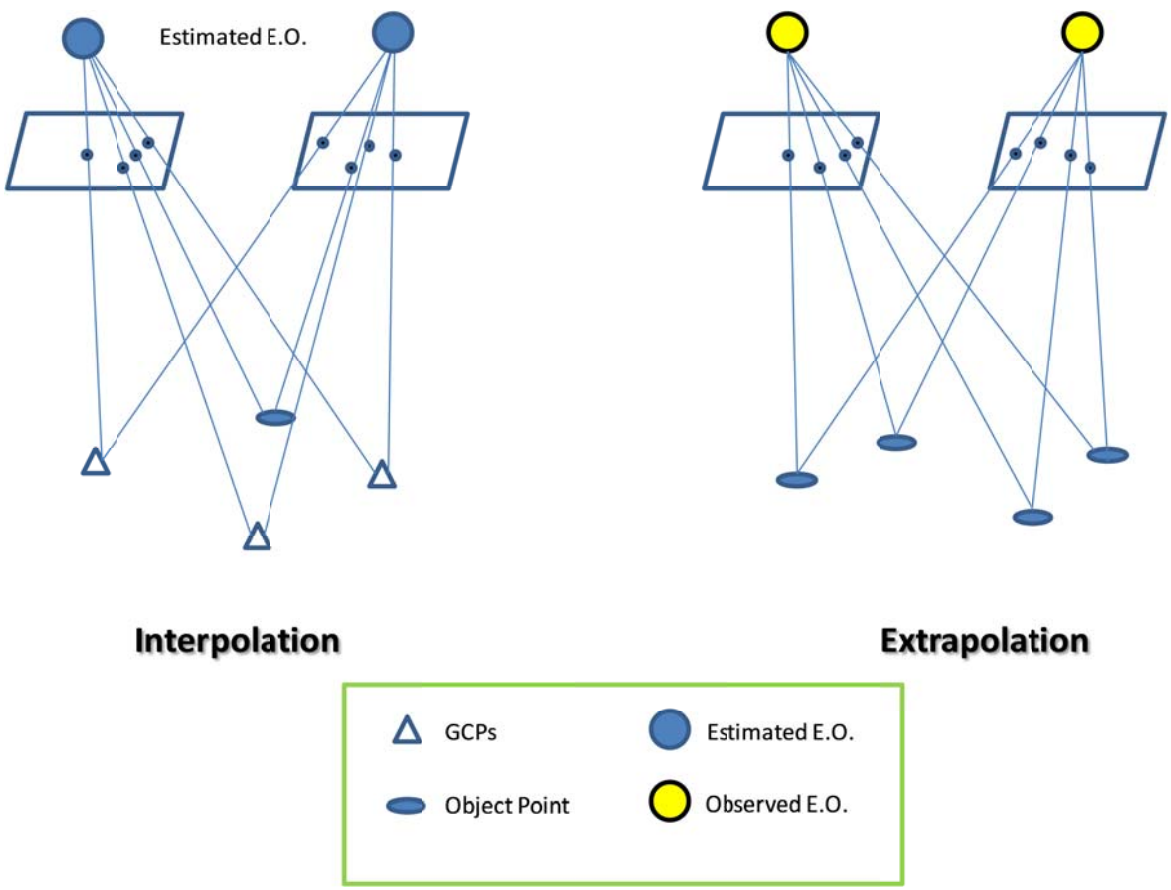

Figure 5 Different error characteristics, IDG: interpolation and DG: extrapolation

Table 6 Comparison of the three orientation methods.

	Direct Georeferencing	Integrated Sensor Orientation	Indirect Georeferencing
Orientation related aspects	a) highly dependent on the sensor performance b) whole system calibration is required	a) less dependency on sensor calibration b) self-calibration of camera is needed c) bundle adjustment	a) very robust process b) self-calibration of camera is needed c) bundle adjustment
IO errors	a) uncompensated b) boresight misalignment	a) compensated due to bundle adjustment	a) compensated due to bundle adjustment
Error characters	extrapolation: GPS/IMU errors directly transfer to object points		interpolation: AT can "absorb" calibration errors
Processing time	short	medium	long
Object accuracy	limited accuracy; no redundancy	best accuracy, not limited by GPS/IMU	best accuracy
GCPs	not needed	not needed/few GCPs	needed
Block formation	not needed, ideal for corridor mapping	not needed	block configuration needed
Generation of orthophoto	sufficient for applications not requiring very high accuracy	adequate for high accuracy orthophoto	standard for high accuracy orthophoto

5.1.3 System Calibration

Sensor calibration is always important for accurate aerial mapping systems, especially if the DG method is used. There have been a number of reports discussing the calibration of DG and ISO systems (Jacobsen, 2003) (Yastikli, 2004) (Yastikli, N.; Jacobsen, K., 2005). Calibration process includes the calibration for every sensor in the integrated system, i.e. camera calibration, and image sensor and GPS/IMU system spatial relationship calibration. More specifically, they are:

- Interior orientation of the imaging sensor (camera calibration)
- The determination of the attitude relation and shifts between the IMU and the imaging sensor (boresight misalignment)
- GPS antenna offsets; lever arm to IMU
- Time synchronization errors

The focal length is generally determined by a laboratory calibration, though it may change under flight conditions. This unexpected variation influences the height precision and accuracy. The focal length may change up to 0.05% depending up on the flying height. In the case of the OEEPE test block (C. Heippke, K. Jacobsen, 2001), the focal length could be determined based on direct sensor orientation from two different height levels with image scales 1:5000 and 1:10000 together with GCPs. Based on Jacobsen's study of the effect, two conclusions are given. First, the change in focal length causes an affine deformation of the photogrammetric model with a changed scale in Z; a 41µ variation was shown and caused a displacement in Z of 1.6cm.

Secondly, if the ground point is determined by DG from a flying height of 1500m, 41μ change of the focal length is resulting in a Z-shift of 40cm, which is quite more than the general accuracy (Jacobsen, 2003).

The attitude and positional relation between the imaging sensor and IMU is known as boresight misalignment which includes three rotations and three shift values. Normally, a reference block with GCPs is used for this calibration. The boresight misalignment will usually be determined by comparison of the GPS/IMU-derived sensor orientation parameters with the results of a reference bundle block adjustment (Yastikli, 2004) (Yastikli, N.; Jacobsen, K., 2005).

5.1.4 Theoretical Accuracy Expectation

From the classic photogrammetric perspective, the 3D position precision of an object is dependent on the image measurement precision, image scale and base-to-height ratio, *b/h*. Since high image measurement precision, such as σ ≤ 0.1 pixel is achievable in AAT, and image scale is normally fixed because certain GSD is required by customers, the effect of *b/h* is investigated.

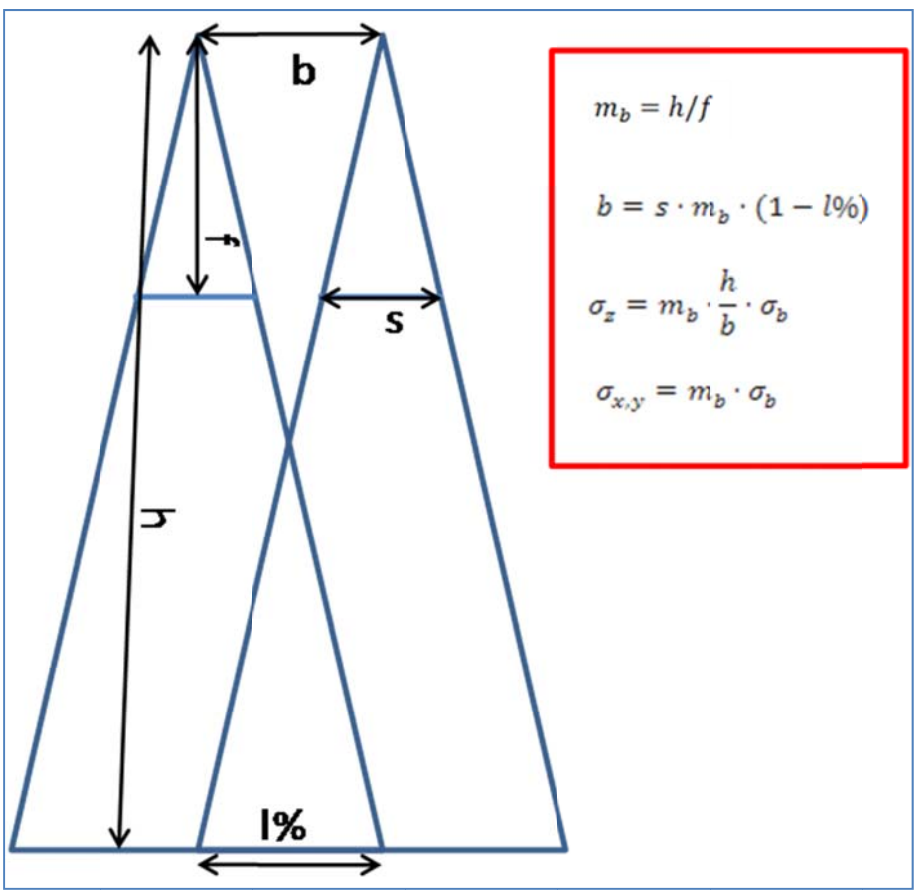

Figure 6 Illustration of geometric relations and precision estimates from two aerial images.

A standard *b/h* of 0.6 overlap is used by analog cameras, while, large format frame-based aerial digital cameras have to reduce their *b/h* due to the design and/or construction restriction. The *b/h*

ratio of 0.31 is not unusual for the DMC. Based on theory, a simple estimation of the precision of a 3D point can be calculated through $\sigma_z = m_b \cdot \frac{Z}{B} \cdot \sigma_b; \sigma_x = \sigma_y = m_b \cdot \sigma_b$, where m_b is the image scale factor, σ_b is the precision of image measurement and *Z/B* is the reciprocal of *b/h*. The baseline B can be calculated through $B = s \cdot m_b \cdot (1 - l\%)$, where s is the image width and $l\%$ is the forward overlap (Kraus, 2004), see Fig. 6.

Obviously, the σ_z is related to *b/h*; a smaller *b/h* leads to a bigger σ_z as well as to a short baseline due to larger overlap, like 90% forward overlap instead of classic 60% forward overlap, can also increase σ_z. R. Alamus et al. used a *b/h* ratio of 0.31 to study the effect on height accuracy and concluded that the deterioration of the height accuracy due to the half *b/h* (e.g., DMC compared to an analogue camera) cannot only be compensated by doubling the image measurement accuracy (R. Alamus, W. Kornus, I. Riesinger, 2007). However, this may be compensated by higher overlap, as Michael Gruber et al. also pointed out that much more tie points with high multi-rays can be generated by using larger forward and side overlap and thus strengthen the geometric stability of the block and to compensate for degradation in height precision (Michael Gruber, Richard Ladstädter, 2008) (YUAN, 2009).

It was also reported by Christoph Dörstel that acceptable 3D point precision was achieved by using *b/h* of 0.3071 to 0.1536 from DMC images (Dörstel C., 2003). All test flights were flown at several altitudes over the test field Elchingen, nearby Aalen, Germany. The AT results are summarized in the Table 7; image block is shown in Fig. 7.

Table 7 Results of Dörstel C. tests using DMC imagery from 2003

Project	Base/Height	Flight Height[m]	Image Scale	Expected Precision [m]			Computed Precision RMS [m]		
				σ_x	σ_y	σ_z	σ_x	σ_y	σ_z
EL4	0.3071	460	1:4000	0.02	0.02	0.023	0.012	0.014	0.018
EL5	0.2688	600	1:5000	0.025	0.025	0.030	0.023	0.025	0.034
EL10	0.1536	1200	1:10000	0.050	0.050	0.060	0.031	0.031	0.043
EL15	0.1536	1800	1:15000	0.075	0.075	0.090	0.041	0.036	0.029

The σ_z can be also simply calculated as $\sigma_z = \pm x\%_0 h_g$; Dörstel used x=0.05 to calculate the expectation height precision.

Comparing to the accuracy of the classic photogrammetric approach to the accuracy of DG should include other characteristics, such as the impact of extrapolation, see Fig. 5. The accuracy of the observed position and attitude from GPS/IMU system, i.e., EO parameters, does also influence the object point accuracy directly. As an example, for the flying height of 1500m and the attitude accuracy from IMU of 0.004 degree and GPS position accuracy of about 5cm, the object position accuracy can be derived as shown in Fig. 8.

.

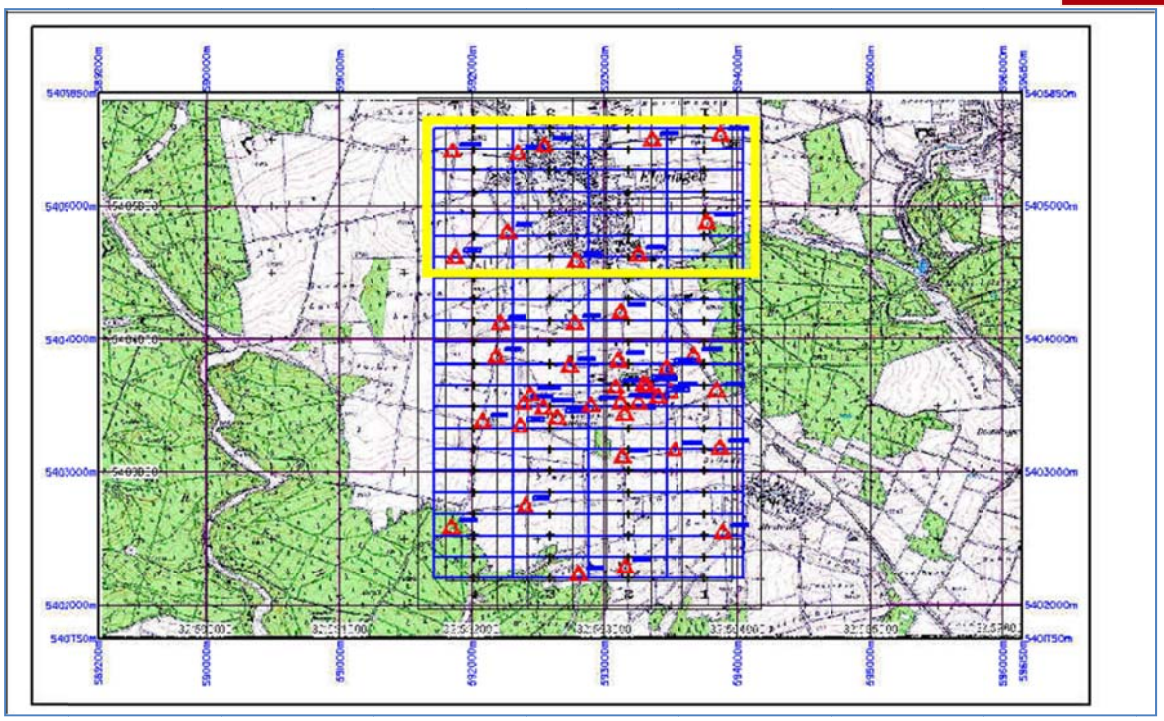

Figure 7 Test field Elchingen with footprints of images at 1:5000/600m AGL (blue) and footprints of images at 1:4000/460 m AGL (yellow). The complete area (blue) was captured by flights at 1200m and 1800m.

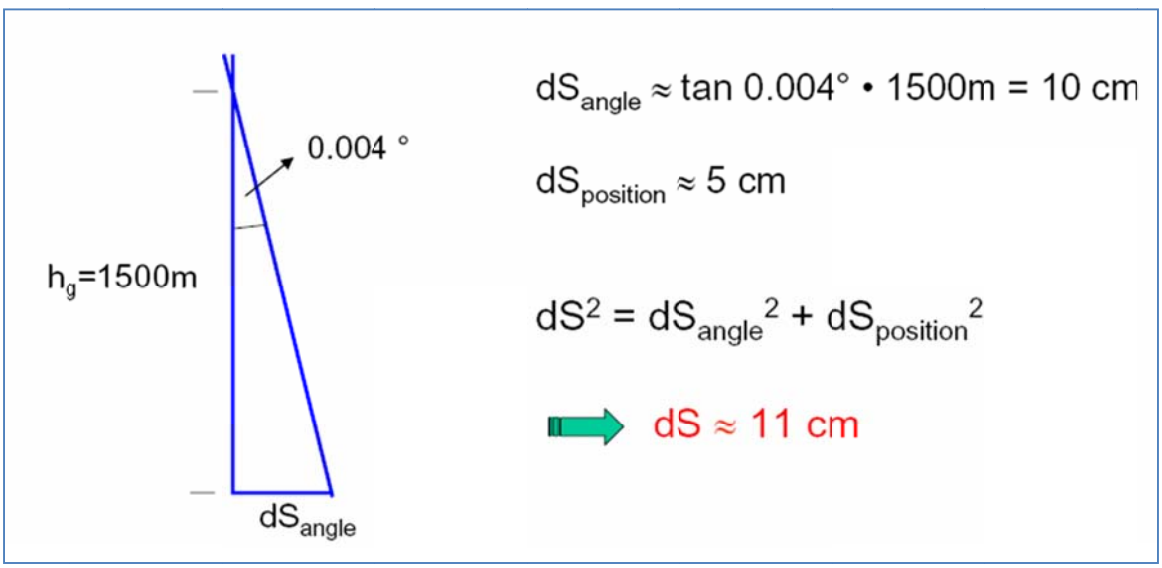

Figure 8 Estimation of object positioning accuracy from the angle- and position accuracies (Kremer, pp. 28).

As GPS/IMU technology matured and became accepted in practice, several well organized investigations on DG and ISO performance have been reported, mostly by academic institutions and organizations since later 1990s, see publication list from the OEEPE-Workshop of "*Integrated Sensor Orientation,*" 2001, and different investigation reports, such as (Michael

Cramer, Norbert Haala, 1999), (Toth, 1999), (Grejner-Brzezinksa, 1999), (Michael Cramer, 2003), (Dahai Guo, Lixin Wu, Qiu Li, Jianchao Wang, Xiongwei Zheng, 2006) (YUAN, 2009), etc.

The 2001 OEEPE (European Organization for Experimental Photogrammetric Research) test showed that the accuracy potential of DG for 1:5000 imagery is approximately 5 – 10cm in planimetry and 10–15cm in height, provided optimal system calibration parameters are used. The accuracy was expressed as RMS values at independent check points. These accuracy numbers are about 2-3 times larger than the numbers from the standard photogrammetric AT (Christian Heipke, Karsten Jacobsen, Helge Wegmann, 2001). Michael Cramer also reported that the accuracy obtained by DG for 1:5500 RMK-Top30 images with non-optimal system calibration in object space is in the range of a few to several decimeters, again, expressed as RMS; especially the vertical component (Michael Cramer, 2003) see Fig. 9.

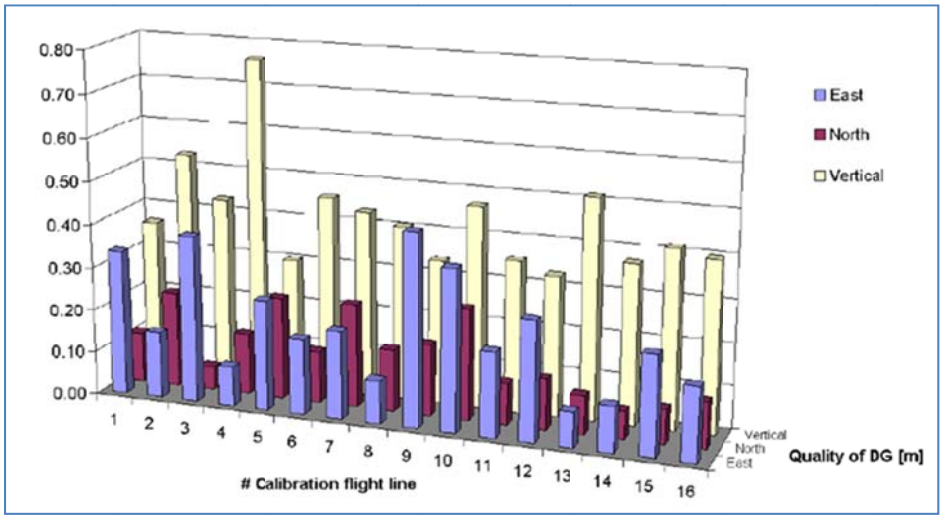

Figure 9 Quality (RMS) of DG based on 16 check points in a strip (Michael Cramer, 2003, pp. 6).

Based on the published performance investigations on DG (in early 2000), it is concluded that the overall system calibration before mission is the most important step for DG. However, the overall system calibration is rather complex, and includes many other components of system and environment. Since a nearly optimal system calibration is difficult to achieve, the standard approach is to introduce GPS/IMU measurements in an extended AT, i.e. ISO. This method allows for the subsequent refinement of systematic errors and will increase the overall accuracy of object points. Michael Cramer gave a typical example of the positive influence of ISO using the same dataset mentioned above. After DG, the presence of remaining systematic errors is obvious from the horizontal and vertical check point differences, see Fig. 10 left. The mean RMS is about 18cm, 12cm and 46cm for east, north and vertical components, respectively and corresponds to the error bars shown in Fig. 9. After performing ISO with only one GCP located in the middle of the corridor, and including additional parameters for the refinement of boresight misalignment and position offsets, the accuracy of object point positioning is increased significantly, see Fig. 10 right. The RMS values from the analysis of 20 check points are about 7cm (east), 9cm (north) and 14cm (vertical).

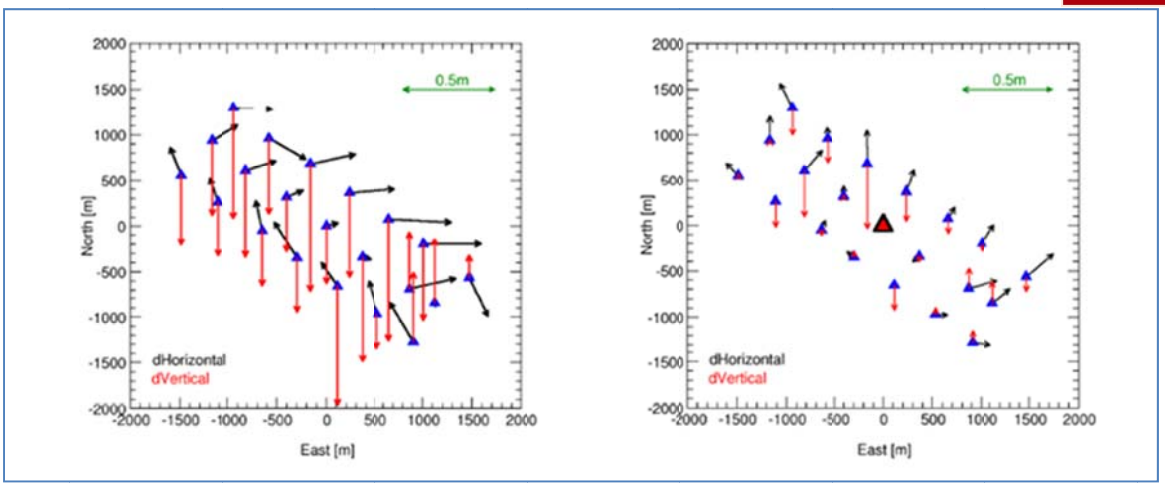

Figure 10 Left: quality (RMS) of DG for one corridor strip; right: quality (RMS) of ISO for one corridor strip (Michael Cramer, 2003, pp. 7).

A comprehensive test of DG using the Leica ADS40 line camera system and three different GPS/IMU systems (IGI AEROcontrol-IID, Applanix LN200/ADC and POS AV 510 – AIMU) were accomplished by the Institute of Photogrammetry at Stuttgart University, Germany, in 2004. The Vaihingen/Enz test area near Stuttgart with 202 well-defined GCPs was used. The flying heights were 500m, 1500m, 2500m and 4000m. The results are listed in the following Table 8.

Table 8 Quality (RMS) of DG at AGL 1500m using different GPS/IMU systems, GSD = 15.6cm.

Direct Geo-Referencing without GCP **Absolute accuracy from 202 independent check points, Leica ADS40**			
GPS/IMU	East RMS [m]	North RMS [m]	Vertical RMS [m]
Applanix LN200/ADC	0.110	0.086	0.158
Applanix POS AV 510/AIMU	0.092	0.097	0.149
IGI AEROcontrol-IId	0.086	0.061	0.098

The lesson learned from this experience is:

- Optimal GPS conditions (GPS accuracy < 10cm)
- Good overall system calibration
- No datum problem (GCPs measured by GPS)

5.1.5 Corridor Project Performance

ODOT plans to use the DMC and GPS/IMU integrated aerial mapping system to acquire high quality images and generate orthophotos with 0.5 feet geometric resolution over highway corridors. Under normal operations, the flying height is about 795m AGL, 80% forward overlap

and 60% side overlap. Since the highway corridor is rather narrow and mostly straight or slowly curving, a single strip or a few strips should be flown. DG is not-sensitive for corridor mapping but the system calibration should be as good as possible, as discussed earlier.

In 1997, ICC performed an accuracy analysis of a corridor mapping project (Guissona), consisting of 42 photos flown in 5 strips at an image scale of 1:5000, see Fig. 11. The DG result from this corridor project is listed in the following Table 9.

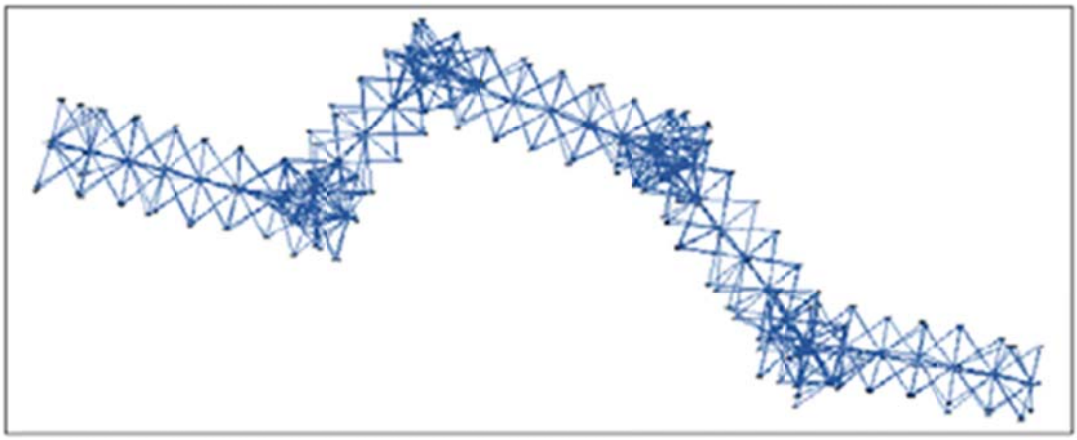

Figure 11 ICC Guissona project, image scale 1:5000 (1997)

Table 9 Quality of DG for a corridor project, ICC, 1997.

Direct Georeferencing by ICC, Spain			
Project	East RMS [m]	North RMS [m]	Vertical RMS [m]
Guissona	0.120	0.220	0.13

5.1.6 Conclusions

Since ODOT will use the DMC and GPS/IMU integrated mapping system to generate 0.5feet geometric resolution orthophotos of high way corridors, the flying height should be 1524m AGL with the image scale of about 1:12700, based on the camera parameters. As this flying height is the maximum, for lower heights, smaller GSD can be achieved which can also be used to generate 6” GSD orthophoto. Note that for the DMC camera, the theoretic horizontal accuracy is about 0.3 GSD, i.e. 5cm, and the vertical is about 15cm.

According to the test results for DG using ADS40 with a similar GSD of 15.6cm published by IFP, Stuttgart University, the horizontal accuracy of 8–6 cm and the vertical accuracy of 10 cm was achieved with a very well calibration system. This result almost reaches the theoretical accuracy.

When the calibration is less than optimal, the DG accuracy in the object space will be significantly deteriorated to the level of several decimeters expressed as RMS, which could be 2–3, or even more, times worse than the AT results.

According to the reports from both academic institutions and industrial tests, DG is possible to be used to generate the 6" orthophoto for ODOT. However, a very careful system calibration must be done firstly and subsequently maintained. A higher forward overlap of 80% and side overlap of 60% have to be taken to increase the number of multi-rays; namely, to strengthen the geometric stability of the corridor area. The maximal flying height of about 1500 m is acceptable.

Before the mission, if possible, a field calibration should be done over a test field with well distributed and surveyed GCPs (measured by GPS) near the mission area. The flying height must be the same as the mission flying height. The GPS/IMU data must be processed without any discrepancy to achieve accurate position and attitude from GPS/IMU system. For this purpose, either comparing the GPS/IMU results with the AT results of the calibration field (two-step-calibration) or introducing the GPS/IMU observations into an extended bundle adjustment (ISO one-step calibration) could be considered.

In general, there should be a few independent check points scattered in the mission area to check the DG performance. If the object point positioning accuracy results indicate systematic errors, self-calibration should be considered to reduce the error. In addition, ISO with minimal number of GCPs in the mission field can be considered to compensate for the remaining errors.

It is concluded that theoretical object positioning accuracy could be achieved from DG with optimal overall system calibration. In case, the different systematic errors exist and GPS/IMU data are not well processed, ISO with self-calibration can be used to improve the results.

5.2 Experimental Performance Evaluation

In order to evaluate the DMC, calibration test flights were flown in Marion, Ohio, using the newly installed DMC camera in the ODOT airplane. Two calibration missions were executed to support the performance evaluation; data sets were collected on January 31, 2011 and April 13, 2011, respectively. The imagery acquired from the DMC was georeferenced in the Ohio State Plane North projection for the data set collected in January while the April data set was not georeferenced to any projection. In addition, ODOT provided GCP's, including coordinates and descriptions. All the processing at OSU was done using the Leica Photogrammetry Suite (LPS) 9.1 and Matlab. Image measurements were done in LPS, while computations were mostly done in Matlab.

5.2.1 Assessing of Test Data

The January dataset collected has high snow coverage causing most of the control points to not be visible or easily distinguished from other features on the ground. The snow caused the imagery to have high contrast and, thus, makes it very hard to see even the visible GCP's. Due to

the mentioned difficulties, the performance and interior orientation parameters could not be evaluated, as the minimum data processing requirements were not met with the January data set.

The April dataset validation, however, was adequate for performance evaluation. In this dataset, the number of visible GCP's provided was sufficient to perform a bundle block adjustment. A bundle block adjustment is based on a mathematical technique of triangulation that simultaneously determines the position and orientation of each image as they existed at the time of image capture as well as the ground coordinates measured in overlap areas of multiple images, by minimizing the errors associated with the imagery, image measurements, and GCP's. In short, a bundle block adjustment is in essence a simultaneous triangulation performed on all observations. Three test blocks were tested for this dataset.

During the processing and validation of the dataset collected on April 13, 2011, it was discovered that there was a numbering discrepancy between the image numbers and the exterior orientation numbering provided by ODOT. The image numbers in the coordinate list were not consistent with the filename numbering system for the imagery; there was a difference of 3 between the file naming of the imagery and the exterior orientation numbering convention. Also, during the processing of data, three control points proved to cause higher discrepancy in the measurements, SV409, SV410 and SV509A. Once these discrepancies were identified, the processing was repeated for all the validation tasks.

5.2.2 Block selection

There were three test blocks selected to perform the performance evaluation of the DMC. All three test blocks provide an independent evaluation. Also, the test blocks cover different locations of the test site, meaning that the evaluations of the test blocks will be uncorrelated

Test Block 1 includes six images from two different flight paths, with different flying height. This block covers the Northwestern part of the test site. The reason for this particular block evaluation was due to the area providing the highest number of visible GCP's. The evaluation of the flight paths having different flying heights was also of high importance in order to compare the effect of varying flying heights of the two different flight paths. The first flight path was in the north-south direction while the second flight path was in the east-west direction. The flying heights were approximately 900 meters for the first flight path, and 1,800 meters for the second flight path. For the performance evaluation of the DMC, 10 GCP's and 65 tie points were used in this block.

The area coverage with image center and boundaries is shown in Fig. 12, and the image overlap and control point distributions for the two flight paths are shown in Figs. 13 and 14.

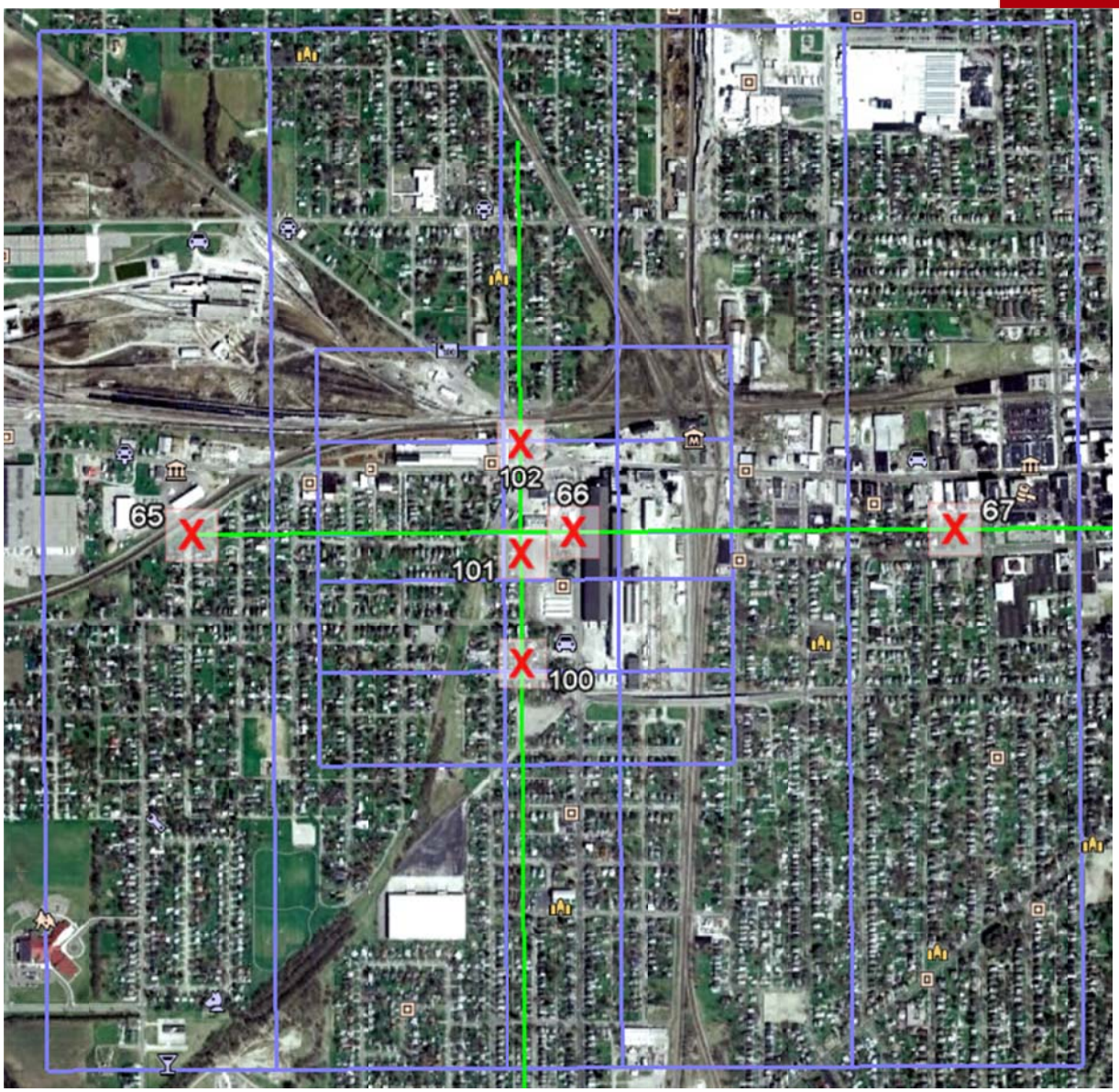

Figure 12 Image projection centers and boundaries with images for Test Block 1.

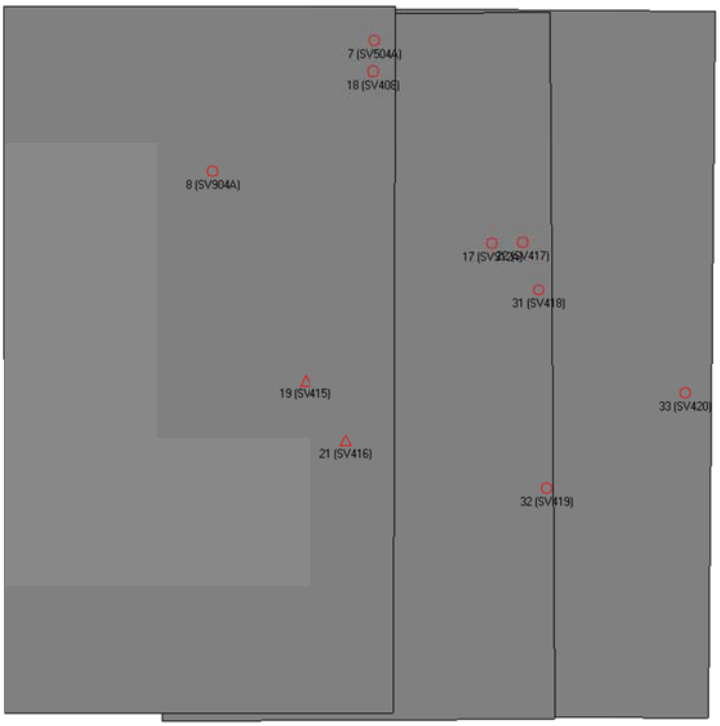

Figure 13 GCP distribution of images 66, 67, and 68.

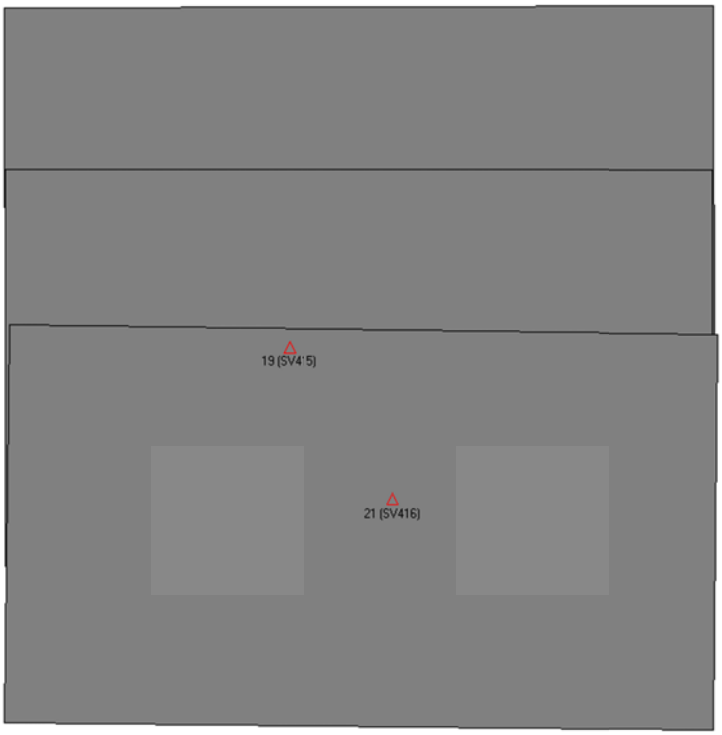

Figure 14 GCP distribution of images 24, 25 and 26

Test Block 2 contains 12 images from four different flight paths. From each flight path three images were selected in the Southern part of the test site. The flying height is 900 m for this block the images were acquired in the north-south and south-north direction. The reason for selecting this block was the consistent flying height. For the performance evaluation of the DMC, 5 GCP's and 143 tie points were used. The area coverage with image center and boundaries is shown in Fig. 15, and the image overlap and control point distribution is shown in Fig. 16.

Figure 15 Image projection centers and boundaries with images for Test Block 2.

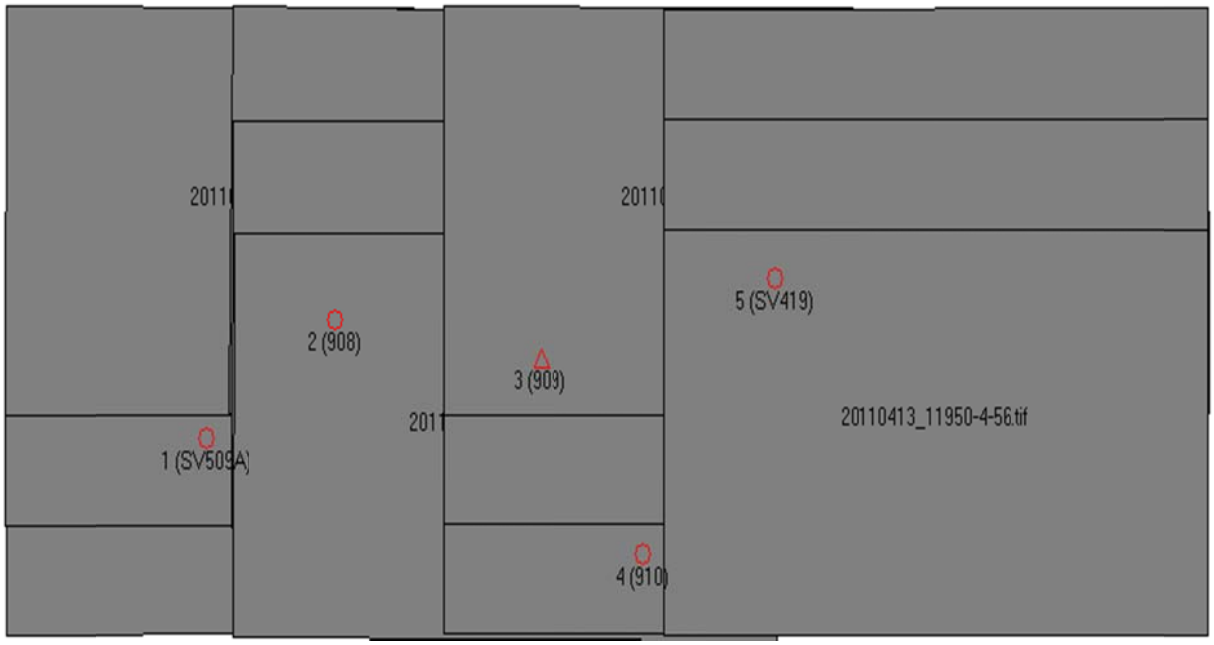

Figure 16 GCP distribution for Test Block 2.

Test Block 3 contains 12 images from two different flight paths; similar arrangement to Test Block 3 with the exception that the flying height is 1,800 m. For the performance evaluation of the DMC, 9 GCP's and 141 tie points were used. The area coverage with image center and boundaries is shown in Fig. 17, and the image overlap and control point distribution is shown in Fig. 18.

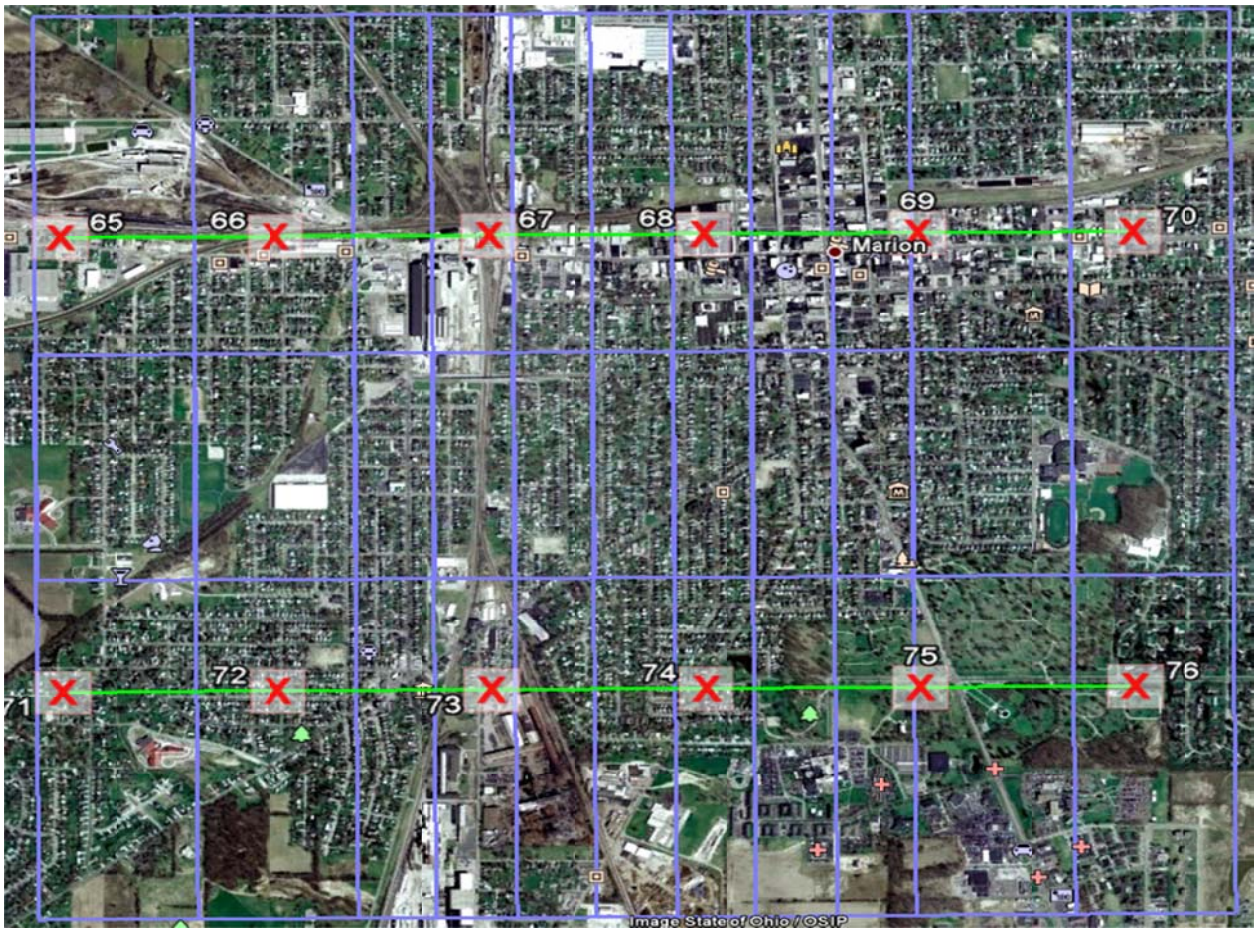

Figure 17 Image projection centers and boundaries with images for Test Block 3.

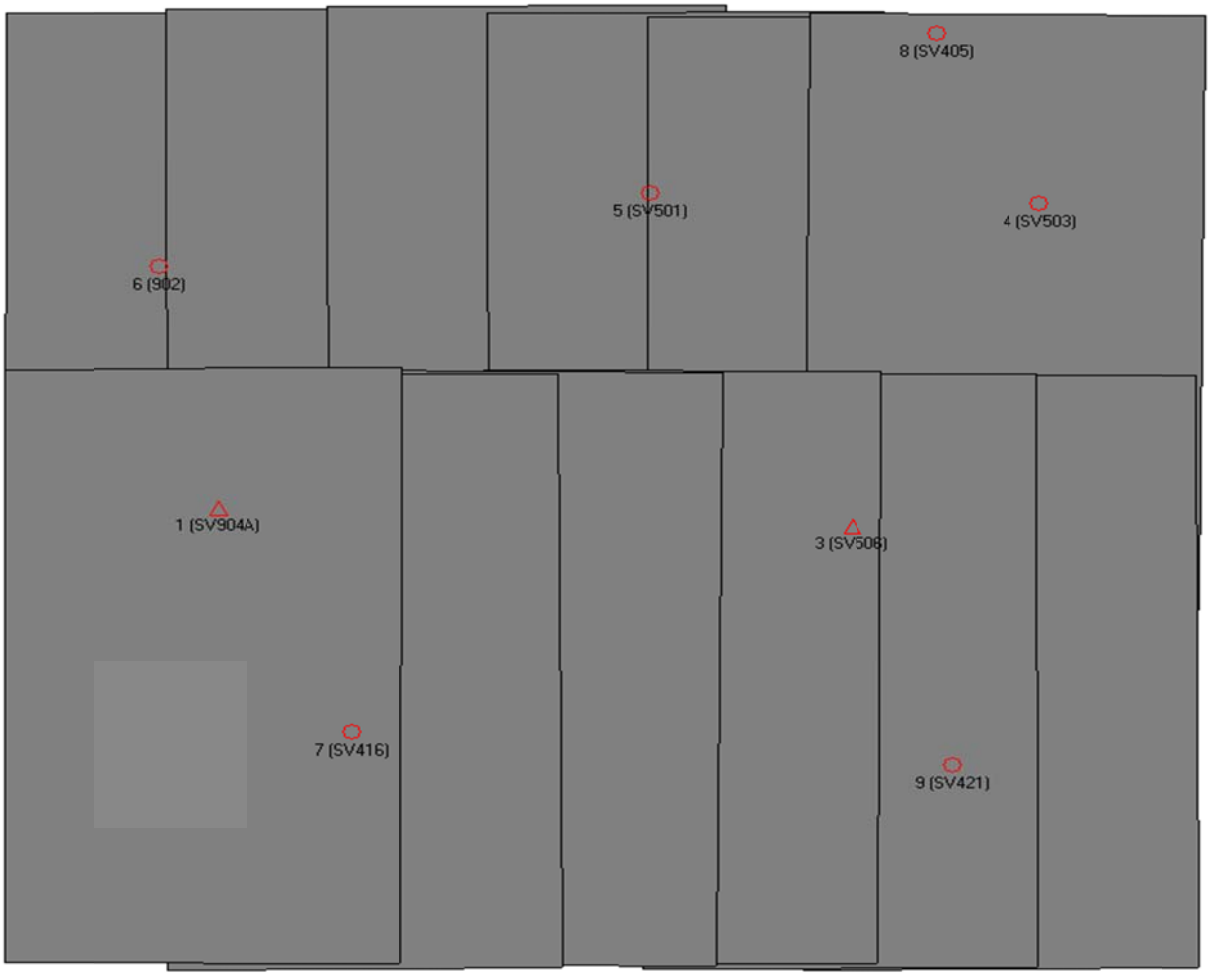

Figure 18 GCP distribution for Test Block 3.

5.2.3 Data Processing

The following procedures describe the data processing with the LPS software by step by step. First, the images were checked for ground control points; this was based how well they could be identified on the imagery. In order to orient an image, at least 3 ground control points (GCP) (x_i,y_i; X_i,Y_i,Z_i) are required due to the fact that each point has 2 equations and 6 unknowns parameters (X_0,Y_0, Z_0; ω, φ, κ) in the system provided the interior orientation parameters (IOP) are known; where lens projection center is at (X_0,Y_0, Z_0), and the rotation angles, ω, φ, κ around X, Y and Z axes, respectively. The collinearity equation is a physical model that represents the geometry between a sensor's projection center (X_i,Y_i,Z_i), the image coordinates (x_i,y_i) in the image space (image *i*), and the ground coordinates (X_g,Y_g,Z_g) in the object space [3]. In short, the collinearity equation describes a line on which the projection center of the sensor (O), the image point (p) and the matching object point (P) lie; see Fig. 19.

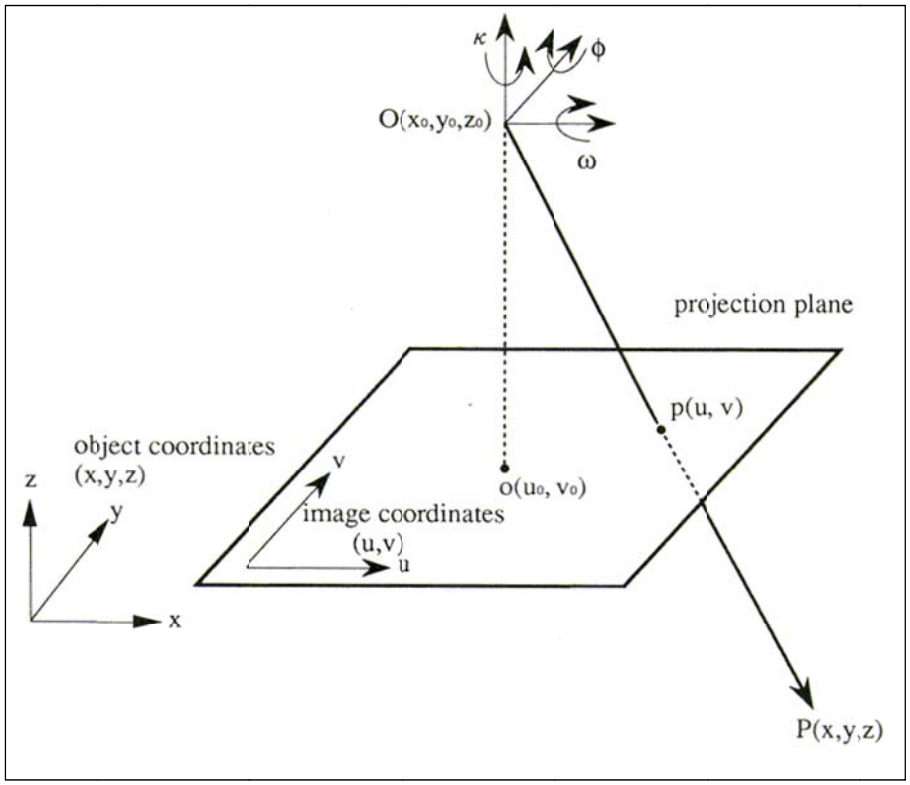

Figure 19 Geometry of central projection.

The image orientation can be performed by bundle block adjustment in which multiple images are used with fewer GCP's, and neighboring images are joined (relative orientation) by tie points in the overlapping image area. Note that there are other ways for orienting an image, such as single-photo resection and absolute orientation of a stereo model, but these methods are less effective for calibration compared to the bundle block adjustment. In particular, this is the case when there is a low number of GCP available, and therefore, the bundle block adjustment was used in the evaluation process.

All the three test blocks were processed the following way:

- Areas which contained the highest density of ground control points were selected in the block formation step
- Manual measurement of the GCP's image coordinates
- Manual tie point measurements (image coordinates)
- Automatic tie point measurement method was used to add more tie points
- Automatic tie point measurements were verified by operators
- Bundle block adjustment was performed

Depending on data availability, point distribution, etc., there are several options to control the bundle block adjustment process. In this investigation, five methods were considered, four including the bundle block adjustment with different configurations and one using direct geo-referencing, see Table 10. All the bundle block adjustment computations represent the indirect geo-referencing approach. The four bundle block adjustment methods differ whether camera calibration (IOP) is allowed or not and whether the sensor projection sensor data (EOP) is available or not.

Table 10 Methods used to process the test block.

Methods Used for Performance evaluation of the DMC Camera						
Method	**Direct Geo-Referencing**		**Indirect Geo-Referencing**		**Benefits**	**Calibration Aspect**
	IOP Status	**EOP Status**	**IOP Status**	**EOP Status**		
1	X	X	Fixed	Initial	Higher Redundancy	Compare Methods 1 and 2
2	X	X	Initial	Initial	Self-Calibration (weak)	
3	X	X	Fixed	Fixed	Accuracy Verification	Compare Method 3 and 4
4	X	X	Initial	Fixed	Self-Calibration (strong)	
5	Fixed	Fixed	X	X	Simple Computation	None

The first method was performed with the given camera interior orientation parameters (fixed), meaning the DMC camera IOP's will be held in the process, i.e., not allowing for calibration. The second method was performed without using the available interior orientation parameters, thus allowing for the interior orientation parameters to be adjusted. The camera calibration parameters obtained by the second method can be used for validating the fixed (given) DMC camera calibration. In addition, the EOP determined by the first two methods were then compared to those orientation parameters provided by the DMC using the direct geo-referencing data.

The third method uses the EOP's provided by direct geo-referencing as well as the given IOP's. The GCP's were then used as check points to verify the residuals of with respect to the computed values. The fourth method is similar to the third one, except allowing for the IOP's to be calibrated in the bundle block adjustment. The third and the fourth methods' residual results are then compared to each other to see the effect of self-calibration. The fifth method apples the DG process and the accuracy can be checked at the GCP's.

The theoretical accuracy was discussed in the Section (5.1), here only the main results are listed. For 900 and 1800 m flying heights, the horizontal and vertical accuracies are estimated to be 4.5 and 9 cm, and 14.6 and 29.3 cm, respectively.

5.2.4 Analyzing the Results

The analysis of the data was performed using the three different test blocks each covering a different area of the test site. Note each test block had different configurations. Only the summary is presented here, as Appendix (11.1) will describe the test results per each test block and also per method, including the horizontal and vertical error characterization.

The combined results of the five computations for Test Block 1 are shown in Table 11 and Fig. 20. As expected, Method 1 gives the best results; also confirming good IOP data.

Table 11 Test Block 1 numerical results.

Test Block 1 Residual Linear Distance Comparison					
	Method 1	**Method 2**	**Method 3**	**Method 4**	**Method 5**
GCP ID	**rD [m]**	**rD [m]**	**rD [m]**	**rD [m]**	**rD [m]**
7	0.31	0.32	1.03	0.47	0.96
8	0.12	0.12	0.69	0.41	0.67
17	0.21	0.18	0.51	0.50	0.45
18	0.15	0.18	0.90	0.50	0.94
19	0.02	0.01	0.31	0.21	0.29
21	0.02	0.02	0.47	0.14	0.45
22	0.21	0.25	0.77	0.40	0.72
31	0.12	0.15	0.71	0.41	0.65
32	0.33	0.35	0.78	0.19	0.72
Max	**0.33**	**0.35**	**1.03**	**0.50**	**0.96**
Min	**0.02**	**0.01**	**0.31**	**0.14**	**0.29**
Mean	**0.17**	**0.18**	**0.69**	**0.36**	**0.65**
STD	**0.11**	**0.12**	**0.22**	**0.14**	**0.22**

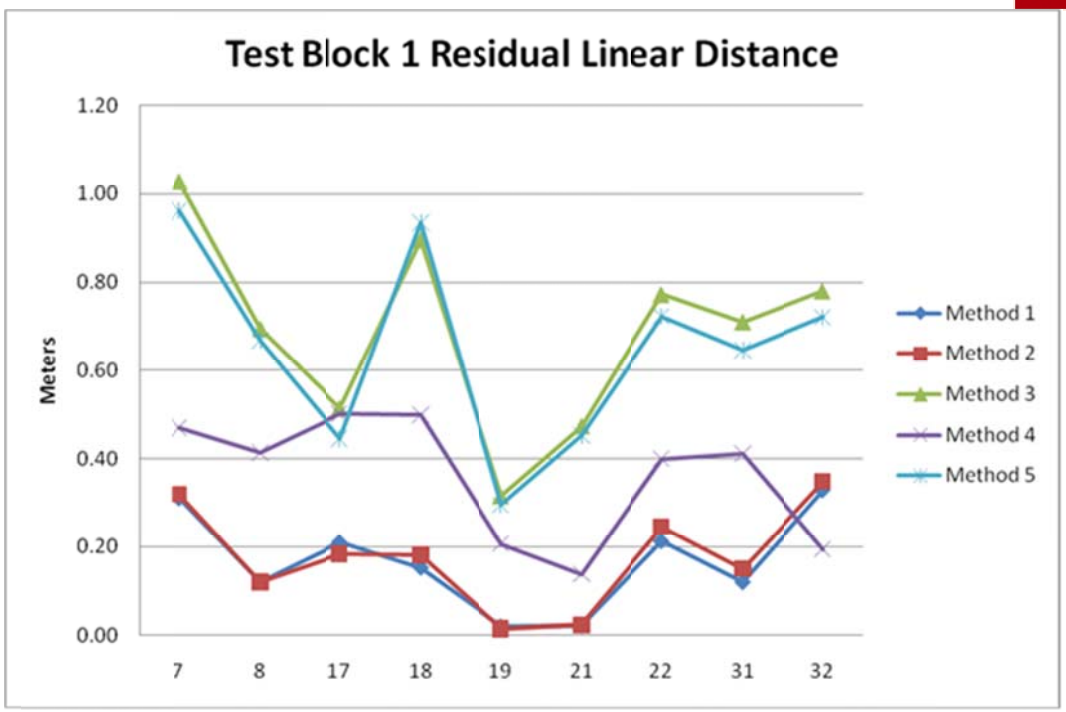

Figure 20 Visualization of Test Block 1 results.

The combined results of the five computations for Test Block 2 are shown in Table 12 and Fig. 21. In this case, Methods 2, 3 and 4 are showing practically identical performance. Note that DG produces the worse results (by orders), indicating some problem with IOP and/or EOP data. Additional investigation revealed GCP error.

Table 12 Test Block 2 numerical results.

Test Block 2 Residual Linear Distance Comparison					
	Method 1	**Method 2**	**Method 3**	**Method 4**	**Method 5**
GCP ID	**rD [m]**	**rD [m]**	**rD [m]**	**rD [m]**	**rD [m]**
1	0.53	0.13	0.44	0.45	12.84
2	0.29	0.09	0.37	0.31	5.18
3	0.06	0.17	0.31	0.30	0.40
4	0.09	0.08	0.35	0.34	0.52
5	0.50	0.13	0.34	0.33	0.39
Max	**0.53**	**0.17**	**0.44**	**0.45**	**12.84**
Min	**0.06**	**0.08**	**0.31**	**0.30**	**0.39**
Mean	**0.29**	**0.12**	**0.36**	**0.35**	**3.86**
SD	**0.22**	**0.04**	**0.05**	**0.06**	**5.42**

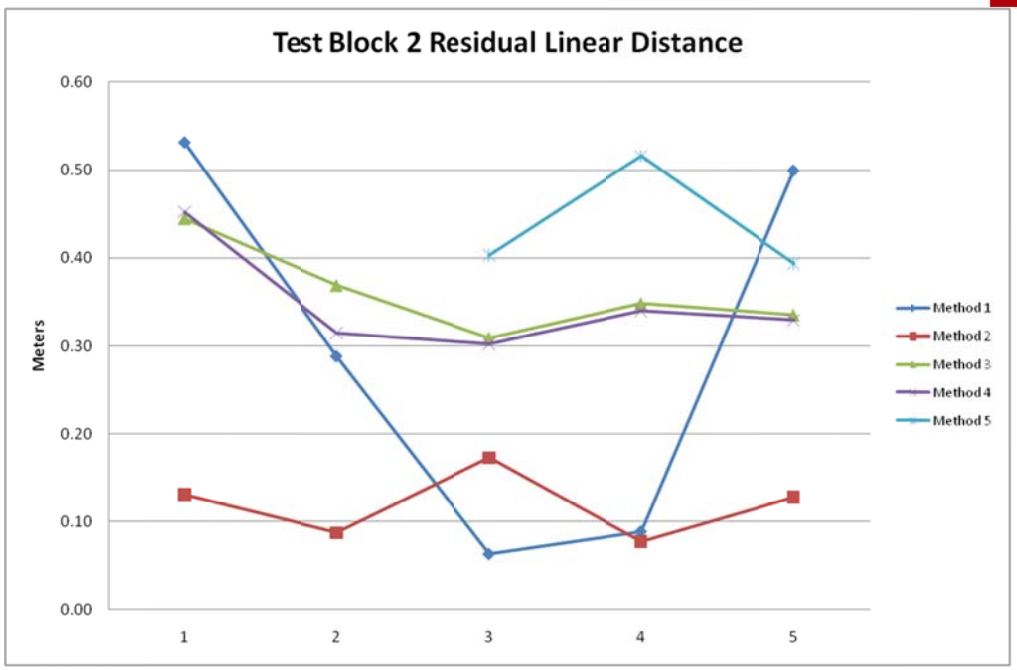

Figure 21 Visualization of Test Block 2 results.

The combined results of the five computations for Test Block 3 are shown in Table 13 and Fig. 22. In this case, Methods 1 and 2 are showing practically identical performance, again confirming good IOP data (camera calibration).

Table 13 Test Block 3 numerical results.

Test Block 3 Residual Linear Distance Comparison					
	Method 1	**Method 2**	**Method 3**	**Method 4**	**Method 5**
GCP ID	**rD [m]**	**rD [m]**	**rD [m]**	**rD [m]**	**rD [m]**
1	0.26	0.25	0.19	0.18	0.22
3	0.06	0.06	0.14	0.20	1.03
4	0.13	0.12	0.84	0.64	0.90
5	0.02	0.02	0.50	0.25	2.26
6	0.00	0.00			
7	0.07	0.08	0.77	0.52	0.72
8	0.40	0.41	0.49	0.35	0.70
9	0.17	0.17	0.70	0.56	0.63
Max	**0.40**	**0.41**	**0.84**	**0.64**	**2.26**
Min	**0.00**	**0.00**	**0.14**	**0.18**	**0.22**
Mean	**0.14**	**0.14**	**0.52**	**0.39**	**0.92**
SD	**0.14**	**0.14**	**0.27**	**0.19**	**0.64**

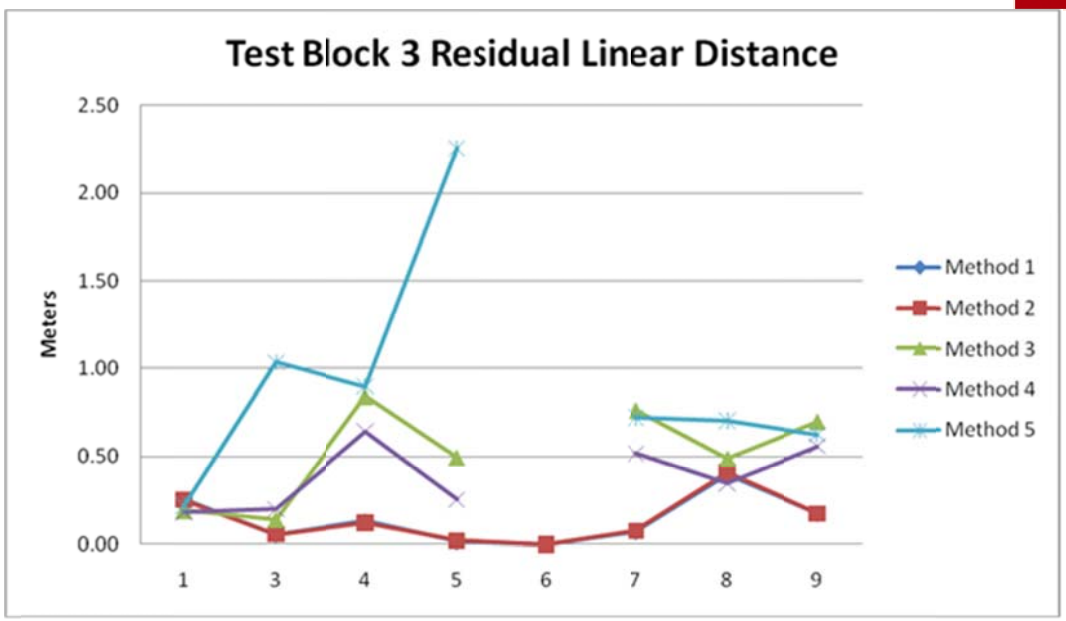

Figure 22 Visualization of Test Block 3 results.

The camera calibration results per test blocks are listed in Table 14. In general, the adjusted and manufacturer provided camera calibration parameters show a small difference; practically, in the few micron range. This is a confirmation that both data sets are acceptable. The magnitude of the changes between the fixed IOP (manufacturer's camera parameters) and self-calibration corrections are small yet in the view of the allowable corrections they match the error range of parameters. Note the principal point offset values are not coherent, as the x-direction is much worse than the y-direction. This shows consistency with our results from the different methods applied to the 3 test blocks. The focal length variation translates to error in the z coordinate. Note that a 0.001 mm change introduces 0.3-0.5 mm/x parallax. The principal point error of 0.01 mm simply translates to 7.5-15 cm shift in horizontal component for flying height of 900 and 1800 m respectively.

Table 14 Camera calibration results.

Difference between Manufacturer's IOP's and Self-Calibration			
Test Block	**Δc [mm]**	**Δx [mm]**	**Δy [mm]**
1	-0.0120	0.0115	0.0038
2	-0.0044	-0.0197	0.0036
3	-0.0055	0.0103	0.0031

In summary, the manufacturer's values of the IOP's are good and meet the specified performance level of the DMC system. The changes introduced by self-calibration are small; having only a small effect. The three test blocks yield different yet reasonable results. Therefore, the camera parameters are acceptable.

5.2.5 Conclusion

Five different approaches were used to evaluate and, ultimately, validate the performance of the DMC system. Using the April 13, 2011, calibration data set, the processing and analysis of the results confirmed a consistent performance, measured by ground control points; note that they were also used as check points in certain configurations. The blocks used for testing represented different geometrical conditions, resulting in changes in the relative performance of the five methods, which was expected. The fact that three test blocks were used reinforces the results, as they are independent.

Finally, suggestions to maintain the high performance of the camera in regular operations:

- There is always need for QA/QC, and therefore, the use of ground control point measurements is essential, as it provides the only independent way to characterize the achieved accuracy. Note that the check points should ideally have an even spatial distribution and, obviously, the more the better.
- For larger surveys, the area should be divided into smaller segments, and then follow the instructions provided in the previous point.
- If possible, more complex, or at least different, flight trajectories, such as a cloverleaf flight path, should be flown, as it helps to decorrelate the adjusted parameters.
- Finally, given the relatively easy availability of automated aerial triangulation, it is a good practice to run an AAT on any data set, as a check process. Either the results are confirmed, or slightly improved, or in rare cases, major problems are detected.

6. TRUE ORTHOPHOTO GENERATION

6.1 Objectives and Accomplishments

Nowadays, increasing number of orthophotos of highway corridor areas are needed for the purpose of maintaining and advancing the transportation system. While orthoimage production is a well-established process, bridge areas still present challenges, as without operator assistance, distortion is usually introduced. In addition, ghost effect around the bridge boundaries in the orthophoto product could be also unacceptable. The preference is given to high quality, so called true orthophoto products, which are free from the above mentioned degradations. In order to create good quality true orthophoto, a PDSM (Precise Digital Surface Model) and occlusion detection are needed. Therefore, the primary objective of this project is to develop a reliable method to create the PDBM (Precise Digital Bridge Model)/PDSM to generate the true orthophoto using the PDSM.

First, the focus is on developing the PDBM, which provides smooth bridge surface and boundaries. Generally, the bridge object boundaries in the LiDAR data due to the irregular and sparse nature of LiDAR points at breaklines cannot well determined. In contrast, bridge boundaries can be well extracted from the aerial images. Fusing clean and smooth boundaries from the aerial image and LiDAR data is an efficient approach to create the PDBM. Considering the efficiency and reliability, three approaches are provided to produce the PDBM, as follows:

- PDBM from LiDAR data
- PDBM from fusing LiDAR data and aerial image via the collinearity equation
- PDBM from fusing LiDAR data and optical image via a generic registration method

Regardless which approach is used, the first step is to create a CDBM (Coarse Digital Bridge Model) directly from the LiDAR data. Then, the CDBM is subsequently refined to form the PDBM. The basic idea is to enhance or re-create the smooth bridge boundaries in the CDBM. Above three approaches differ in method of creating the smooth bridge boundaries. The PDBM workflow, developed in this project, is reliable for both simple straight and complex curved bridges. PDBM is then merged to the DSM (Digital Surface Model) to form the PDSM for the true orthophoto generation.

When the PDSM is created, the focus is on the true orthophoto generation. The key issue is to detect the occluded cells, caused by the bridge boundaries in the PDSM. Those occluded pixels in the true orthophoto are filled with content from the slave (second) image or white pixels if the slave image unavailable. Angle-based and z-buffer methods are implemented and tested. According to our tests, the angle-based method has better performance than the z-buffer method. In addition, as the occluded cells are caused by the bridge boundary which is well determined in the PDSM, therefore, it is possible to simplify the occlusion detection. This method has been also implemented in software developed. As requested, the true orthophoto should be in the GeoTIFF format; namely, geo-referenced true orthophoto. The current version of the true orthophoto generation program, TrueOrthoPro does not directly support the export to GeoTIFF. The workflow to generate GeoTIFF files is described next. The true orthophoto is the same size as the PDSM used, and PDSM metadata which is the LAS format information file is available, this information can be used to create the GeoTIFF metadata, namely, *.gtf. ListgeoG GUI which is a free 3rd-party GeoTIFF tools in GUI form can support to integrate the GeoTIFF metadata to the true orthophoto.

The final product of this research project is the software developed in MATLAB and C++. Several open sourced libraries are used, such as PCL (Point Cloud Library) is used to create PDBM and OpenCV is used to generate the orthophoto/true orthophoto. ListgeoG GUI is used to convert the true orthophoto into GeoTIFF format. An overview of the software is presented in the Table 15.

Table 15 Software product list.

Software	Main Tasks	Development Environment and Libraries
MATLAB based processing	+ data workflow control + data pre-processing + co-registration + smooth bridge boundaries generation + precise DSM generation + occlusion detection	MATLAB2011b
PCDProcessing	+ coarse DBM + precise DBM	+ VS 2010 MFC GUI + PCL
TureOrthoPro	+ regular orthophoto generation + true orthophoto generation	+ VS 2010 MFC GUI + OpenCV
ListGeoG	+ convert true orthophoto to GeoTIFF format	+ GeoTIFF GUI

All routines/programs of the developed software are listed in the Table 15, following the order of the workflow. In subsequent sections, the entire project workflow is reviewed and some issues are emphasized and discussed.

Table 16 List of developed software

Module	Routines/Programs
Pre-processing	Step_0_AerialLevelImageGen.m
M-0 Initialization	Module_0_InitialProj.m (mandatory)
M-1 Data pre-processing Module_1_MainFun.m (mandatory)	Step_1_1_RawLASProcessing.m
	Step_1_2_LASImgGen.m
	Step_1_3_1_ROISelectionLASImg_I.m Step_1_3_1_ROISelectionLASImg_I.m
	Step_1_4_CheckROI.m
	Step_1_5_ElevationAnalysis.m
M-2 Coarse DBM Module_2_MainFun.m	PCDProcessing (mandatory)
	Step_2_1_SubROI2PCD.m
	Step_2_2_BridgeSurfaceIdentifier.m
	Step_2_3_BridgeSurfaceClassifier.m
	Step_2_4_UpperLowerBreakLinesIdentifer.m
	Step_2_5_SubPCDMerger.m
M-3 Co-registration Module_3_MainFun.m (optional)	Step_3_1_HuiFFTLogPolarApp_ODOT.m
	Step_3_2_Hui2ndImgBackTrans.m
	Step_3_3_HuiTranslationEstimation.m
	Step_3_4_HuiHarrisPDFMatching.m
M-4 Smooth Boundary Module_4_MainFun.m (mandatory)	Step_4_1_LinearSegROI_StraightBridge_I.m Step_4_1_LinearSegROI_StraightBridge_II.m Step_4_1_LinearSegROI_StraightBridge_III.m Step_4_1_LinearSegROI_StraightBridge_IV.m
	Step_4_2_SmoothBoundaryFitting_StraightBridge.m
	Step_4_3_PreSmoothBoundaryICPFittingInMappingSystem.m
	Step_4_4_SmoothBoundaryICPFittingInMappingSystem.m
M-5 Precise DBM Module_5_MainFun.m (mandatory)	PCDProcessing (mandatory)
	Step_5_1_PDBM.m
	Step_5_2_PDSM.m
	Step_5_3_PDSM2LPS.m
	Step_5_4_SmartDSM.m
M-6 True Orthophoto Module_6_MainFun.m (mandatory)	Step_6_0_AerialImageGen.m
	Step_6_1_AngleDistanceMatrix.m
	Step_6_2_OcclusionDetectionZBuffer.m Step_6_2_OccusionDetectionAngle.m
	Step_6_3_RefinementOcclusionMatrix.m
	TrueOrthoPro (mandatory)
	GeoTIFF Tool (mandatory)

6.2 Problem Identification

The core objective of this research component is to correct for bridge introduced DEM distortions and ghost effects in the orthophotos. Bridge problems in orthophoto producta are mainly caused by the following two reasons:

- Bridge object is not or not correctly modeled in the DSM (Digital Surface Model), and then the bridge is shown at the wrong place or bridge boundaries are distorted in the orthophoto.
- In case the correct DSM is used, the ghost effect may be caused by occlusion areas due to bridge boundaries.

Figure x shows those typical problems. Fig. 23a is an orthophoto using DSM without a precise bridge model; note that the bridge body is lower than at its two ends. Figure 23b shows the distortion and ghost effect. After the bridge model is refined, Fig. 23c shown only the remaining ghost effect.

(a)

(b)

(c)

Figure 23. Distortions and ghost effects

Figure 24a is the DSM generated from LiDAR data, and used to create orthophoto in the Fig. 1 23b. Figure 24b is the refined DSM, and used to create the orthophoto in the Figure 23c.

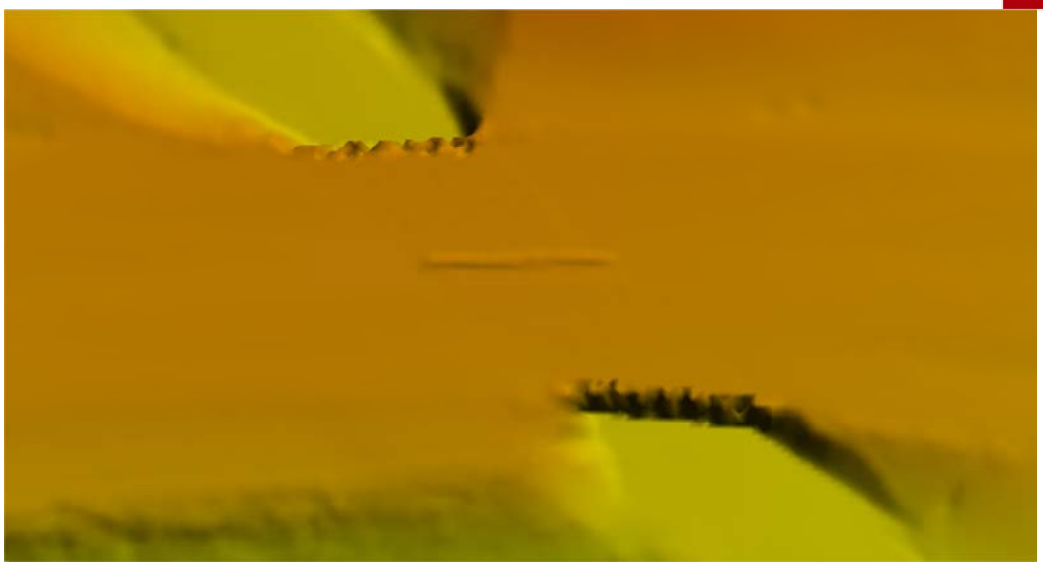

(a)

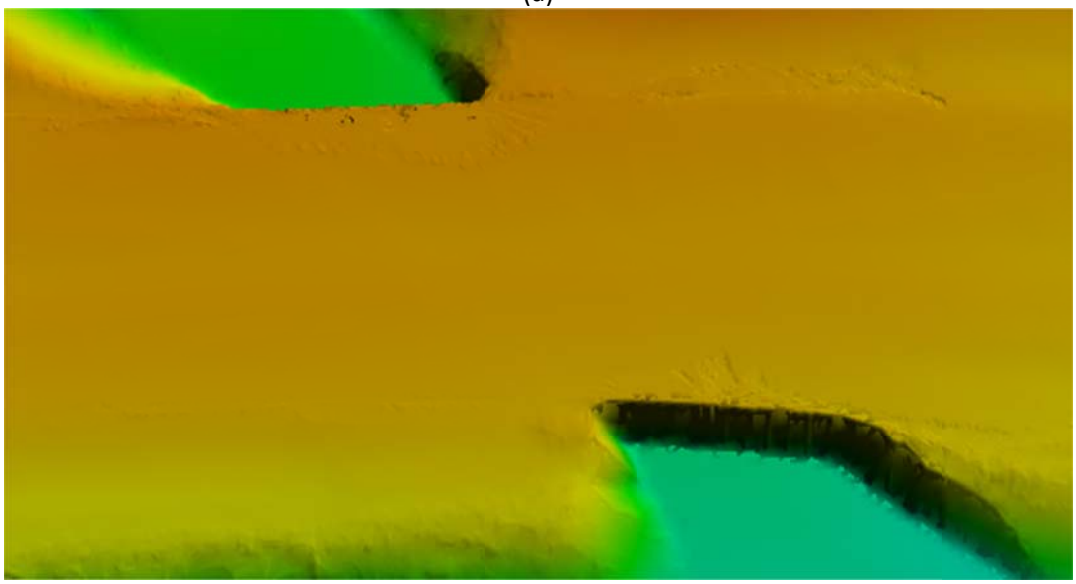

(b)

Figure 24 Regular DSM from LiDAR data (a), and refined DSM (b).

As seen in the above figures, the PDBM (Precise Digital Bridge Model) is required to place the bridge in the correct position in the orthophoto. In addition, the bridge boundaries have to be smooth and clear in the PDBM to avoid warped boundaries in the orthophoto. Even when a PDSM is used, ghost effects can occur in the rectified image due to occluded areas in the aerial image, and thus, occlusion detection and compensation are needed. Fig. 25a illustrates how the ghost effect is caused by occlusion due to the bridge boundary. In order to remove the ghost effect, the occlusion area should be detected in the DSM. There are two main groups of occlusion detection methods: distance-based [Amhar et al., 1998] and angle-based [Habib et al., 2007]. Once the occluded cells in a DSM are detected, the occluded area of a master image is then filled with the visible content in the slave (second) image. In other words, images with

different camera view angles are used to compensate the occluded areas to eliminate the ghost effect in the orthophoto. Fig. 25b shows the true orthophoto generation from two images.

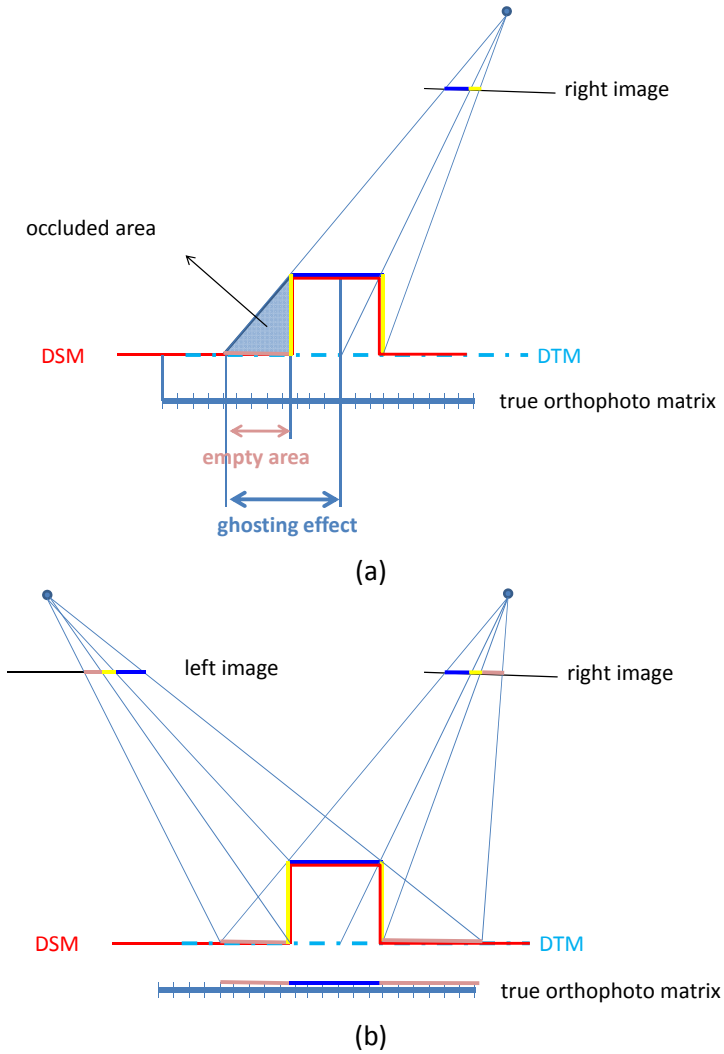

Figure 25 Ghost effect (a), true orthophoto generation based on two images (b) .

After identifying the problems, a comprehensive literature review was conducted to find possible solutions, and then development of our own approach started. In the following sections, the research work is presented.

6.3 Novel Registration Approach for LiDAR/Optical Imagery

PDBM generation plays a key role in the project. At the early research stage, a comprehensive literature review was conducted to understand the state-of-the-art of the PDBM generation. Generally, LiDAR data can directly provide accurate and dense surface measurements, yet, it cannot well determine the man-made object boundaries due to the irregular and sparse nature of LiDAR points, in particular at breaklines. On the other hand, the man-made object boundaries

can be well extracted from optical imagery, as imagery provides higher spatial resolution. Fusing clean and smooth boundaries from optical image and LiDAR elevation data offers an efficient way to create the digital man-made object model [Kim et al., 2008; Rottensteiner and Briese, 2002; Sampath and Shan, 2007; Vosselman, 1999]. Reviewing related publications, it was found that most of the research is focused on precise digital building modeling. The main idea is to extract 2D roof outlines of buildings from aerial images, and then project them to the 3D LiDAR data space via the collinearity equation, and subsequently, compare them with 3D linear features extracted from LiDAR data to form the smooth and precise digital building models. Those methods show good results for automated generation of polyhedral building models for complex structures [Kim and Habib, 2009; Wu et al., 2011]. However, implementation of these methods could be complex and computation load could be heavy. Earlier research is focused on either generating DBM (Digital Bridge Model) based on analysis of LiDAR point cloud profile [Sithole and Vosselman, 2006] or bridge boundary extraction from DTM (Digital Terrain Model) [Goepfert and Rottensteiner, 2010]. In summary, the determination of man-made object boundaries in LiDAR data is a rather complex task. If the registration between LiDAR intensity and high resolution imagery can be established, it is not necessary to generate the perfect DBM from LiDAR data domain, as the LiDAR data derived CDBM (Coarse Digital Bridge Model) can be refined by introducing smooth bridge boundaries, extracted from the high resolution image. This inspired the development of a novel registration approach for the LiDAR/optical image pair.

The proposed approach is a hybrid multiple-domain image registration method using a coarse-to-fine strategy. First, a modified LPFFT (Log Polar FFT) with an internal validation module is used to estimate the coarse similarity transformation between LiDAR intensity and optical images. Next, strong HCs (Harris Corners) in both images are generated and transformed to the other image domain via the estimated coarse transformation, and, subsequently, scale- and rotation-invariant PDF (Probability Density Function) mean-shift matching [Comaniciu et al., 2003] is used to find the correct correspondences. Finally, the RANSAC (RANdom Sample Consensus) [Fischler and Rolles, 1981] scheme is employed to detect and remove blunders among the matches, and eventually estimate the parameters of an affine or a perspective transformation. The entire workflow is illustrated in the Fig. 26.

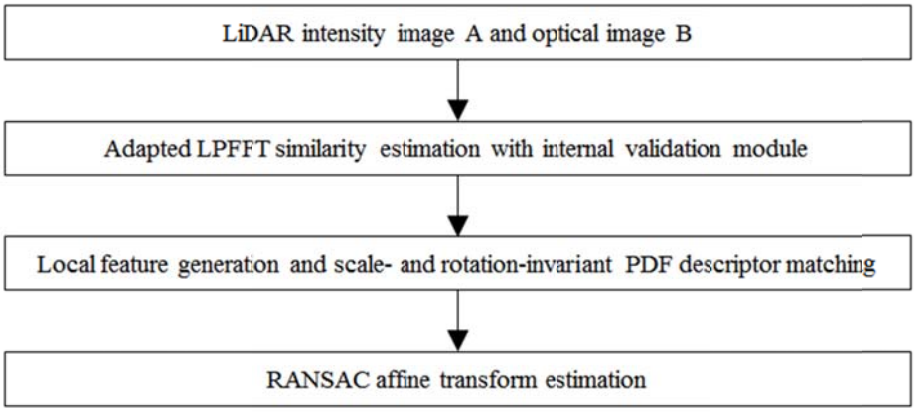

Figure 26 Proposed multiple domain image registration workflow.

The research was divided into three phases. In the phase 1, the focus was on reviewing current feature-based, intensity-based and frequency-based registration methods, and sorting out the possible solutions for registering LiDAR intensity and optical images. Next, the selected methods were tested including performance evauation [H. Ju et al., 2011; C K Toth et al., 2010]. In the phase 2, the proposed method was implemented in MATLAB, and tested with limited data sets; promising results were achieved [Hui Ju et al., 2012; C Toth et al., 2011]. In the phase 3, the develoepd method was integrated to the PDBM generation approach, which is introduced in the following sections. The performance and test results of this registration method are alos provided in the subsequent sections.

6.4 PDBM Generation

Considering efficiency and reliability, three approaches were implemented as main components of the final software:

- PDBM from LiDAR data
- PDBM from fusing LiDAR data and aerial image via the collinearity equation
- PDBM from fusing LiDAR data and optical image via a generic registration method

6.4.1 CDBM Generation

CDBM generation is the first step, and it is the same for all the three approaches. The research on CDBM generation can be divided into two phases.

In the phase 1, the main focus is on creating CDBM for simple bridges. Fig. 27 shows the workflow of the CDBM for the simple bridge. First, ground points and non-bridge points should be filtered out. Ground points can be easily separated based on elevation values. For non-bridge points having similar height as the bridge surface, the intensity value can be used for filtering. Unfortunately, pavement markings and/or vehicles on the bridge may have different reflectance characteristics, and thus, those points can be also removed from the bridge surface, see Figure 28a. In order to trim those sparse outlier point clusters in the intensity/elevation value filtered data, a statistical outlier removal filter based on statistical analysis of each point's neighborhood is applied to clean the bridge points. For each point, the mean distance to all its closest *n* points is computed. By assuming Gaussian distribution with a given mean and a standard deviation, those points whose mean distances are outside the interval defined by the global distances mean and standard deviation can be regarded as outliers and removed from bridge surface point set, see differences between Figs. 28a and 28b.

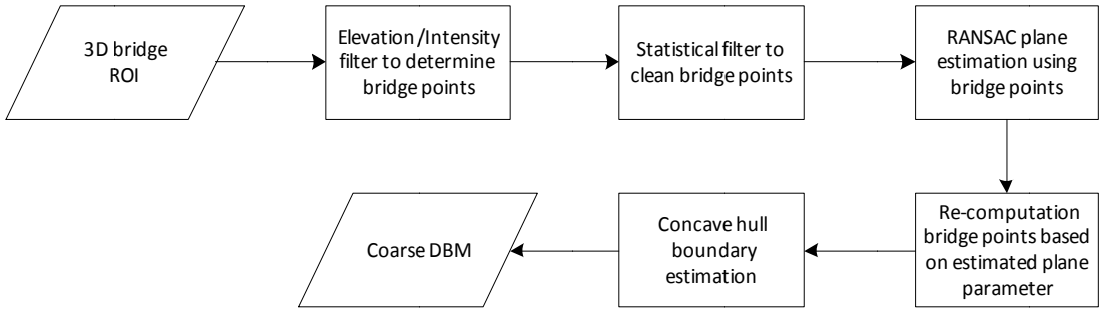

Figure 27 Coarse DBM generation workflow.

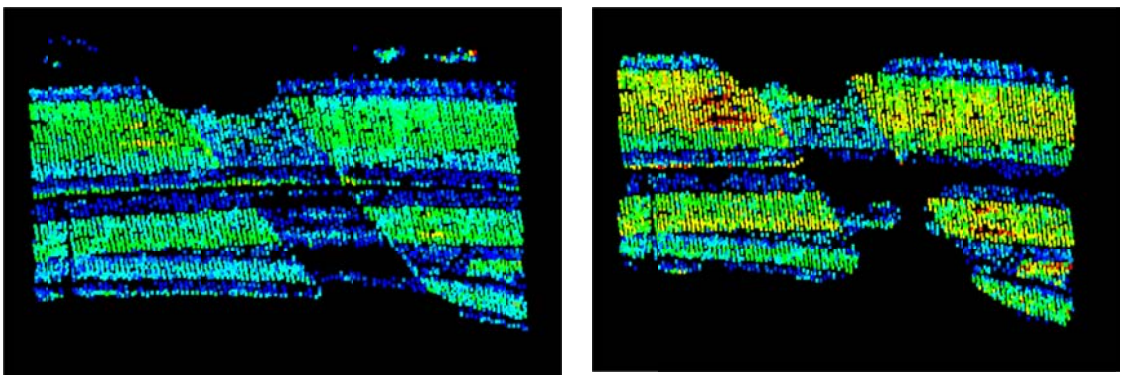

(a) (b)

Figure 28 Filtered bridge points using elevation and intensity threshold (a), and cleaned bridge points using a statistical filter (b).

3D RANSAC (RANdom Sample Consensus) [Fischler and Bolles, 1981] plane estimation is performed based on the clean bridge points. The 3D plane equation is given as:

$$aX + bY + cZ + d = 0$$

where *a, b, c, d* are the 3D plane parameters, *X, Y, Z* are the LiDAR point coordinates. RANSAC method is embedded to estimate the robust plane parameters. Next, the estimated plane parameters are used to re-compute the clean bridge points' elevation values. The newly computed points are all on the estimated plane which is regarded as the bridge surface. Subsequently, concave hull boundary estimation is applied on the refined surface points, as the bridge surface has a concave shape. Fig. 29 shows the LiDAR points on the concave hull boundary polygon, marked white. Bridge boundary points are also determined by checking their elevation values with respect to their neighborhood in a circular searching area. The elevation difference between a bridge boundary point and its neighboring ground points should be large, whereas, the elevation difference between a surface point and its neighbor points on the bridge surface should be small. Bridge boundary points are marked in sky blue in the Fig.29.

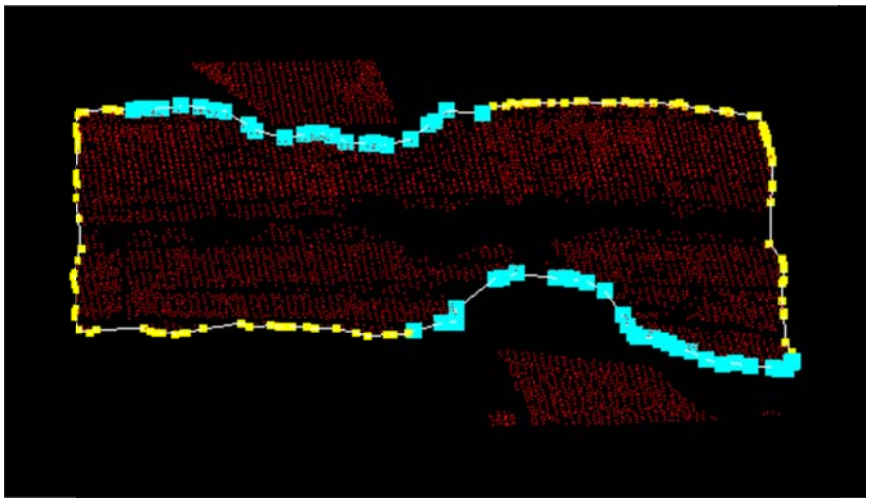

Figure 29 Concave hull boundary points (yellow) and bridge boundary points (sky blue).

In the phase 2, the focus was on the long curved bridges. The approach, applied to straight bridges experienced difficulties at processing long curved bridges because a 3D plane may not fit all points on the long curved bridge surface. Normally, a long curved bridge surface is a smooth curved surface; clearly, not a plane. Therefore, a classifier was developed to identify those non-bridge points which include the vehicles and rails on the bridge surface. The classifier has two components. The first component is to use the surface normals to classify bridge surface and non-bridge points. The second component is to divide the bridge into several rectangle cells, and then analyze the elevation values in the cells to identify those non-bridge points.

Next, the new CDBM generation approach is discussed. First, the bridge ROI is manually selected. The ground and bridge points are separated based on elevation analysis. For non-bridge points having similar height as the bridge surface, the intensity data is used for filtering.

For example, Fig. 30 is the 3D visualization of a simple bridge. The color bar at the bottom shows the elevation values in feet. An elevation histogram is useful to decide on the elevation threshold value to separate the ground points. Fig. 31 shows the elevation histogram. Obviously, the right peak indicates the elevation range for the bridge surface, and the left peak for the ground.

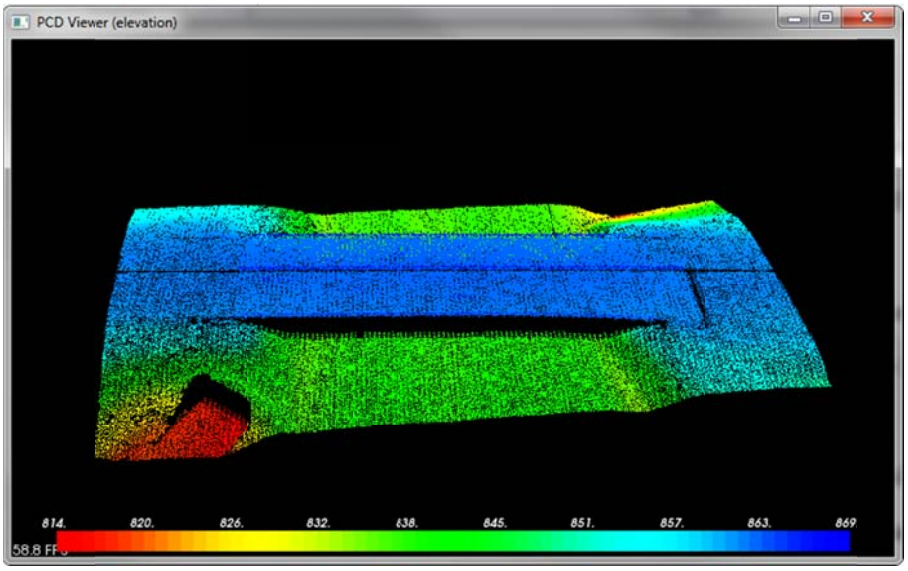

Figure 30 Bridge ROI point cloud visualization via elevation values.

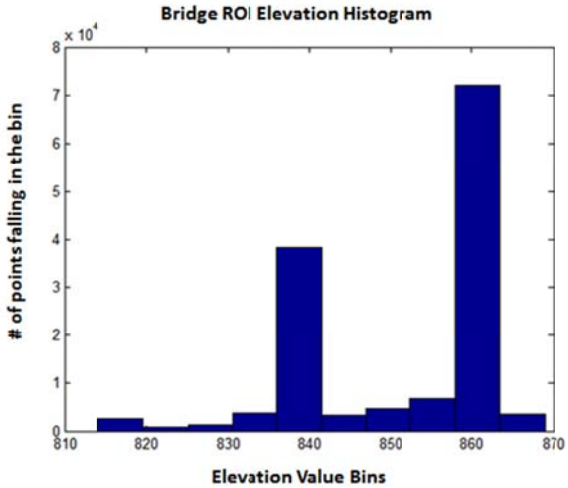

Figure 31 Bridge ROI elevation histogram.

Fig. 32 shows the bridge points after applying the elevation filter with a threshold value of 860 feet. Rails on the bridge boundaries and bridge axle wire are higher than other bridge points, and visualized in green color. If there are vehicles, they should be also higher than bridge surface. In the CDBM generation, those non-bridge points should be removed. In addition, the bridge boundary points should be also detected.

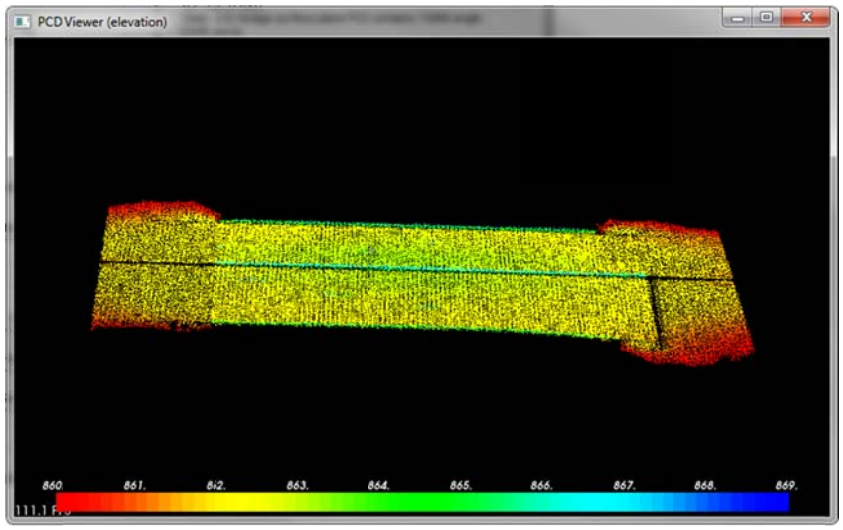

Figure 32 Bridge visualization after applying elevation filter.

In order to detect the bridge boundary, the normal direction of every bridge point is computed. To compute the normal vector, an effective local circular region is needed. According to test data characteristics, the local region radius was set to 1 m to compute the normal. The normal computation routine is provided by the PCL (Point Cloud Library). The algorithm is based on the first order 3D plane fitting.

Fig. 33 illustrates the normal vectors of the bridge points. Normals of points on the bridge surface have almost vertical direction, while normals of points on breaklines have arbitrary directions. The slope angle of every point is then computed using the normal vector. The slope angle is defined as the angle difference between the normal direction and the nadir direction. Fig. 34 is the slope angle histogram. Obviously, most slope angles are round 0 and 180 degrees, which are from the points on the bridge surface. Those points with slope angle from 10 to 170 degrees are classified as object points not on the bridge.

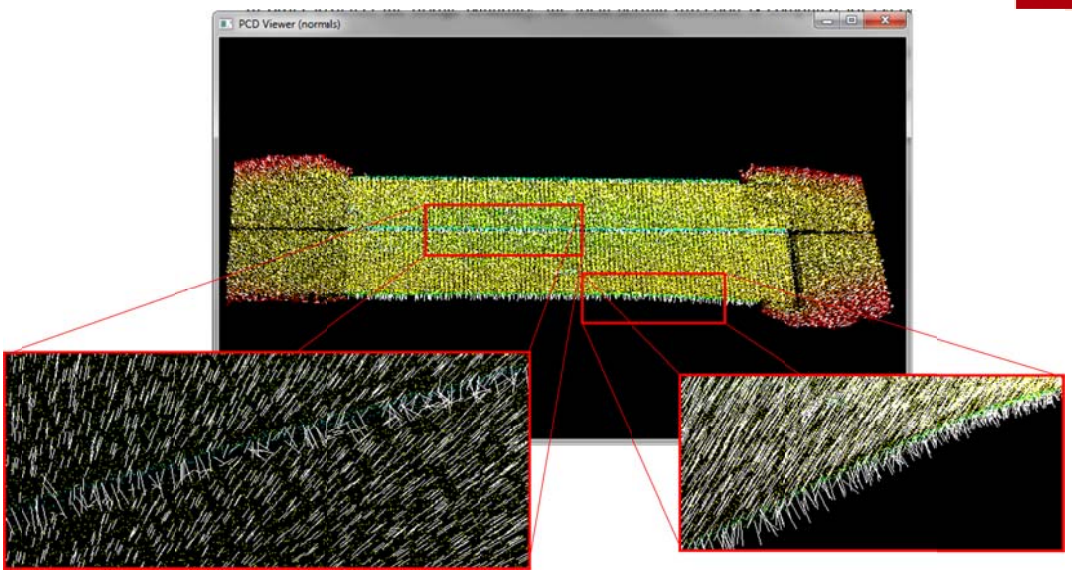

Figure 33 Normals of bridge points.

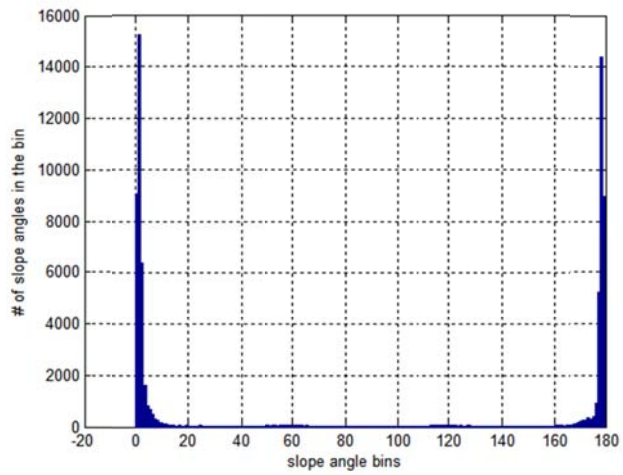

Figure 34 Slope angle histogram.

In addition, a local elevation analysis is performed to find out the remained object points on the bridge surface. For example, the bridge ROI data is divided into $n \times m$ square cells. The mean elevation and the standard deviation (σ) are computed from all points in the cell. Those points whose elevation values apart from the mean value larger than 3σ are regarded as object points on the bridge surface.

Fig. 35 shows the classified object points not on the bridge surface after slope angle analysis and local elevation analysis. Obviously, rails and vehicles on the bridge surface are separated from the bridge points. Figure 36 shows the points on the bridge surface, which is quite smooth and the points are on a plane.

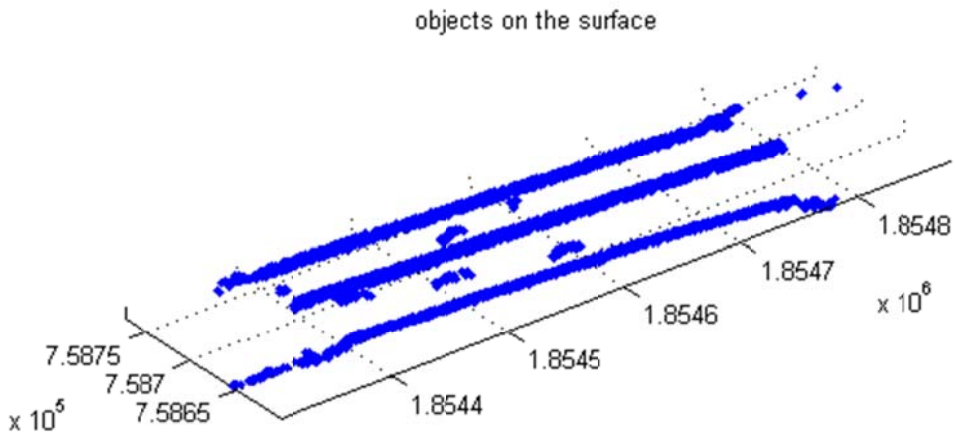

Figure 35 Non-bridge points.

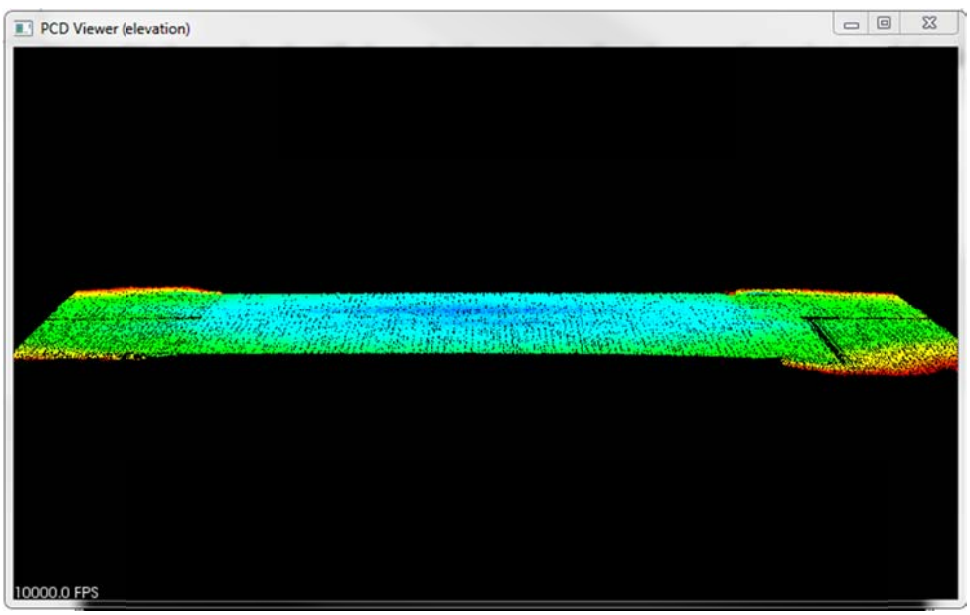

Figure 36 Bridge surface points.

Elevation values of those object points (rails and vehicles on the bridge surface) are recomputed based on their neighbor points elevation values. In our implementation, the elevation value is the average elevation value of its nearest 10 points. Then, all object points are pulled back to the bridge surface. Subsequently, concave hull boundary estimation is applied on the refined surface points, as the bridge surface has a concave shape generally. Bridge boundary points (those on breaklines) are also determined by checking their elevation values with respect to their neighborhood in a circular searching area. The elevation difference between a bridge boundary point and its neighboring ground points should be large, whereas, the elevation difference between any surface point and its neighboring points on the bridge surface should be small. Fig.

37 shows the refined bridge surface points in blue, the concave hull boundary points are in red, and the bridge boundary points are in yellow.

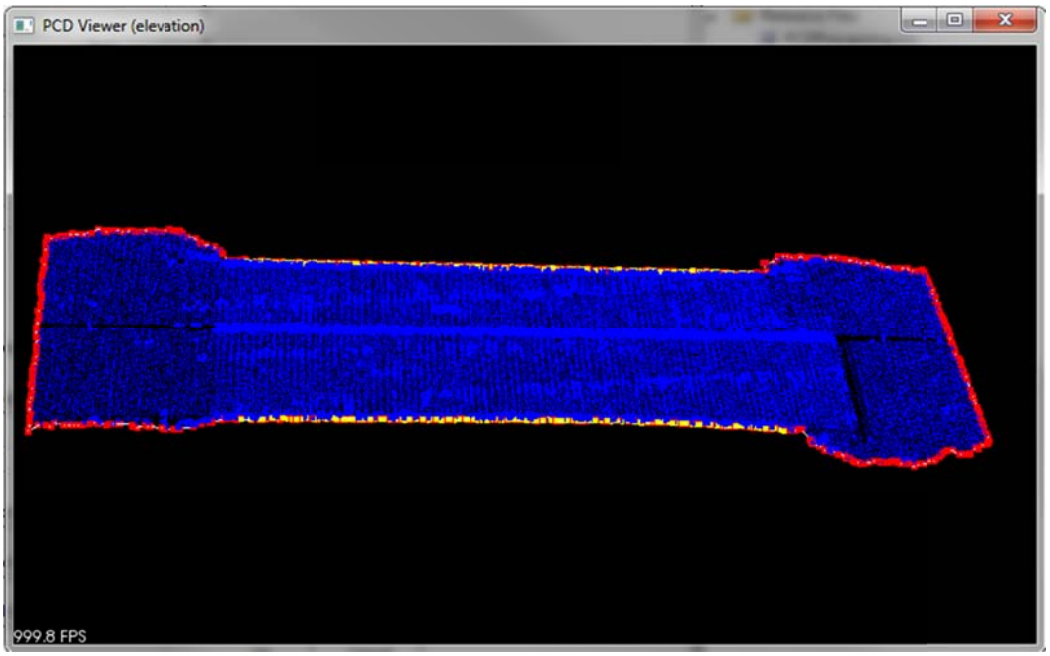

Figure 37 Concave hull boundary points (red) and bridge boundary (yellow).

Fig. 38 shows the final CDBM. All objects on the bridge surface are removed and the surface is smooth. In the new CDBM approach, the long curved bridge surface is not reconstructed via a 3D plane, which is not reliable, but via the classified bridge surface points.

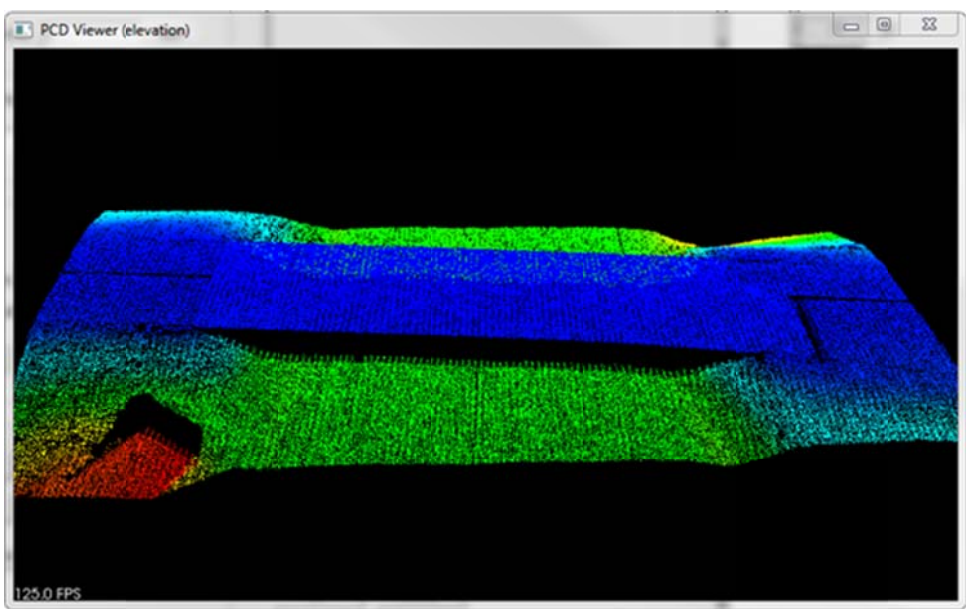

Figure 38 CDBM.

6.4.2 Smooth Bridge Boundaries

PDBM is obtained by adding the smooth bridge boundaries to the CDBM. The three approaches differ based on how the smooth bridge boundaries are created. In the first case, if the bridge boundary points are well determined in CDBM, the smooth bridge boundaries can be directly computed from those boundary points. The remaining task is to determine the upper and lower boundaries. This is performed automatically based on a horizontal scanning. For the vertical directional bridge, the boundary points are rotated to an appropriate position for the horizontal scanning. For example, the entire curved bridge is divided into two sub ROIs, see Fig. 39. After CDBM generation, it is observed that the CDBM boundaries are in good quality. Then, the upper and lower boundary points in the CDBM can be directly classified. The upper boundary points in the CDBM are shown in Fig. 40, and classified upper and lower boundary points are shown in Fig. 41.

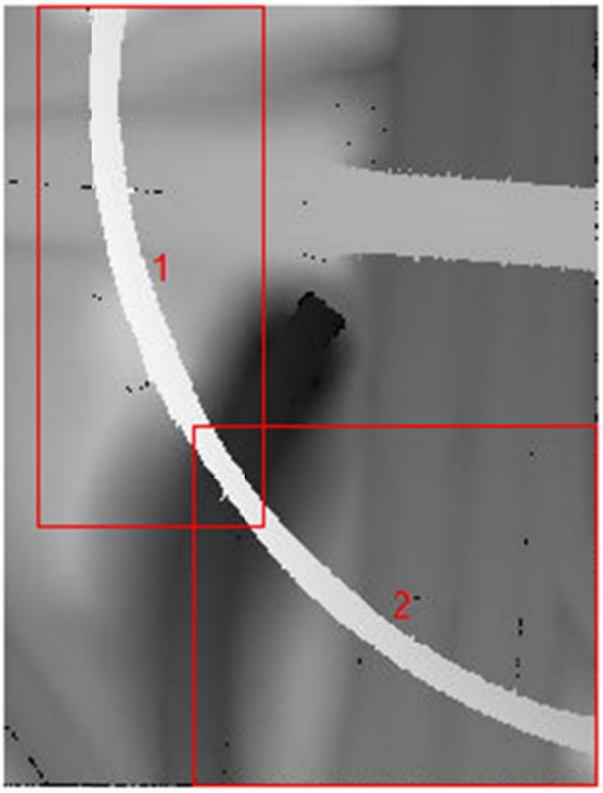

Figure 39 Two sub ROIs inside a bridge ROI.

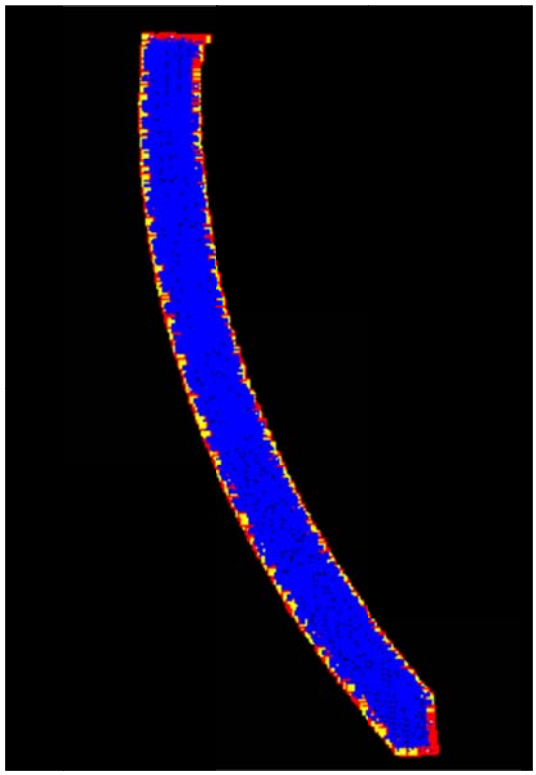

Figure 40 CDBM of sub ROI 1 bridge segment.

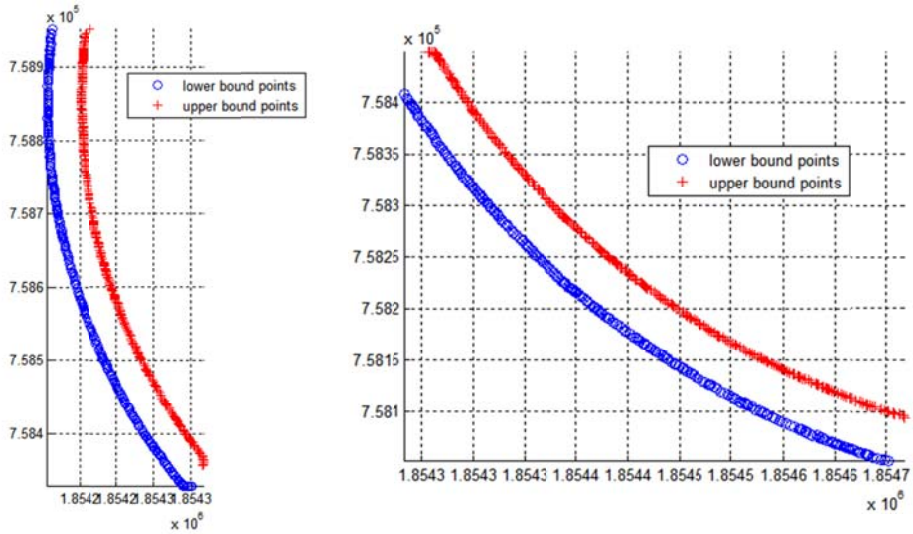

(a) (b)

Figure 41 Automatic classification of upper and lower boundary points in sub ROI 1 (a) and in sub ROI 2 (b).

Next, the bridge boundaries from sub ROIs are merged into a complete upper/lower bridge boundary. A polynomial function is used to produce very dense and smooth bridge boundary points. Figure 42 presents the final PDSM.

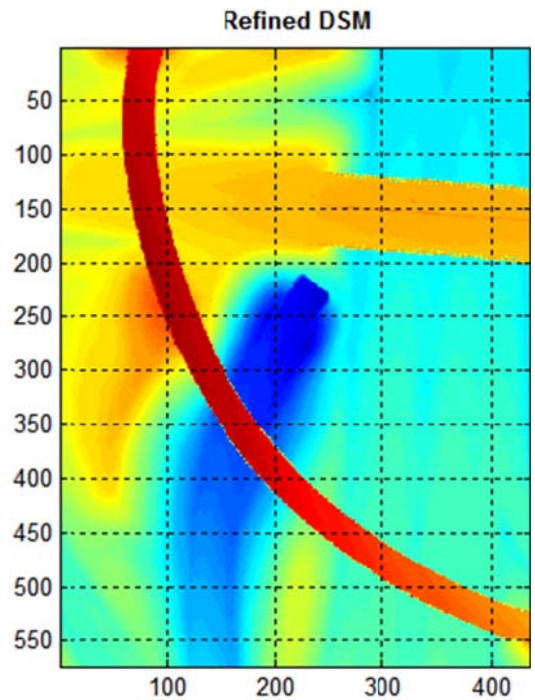

Figure 42 PDSM

The second approach extracts the smooth bridge boundaries from the geo-referenced aerial images, and then transforms them back to the LiDAR data domain via the collinearity equation. In some special cases, if no geo-referenced aerial image is available, a novel registration module developed is used to estimate the affine/perspective transformation between the LiDAR intensity and optical images; note this is the case for the third approach. Fig. 43 shows the workflow of both approaches; the only difference is that the registration is provided by collinearity equation or by the more generic registration method. Smooth bridge boundaries extraction is the comparable in both cases.

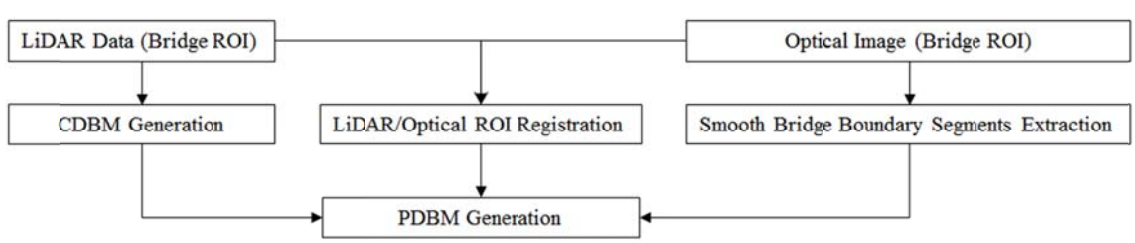

Figure 43 PDBM workflow.

Hough linear transform is applied to the bridge ROI in the aerial image to extract the bridge boundaries. For each Hough transform identified linear feature, its Hough transform angle is also recorded, which can be used to determine the bridge direction and remove the non-bridge linear features. For a long curved bridge, short linear features are extracted along the curved bridge boundaries. Since Hough linear transform cannot be directly used to extract long curved bridge boundaries, the long curved bridge ROI is divided into several small sub ROIs, as shown in Fig. 44. Then, it is possible to obtain short linear features in each sub ROI. Hough linear features in all sub ROIs are merged together to form the complete set of linear features along the long curved bridge boundaries.

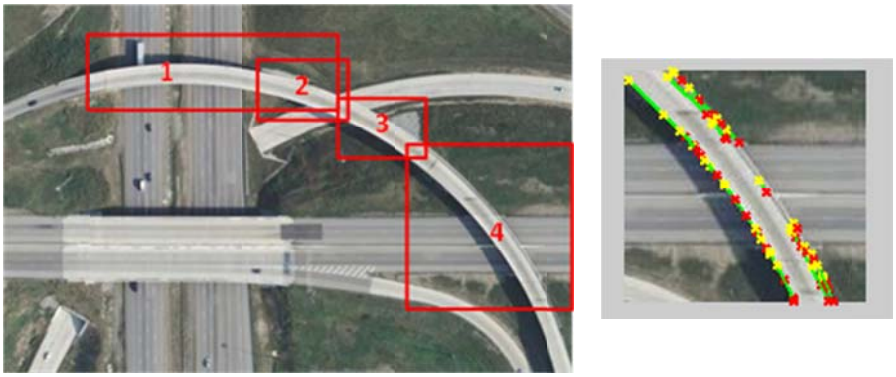

(a) (b)

Figure 44 Sub-ROIs of a curved bridge ROI (a), and short linear features in sub-ROI 4 (b).

It is also necessary to determine points of upper and lower boundaries for the smooth boundary generation. In order to simply separate the upper and lower boundaries, all linear features are rotated to align to the horizontal direction based on the recorded α angles. This step is performed in ROI for simple bridge or in each sub ROI for the curved bridge. If the bridge or bridge segment is rotated to horizontal direction, upper and lower boundaries can be separated based on comparing the Y coordinate. For straight bridge boundary, 1st order polynomial function is used to fitting those endpoints of linear features along the bridge boundary, and for curved bridge boundary, 2nd order polynomial function is used. Once the polynomial function parameters are estimated, the smooth boundary can be then represented in the dense sample points computed via the polynomial function.

6.4.3 Summary

The first approach is the fastest approach, as it does not require any aerial images and is only based on LiDAR data. The second approach is straightforward if the EOPs (Exterior Orientation Parameters) are precise. The third approach is used in the cases if no geo-referenced aerial imagery is available. A few PDBM figures are included in the Appendix (11.3).

6.5 True Orthophoto Generation

6.5.1 Occlusion Detection

Z-buffer and angle-based methods are used to detect the occluded cells. As we are interested in the occluded cells caused by the bridge boundary, the occlusion detection is only performed around the bridge boundary, which will largely reduce the computation load. Fig. 45 shows the occlusion detection interface.

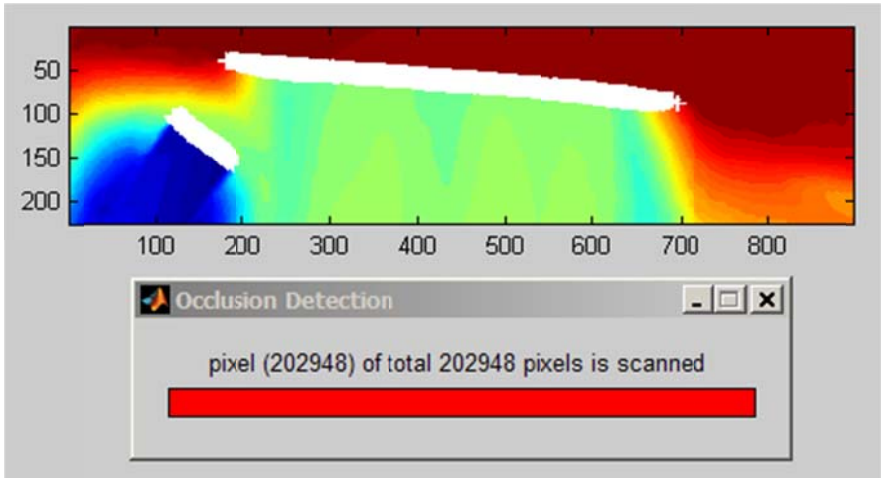

Figure 45 Occlusion detection results, bridge low boundary DSM sub-ROI (Franklin County).

6.5.2 PDSM Problem

It was noticed that irregular distortions along the bridge boundaries in our orthophoto/true orthophoto occurred at a GSD of 0.25 foot, see Figure 46.

Figure 46 Bridge boundary area in the true orthophoto (GSD=0.25 foot).

First, it was thought that the rails are the reason for the above distortion, but it turned out not true. The effect of the height variation of the rails is relatively small in the orthophoto. Then, looking at the DSM carefully, it was figured that the real reason was still the DSM itself. First, Fig. 47 shows the 3D plot of the refined PCD, the bridge boundary, the same boundary shown in the Fig. 46, is very precise, clean and smooth. It is generated from PCDProcessing.

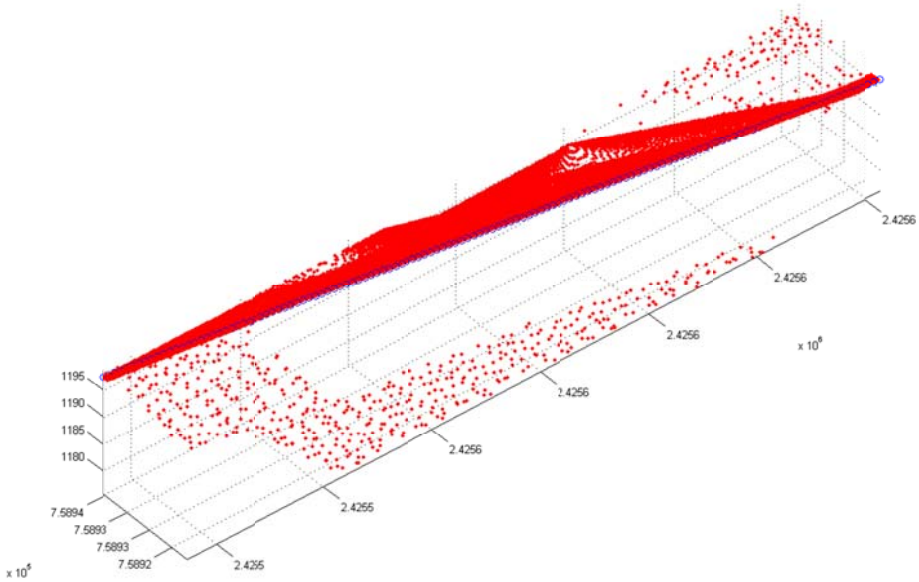

Figure 47 Point cloud of the bridge boundary (red points), smooth bridge boundary points (blue circles).

The next step is to use LASTool las2dem.exe to generate the DSM. If the bridge boundary points and ground points on the generated DSM are plotted, the problem becomes visible, see Figs. 48 and 49. Note that the ground points are pretty sparse in comparison with bridge points. In addition, 0.25 foot GSD is too small for those ground points, so there must be some void cells, which are filled based on the elevation values of neighboring cells. This is the real reason, why the DSM is not smooth on the bridge boundary. Unfortunately, DSM generated from the precise bridge model is not smooth enough on the bridge boundary, which can eventually degrade the orthophoto product quality.

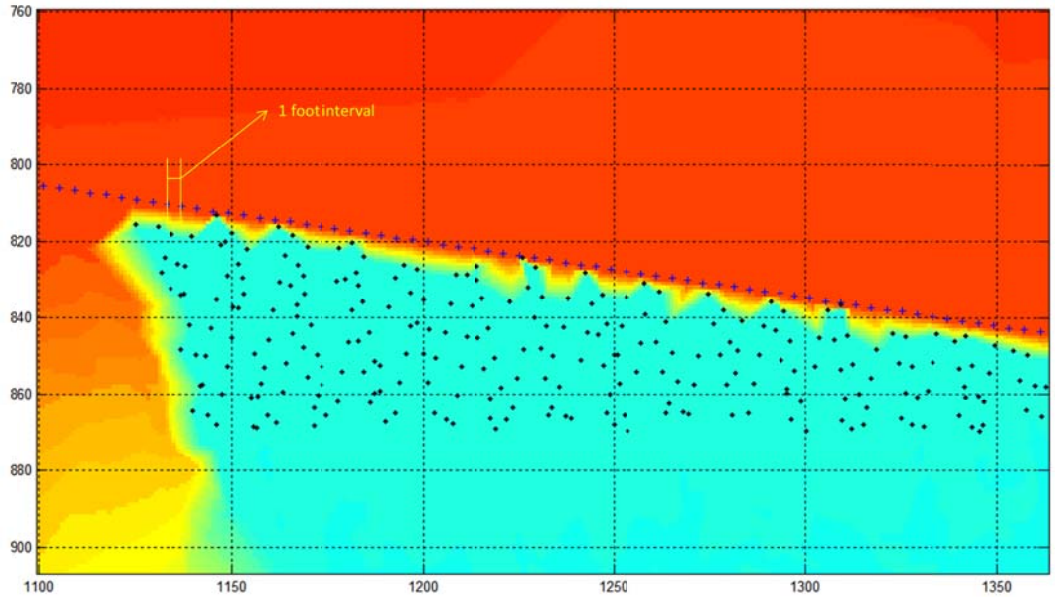

Figure 48 0.25 foot DSM (background), ground points around the bridge (black points), bridge boundary points (blue cross).

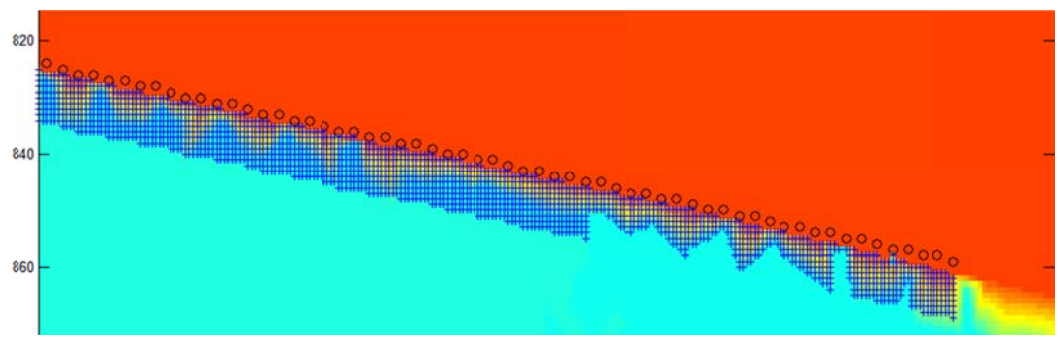

Figure 49 Detected cells (blue cross), and bridge boundary points (circle).

A further refinement of the DSM is required on the bridge boundary area. Fortunately, bridge boundary location is well known on the DSM, and ground points are also known. Based on this information, all those DSM cells transition from bridge to ground are detected. Those cells are filled with the average ground height. Then, the new DSM is used to generate orthophoto/true orthophoto, see Figs. 50 and 51.

Figure 50 Refined DSM.

Figure 51 0.25 foot true orthophoto of the bridge lower boundary area.

In conclusion, 0.25 ft orthophoto/true orthophoto is a challenge using current LiDAR data (spatial resolution). However, it is still possible to achieve better results if the developed software to manipulate the smooth bridge boundaries is carefully used. For this purpose, additional routines are provided for the user to manipulate the bridge boundaries in the PDSM to achieve the best true orthophoto quality.

6.5.3 Summary

Generally speaking, the true orthophoto resolution is highly dependent on the PDSM resolution. If they do not match, for example, DSM resolution is only 1 foot, it is hard to obtain a 0.25 foot true orthophoto. The developed PDBM is based on a very dense point cloud, as additional points are inserted to smooth bridge boundaries. Then, the PDSM of the bridge area may have good resolution, and possible to derive 0.25 foot level PDSM to produce the true orthophoto. Fig. 52 shows the orthophoto of one of the test sites with 0.5 ft resolution.

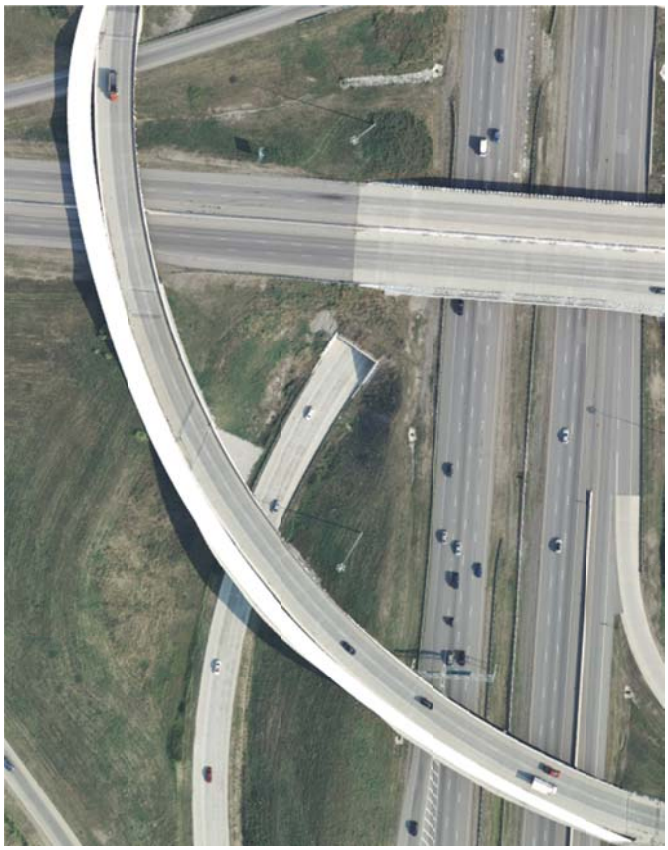

Figure 52 0.5 foot true orthophoto with white pixels in the occluded cells.

8. CONCLUSION

The DMC system procured in the project represented the state-of-the-art in large-format digital aerial camera systems at the start of project. DMC is based on the frame camera model, and to achieve large ground coverage with high spatial resolution, the output image is formed from four independent images acquired by four cameras. Color provided by pan-sharpening, using four cameras covering the entire FOV of the system. Due to its careful design, the DMC system has high optical, mechanical and electrical stability, providing an unprecedentedly high image quality. Note that the image radiometry is superior compared to film-based cameras, and thus greatly facilities any image processing tasks. As it is always the case with technology, a few years can make a big difference, and the new version of the camera family, the DMC-II, raises the bar even further by providing larger FOV and significantly higher spatial resolution. Note that the DMC-II has a 250 Mpixel single CCD sensor, compared to the DMC four 28 Mpixel camera head, which provides an about 100 Mpixel image.

The DMC has been carefully tested to assess its performance level. Out of the two test flights, the first one was flown in snowy conditions, so the second set flown in April 2011 was used. Three different blocks were selected, representing different flying condition and flight geometry. Five methods were used for the performance evaluation, including two methods where self-calibration was also introduced. The analysis of the results confirmed that the DMC meets the manufacturer's specification. To maintain consistent performance in regular operations, calibration flight and the use of ground controls as check point is highly recommended. In addition to further support QA/QC, the use of automated aerial triangulation is also suggested.

The main product of the ODOT Office of Mapping and CADD Services is orthophoto, which is widely used in many applications at ODOT and other State offices. Since ODOT primarily acquire data over the transportation network, the orthophoto production has some specific needs, such as dealing with bridges and occlusions, besides the general tasks of the orthoimage workflow. In this project, an innovative method was developed to support the orthoimage generation at bridges. The concept is built around a development of a precise bridge model, which is formed from the DMC imagery and LiDAR data. To address the second problem, a true orthophoto generation process was implemented. The initial versions of both software have been installed at Office of Mapping and CADD Services for testing and collecting feedback for refinement.

9. IMPLEMENTATION PLAN

The OSU-developed code in Matlab will be updated by the official end of the project. For a short time, we expect to support ODOT personnel to assure a smooth introduction of the tools to production.

10. REFERENCES

Ahokas, E., Kaassalainen, S., Hyyppa, J. and Suomalainen, J., 2006. Calibration of the Optech ALTM 3100 Laser Scanner Intensity Data Using Brightness Targets, Proceedings of ISPRS Commission I. Symposium.

R.Alamus, W.Kornus, I. Riesinger. (2007). DMC Geometric Performance Analysis. *ISPRS.* Hannover.

ASPRS LiDAR Committee, 2004. ASPRS Guidelines Vertical Accuracy Reporting for LiDAR Data, http://www.asprs.org/society/committees/lidar/Downloads/Vertical_Accuracy_Reporting_for_Lidar_Data.pdf

Baltsavias, E.P., 1999. Airborne Laser Scanning: Basic Relations and Formulas. *ISPRS Journal of Photogrammetry & Remote Sensing,* Vol. 54: 199-214.

Behan, A., 2000. On the Matching Accuracy of Rasterized Scanning Laser Altimeter Data. *International Archives of Photogrammetry and Remote Sensing*, 33 (Part 2B): 75-82.

Burman, H., 2000. Calibration and Orientation of Airborne Image and Laser Scanner Data Using GPS and INS, Ph.D. Thesis, Geodesy and Photogrammetry. Royal Institute of Technology, Stockholm. 107 p.

Burman, H. ,2002. Laser Strip Adjustment for Data Calibration and Verification. *International Archives of Photogrammetry and Remote Sensing*, 34 (Part 3A): 67-72.

Crombaghs, M. J.E., R. Brügelmann, E.J. de Min, 2000. On the Adjustment of Overlapping Strips of Laseraltimeter Height Data. *International Archives of Photogrammetry and Remote Sensing*, 33, (Part B3/1):224-231.

Csanyi N. and Toth C., 2004. On Using LiDAR-specific Ground Targets, ASPRS Annual Conference, Denver, CO, May 23-28, CD-ROM.

Csanyi N, Toth C., Grejner-Brzezinska D. and Ray J., 2005. Improving LiDAR data accuracy using LiDAR-specific ground targets, ASPRS Annual Conference, Baltimore, MD, March 7-11, CD-ROM.

Csanyi, N. and Toth, C., 2006. Improvement of LiDAR Data Accuracy Using LiDAR-Specific Ground Targets, *Photogrammetric Engineering & Remote Sensing*, (in press).

Cramer, Michael, Norbert Haala. (1999). Direct Exterior Orientation of Airborne Sensor - An Accuracy Investigation of an Integrated GPS/INS System.

Cramer, Michael. (2003). Integrated GPS/INS and Digital Aerial Triangulation - Recent Test Results. *ISPRS*, (pp. 161-172).

Dahai Guo, Lixin Wu, Qiu Li, Jianchao Wang, Xiongwei Zheng. (2006). A Comparsion of DG and GPS-Supported AT. *IEEE* .

Digital Mapping Camera System Brochure, Z/I Imaging, Intergraph.

Dörstel, C. (2003). DMC - Practical Experience and Photogrammetric System Performance. *49th Photogrammetric Week*, (pp. 59-65). Stuttgart.

Dörstel, C. (2005). DMC - The Most Versatile Digital Large Format Camera in the Market. *Photogrammetric Week 05*, (pp. 51-55). Stuttgart.

Duda R. O., Hart P. E., 1972. Use of the Hough Transformation to detect lines and curves in pictures, *Graphics and Image processing*, 15: 11-15.

Filin, S., 2003. Recovery of Systematic Biases in Laser Altimetry Data Using Natural Surfaces. *ISPRS Journal of Photogrammetric Engineering and Remote Sensing* 69, 1235-1242.

Filin, S., 2003. Analysis and Implementation of a Laser Strip Adjustment Model. *International Archives of Photogrammetry and Remote Sensing*, 34 (Part 3/W13): 65-70.

Filin, S., and Vosselman, G., 2004. Adjustment of Airborne Laser Altimetry Strips. International Archives of Photogrammetry, *Remote Sensing and Spatial Information Sciences* 34 (Part B) pp. 285-289.

Grejner-Brzezinksa, D. A. (1999). Direct Exterior Orientation of Airborne Imagery with GPS/INS System - Performance Analysis. *Navigation* , 261-270.

D.A. Grejner-Brzezinska, C. Toth, E. Paska . (2007). Airborne Remote Sensing Supporting Traffic Flow Estimation. In J. L. C. V. Tao, *Advances in Mobile Mapping Technology* (pp. 51-60).

Gruber, Michael, Richard Ladstädter. (2008). Geometric Aspects Concerning the Photogrammetric Workflow of the Digital Aerial Camera UCX. *ISPRS Beijing*, (p. 524). Beijing.

Hasegawa, H., 2006. Evaluations of LiDAR Reflectance Amplitude Sensitivity Towards Land Cover Conditions, *Bulletin of the Geographical Survey Institute*, Vol. 53.

Heier, Helmut, Michael Kiefner, Wolfgang Zeitler. (2003). Calibration of the Digital Modular Camera. *FIG XII International Congress.* Washington, D.C.

Heipke, Christian, Karsten Jacobsen, Helge Wegmann. (2001). The OEEPE Test On Integrated Sensor Orientation. *OEEPE Workshop of "Integrated Sensor Orientation"* , 53-62.

Intergraph. (2008). Digital Mapping Camera System - Optimize the Accuracy of Your Data Acquisition.

Jacobsen, K. (2003). System Calibration for Direct and Integrated Sensor Orientation. *ISPRS WG I/5, Barcelona.* Barcelona.

Kaassalainen, S., Ahokas, E., Hyyppa, J. and Suomalainen, J., 2005. Study of Surface Brightness from Backscattered Laser Intensity: Calibration of Laser Data, *IEEE Geoscience and Remote Sensing Letters*, 2(3):255-259.

Kager, H. and Kraus, K., 2001. Height Discrepancies between Overlapping Laser Scanner Strips. Proceedings of Optical 3D Measurement Techniques V, October, Vienna, Austria: 103-110.

Katzernbeisser, R., 2003. About the Calibration of LiDAR Sensors. Proc. ISPRS Workshop 3-D Reconstruction from Airborne Laser-Scanner and InSAR data, Dresden, Germany, 8-10 October. 6 p. (on CDROM).

Kilian J., Haala, N., Englich, M., 1996. Capture and Evaluation of Airborne Laser Scanner Data. *International Archives of Photogrammetry and Remote Sensing*, 31 (Part B3):383-388.

Kraus, K. (2004). *Photogrammetrie Band I, II.* Germany: Walter de Gruyter GmbH & Co. KG.

Kremer, J. (2006). *Precise Flight Planning and Guidance for Airborne Sensors - and More.* Bogata.

Leica Geosystems, ALS50, http://gis.leica-geosystems.com

Lichti, D., 2004. A Resolution Measure for Terrestrial Laser Scanners. International Archives of Photogrammetry, *Remote Sensing and Spatial Information Sciences* 34 (Part B) pp. 552-558.

Lutz, E., Geist, Th. and Stötter, J., 2003. Investigations of Airborne Laser Scanning Signal Intensity on Glacial Surfaces - Utilizing Comprehensive Laser Geometry Modeling and Orthophoto Surface Modeling (A Case Study: Svartisheibreen, Norway), proceedings of ISPRS Commission III, WG 3.

Maas, H.-G., 2000. Least Squares Matching with Airborne Laserscanning Data in a TIN Structure. *International Archives of Photogrammetry and Remote Sensing*, 33 (Part B3/1): 548-555.

Maas, H.-G., 2001. On the Use of Pulse Reflectance Data for Laserscanner Strip Adjustment. International Archives of Photogrammetry, *Remote Sensing and Spatial Information Sciences*, 33 (Part 3/W4): 53-56.

Morin, K., and El-Sheimy, N., 2002. Post-mission Adjustment of Airborne Laser Scanning Data. Proc. FIG XXII International Congress, Washington DC, USA. 12 p. (on CD-ROM)

Nobrega, R. and O'Hara, C., 2006. Segmentation and Object Extraction from Anisotropic Diffusion Filtered LiDAR Intensity Data.

Optech International, 2004. ALTM 30/70/100 User Manual. Toronto, Canada.

Optech, ALTM 3100AE, 2006, http://www.optech.ca/pdf/Brochures/ALTM3100EAwspecsfnl.pdf

Renslow, M., 2005. The Status of LiDAR Today and Future Directions, 3D Mapping from InSAR and LiDAR, ISPRS WG I/2 Workshop, Banff, Canada, June 7-10, CD-ROM.

K.P. Schwarz, N. El-Sheimy. (2004). Digital Mobile Mapping System - State of Art and Future Trends. *The XXth ISPRS Congress.* Istanbul.

Sithole, G., 2005. Segmentation and Classification of Airborne Laser Scanner Data, Publication of Geodesy 59, Nederlandse Commissie voor Geodesie, Delft (184 pages).

Skaloud, J., and Schaer, P., 2003. Towards A More Rigorous Bore-sight Calibration. Proc. ISPRS International Workshop on Theory Technology and Realities of Inertial/GPS/Sensor Orientation, Castelldefels, Spain, 22-23 September. 9 p. (on CD-ROM).

Soininen, A., and Burman, H., 2005. TerraMatch for MicroStation. Terrasolid Ltd., Findland.

Song, J-H., Han, S-H., Yu, K, and Kim, Y., 2002. Assessing the Possibility of Land-Cover Classification Using LiDAR Intensity Data, *International Archives of Photogrammetry*, 34. pp. 4.

Toth, C. (1999). Experiences with Frame CCD Arrays and Direct Georeferencing. *Photogrammetric Week.* Stuttgart.

Toth C. K., Calibrating Airborne LIDAR Systems, ISPRS Commission II Symposium on Integrated Systems for Spatial Data Production, Custodian and Decision Support, *International Archives of Photogrammetry and Remote Sensing*, Vol. XXXIV, part 2, pp.475-480, 2002.

Toth, C., 2004. Future Trends in LiDAR, Proc. ASPRS 2004 Annual Conference, Denver, CO, May 23-28, CD-ROM.

Toth Ch.K. and Csanyi N., 2001. Automating the LIDAR Boresight Misalignment, ISPRS WGII/2 Workshop on Three-Dimensional Mapping from InSAR and LIDAR, Banff, Alberta, Canada, 11-13 July, CD-ROM.

Toth C., Csanyi N. and Grejner-Brzezinska D. 2002. Automating the Calibration of Airborne Multisensor Imaging Systems, Proc. ACSM-ASPRS Annual Conference, Washington, DC, April 19-26, CD ROM.

Toth, C. and Grejner-Brzezinska, D., 2005. Geo-referenced Digital Data Acquisition and Processing Systems Using LiDAR Technology – Final report, ODOT State Job No. 147990.

Vosselman, G., and Mass, H.-G., 2001. Adjustment and Filtering of Raw Laser Altimetry Data. Proc. OEEPE Workshop on Airborne Laserscanning and Interferometric SAR for Detailed Digital Elevation Models. OEEPE Publication 40, Stockholm, Sweden. pp. 62-72.

Vosselman, G., 2002. On the Estimation of Planimetric Offsets in Laser Altimetry Data. *International Archives of Photogrammetry and Remote Sensing*, 34 (Part 3A): 375-380.

Vosselman, G., 2002. Strip Offset Estimation Using Linear Features. 3rd International LIDAR Workshop, October 7-9, Columbus,

http://www.itc.nl/personal/vosselman/papers/vosselman2002.columbus.pdf

"What is Bundle block Adjustment?." Lidar & Photogrammetry Development. Lidar & Photogrammetry Development, n.d. Web. 26 Jul 2011. http://photogrammetrydevelopment.blogspot.com/2010/12/what-is-bundle-block-adjustment.html

Yastikli, N. (2004). The Effect of System Calibration on Direct Sensor Orientation. *ISPRS Congress 2004.* Istanbul.

Yastikli, N.; Jacobsen, K. (2005). Influence of System Calibration to Direct Sensor Orientation. *PE&RS 71* , Nr. 5, S. 629-633.

Yuan, X. (2009). Quality Assessment for GPS-Supported Bundle Block Adjustment Based on Aerial Digital Frame Imagery. *The Photogrammetric Record 24 (126)* , 139-156.

11. APPENDIX

11.1 Camera Performance Validation Test Results

11.1.1 Test Block 1

11.1.1.1 Method 1

The Residual of the Ground Control Points of IOP Fixed and EOP Initial using IDG				
Point ID	**rX [m]**	**rY [m]**	**rZ [m]**	**rD [m]**
7	0.12	-0.13	0.26	0.31
19	-0.01	0.00	-0.02	0.02
21	0.00	-0.02	0.00	0.02
31	-0.08	-0.01	0.09	0.12
32	-0.05	0.16	0.28	0.33
Max	0.12	0.16	0.28	0.33
Min	0.00	0.00	0.00	0.02
Mean	0.00	0.00	0.12	0.16
SD	0.08	0.10	0.14	0.15

The Residual of the Check Points of IOP Fixed and EOP Initial using IDG				
Point ID	**rX [m]**	**rY [m]**	**rZ [m]**	**rD [m]**
8	0.04	0.02	-0.11	0.12
17	0.07	-0.01	-0.20	0.21
18	-0.08	-0.10	0.08	0.15
22	-0.05	-0.09	0.18	0.21
Max	0.08	0.10	0.20	0.21
Min	0.04	0.01	0.08	0.12
Mean	-0.01	-0.04	-0.01	0.17
SD	0.08	0.06	0.17	0.05

GCPs 19, 21, 31, 32 horizontal precision achieve theretical precision; residuals on GCP 7 is higher than others. All vertical values are under 29 cm. Check Point (CP), horizontal accuracy are from 1 cm to 10 cm; it falls in the expected accuracy range.

11.1.1.2 Method 2

The Residual of the Ground Control Points of Self-Calibration and EOP Initial using IDG				
Point ID	**rX [m]**	**rY [m]**	**rZ [m]**	**rD [m]**
7	0.12	-0.13	0.27	0.32
19	-0.01	0.00	-0.01	0.01
21	0.00	-0.02	-0.01	0.02
31	-0.09	-0.01	0.12	0.15
32	-0.05	0.16	0.30	0.35
Max	0.12	0.16	0.30	0.35
Min	0.00	0.00	0.01	0.01
Mean	-0.01	0.00	0.13	0.17
SD	0.08	0.11	0.15	0.16

The Residual of the Check Points of Self-Calibration and EOP Initial using IDG				
Point ID	**rX [m]**	**rY [m]**	**rZ [m]**	**rD [m]**
8	0.05	0.00	-0.11	0.12
17	0.07	-0.01	-0.17	0.18
18	-0.08	-0.12	0.11	0.18
22	-0.06	-0.10	0.22	0.25
Max	0.08	0.12	0.22	0.25
Min	0.05	0.00	0.11	0.12
Mean	-0.01	-0.06	0.01	0.18
SD	0.08	0.06	0.18	0.05

These tables represent almost the same results as of Method 1, which means that that the self-calibration does not bring in much improvement to the block adjustment; see Tables below

The Effect of Self-Calibration on Ground Control Points				
Point ID	**ΔrX [m]**	**ΔrY [m]**	**ΔrZ [m]**	**ΔrD [m]**
7	0.00	0.00	-0.01	-0.01
8	0.00	0.00	0.00	0.00
17	0.00	0.00	0.01	0.00
18	0.01	0.00	-0.03	-0.03
19	0.01	0.00	-0.02	-0.02
Max	0.01	0.00	0.03	0.03
Min	0.00	0.00	0.00	0.00
Mean	0.00	0.00	-0.01	-0.01
SD	0.00	0.00	0.02	0.01

The Effect of Self-Calibration on Ground Check Points				
Point ID	**ΔrX [m]**	**ΔrY [m]**	**ΔrZ [m]**	**ΔrD [m]**
7	-0.01	0.02	0.00	0.00
8	0.01	0.00	-0.03	0.03
17	0.00	0.02	-0.03	-0.03
18	0.01	0.00	-0.03	-0.03
Max	0.01	0.02	0.03	0.03
Min	0.00	0.00	0.00	0.00
Mean	0.00	0.01	-0.02	-0.01
SD	0.01	0.01	0.01	0.03

11.1.1.3 Method 3

The Residual of the Ground Control Points of IOP Fixed and EOP Fixed using IDG				
Point ID	**rX [m]**	**rY [m]**	**rZ [m]**	**rD [m]**
19	-0.30	-0.10	0.04	0.31
21	-0.28	-0.11	0.37	0.47
Max	0.30	0.11	0.37	0.47
Min	0.28	0.10	0.04	0.31
Mean	-0.29	-0.10	0.20	0.39
SD	0.01	0.01	0.23	0.11

The Residual of the Check Points of IOP Fixed and EOP Fixed using IDG				
Point ID	**rX [m]**	**rY [m]**	**rZ [m]**	**rD [m]**
7	-0.50	-0.20	0.88	1.03
8	-0.60	0.06	0.34	0.69
17	-0.49	0.01	0.15	0.51
18	-0.73	-0.06	0.52	0.90
22	-0.61	-0.05	0.47	0.77
31	-0.62	0.03	0.35	0.71
32	-0.53	0.17	0.55	0.78
Max	0.73	0.20	0.88	1.03
Min	0.49	0.01	0.15	0.51
Mean	-0.58	0.00	0.47	0.77
SD	0.08	0.12	0.23	0.16

These results are worse than Method 1 and 2; X residuals (Easting) of GCPs and CPs are generally larger than Y (Northing). The reason could be 900 m sub-blcok is north-south direction which causes the easting direction precision/accuracy to be larger.

11.1.1.4 Method 4

The Residual of the Ground Control Points of Self-Calibration and EOP Fixed using IDG				
Point ID	**rX [m]**	**rY [m]**	**rZ [m]**	**rD [m]**
19	-0.17	0.01	-0.11	0.21
21	-0.12	-0.05	-0.03	0.14
Max	0.17	0.05	0.11	0.21
Min	0.12	0.01	0.03	0.14
Mean	-0.15	-0.02	-0.07	0.17
SD	0.03	0.04	0.06	0.05

The Residual of the Check Points of Self-Calibration and EOP Fixed using IDG				
Point ID	**rX [m]**	**rY [m]**	**rZ [m]**	**rD [m]**
7	-0.14	-0.43	0.14	0.47
8	-0.23	-0.16	-0.30	0.41
17	-0.13	-0.21	-0.43	0.50
18	-0.36	-0.28	-0.20	0.50
22	-0.25	-0.28	-0.14	0.40
31	-0.25	-0.19	-0.26	0.41
32	-0.16	-0.07	-0.09	0.19
Max	0.36	0.43	0.43	0.50
Min	0.13	0.07	0.09	0.19
Mean	-0.22	-0.23	-0.19	0.41
SD	0.08	0.11	0.18	0.11

When self-calibration is applied, the residuals are clearly improved. However, CPs residuals are still larger than the expected 9cm and 29cm; also, there is some inconsistency with the GCPs. Comparing Methods 3, see Tables below.

The Effect of Self-Calibration on Ground Control Points				
Point ID	**ΔrX [m]**	**ΔrY [m]**	**ΔrZ [m]**	**ΔrD [m]**
19	-0.13	-0.11	0.15	0.11
21	-0.15	-0.06	0.40	0.34
Max	0.15	0.11	0.40	0.34
Min	0.13	0.06	0.15	0.11
Mean	-0.14	-0.08	0.27	0.22
SD	0.02	0.03	0.18	0.16

The Effect of Self-Calibration on Ground Check Points				
Point ID	**ΔrX [m]**	**ΔrY [m]**	**ΔrZ [m]**	**ΔrD [m]**
7	-0.37	0.23	0.74	0.56
8	-0.37	0.22	0.65	0.28
17	-0.36	0.23	0.58	0.01
18	-0.37	0.23	0.73	0.40
22	-0.36	0.22	0.61	0.37
31	-0.37	0.22	0.61	0.30
32	-0.37	0.24	0.64	0.59
Max	0.37	0.24	0.74	0.59
Min	0.36	0.22	0.58	0.01
Mean	-0.37	0.23	0.65	0.36
SD	0.00	0.01	0.06	0.19

Self-calibration brings in some improvement; though, it is not sufficient. This is an indication that the aerial position data does not match the ground truth completely.

11.1.1.5 Method 5

Ground Control Position Differences Using DG (Computed - Given)				
Point ID	**ΔX [m]**	**ΔY [m]**	**ΔZ [m]**	**ΔD [m]**
7	-0.45	-0.25	0.81	0.96
8	-0.52	-0.05	0.42	0.67
17	-0.42	-0.06	0.14	0.45
18	-0.59	0.49	0.53	0.94
19	-0.25	-0.07	0.13	0.29
21	-0.24	-0.10	0.37	0.45
22	-0.54	-0.13	0.47	0.72
31	-0.54	-0.04	0.35	0.65
32	-0.45	0.10	0.55	0.72
Max	0.59	0.49	0.81	0.96
Min	0.24	0.04	0.13	0.29
Mean	-0.44	-0.01	0.42	0.65
SD	0.12	0.21	0.21	0.22

The differences are shown based on the coordinates computed by DG; note the data was provided by ODOT.

11.1.2 Test Block 2

The Residual of the Ground Control Points of IOP Fixed and EOP Initial using IDG				
Point ID	**rX [m]**	**rY [m]**	**rZ [m]**	**rD [m]**
1	-0.33	0.02	-0.42	0.53
2	-0.18	0.21	-0.07	0.29
4	0.02	-0.03	-0.08	0.09
5	0.01	0.07	0.49	0.50
Max	0.33	0.21	0.49	0.53
Min	0.01	0.02	0.07	0.09
Mean	-0.12	0.07	-0.02	0.35
SD	0.17	0.10	0.38	0.21

The Residual of the Check Points of IOP Fixed and EOP Initial using IDG				
Point ID	**rX [m]**	**rY [m]**	**rZ [m]**	**rD [m]**
3	-0.03	0.05	-0.02	0.06

Horizontal residuals on GCPs 1 and 2 are larger than 4.5cm, and vertical residuals on GCPs 1 and 5 are also larger than 14cm. Note the CPs show good residuals.

11.1.2.1 Method 2

The Residual of the Ground Control Points of Self-Calibration and EOP Initial using IDG				
Point ID	**rX [m]**	**rY [m]**	**rZ [m]**	**rD [m]**
1	-0.05	-0.04	-0.11	0.13
2	0.03	0.03	0.07	0.09
4	-0.01	-0.07	-0.04	0.08
5	0.00	0.06	0.11	0.13
Max	0.05	0.07	0.11	0.13
Min	0.00	0.03	0.04	0.08
Mean	-0.01	0.00	0.01	0.11
SD	0.03	0.06	0.10	0.03

The Residual of the Check Points of Self-Calibration and EOP Initial using IDG				
Point ID	**rX [m]**	**rY [m]**	**rZ [m]**	**rD [m]**
3	-0.11	-0.03	-0.13	0.17

When self-calibration is applied, results have improved significantly; residuals at GCPs are all in the range of the expected values. Comparison between Methods 1 and 2 are in the Tables below.

The Effect of Self-Calibration on Ground Control Points				
Point ID	**ΔrX [m]**	**ΔrY [m]**	**ΔrZ [m]**	**ΔrD [m]**
1	-0.28	0.07	-0.30	0.40
2	-0.22	0.18	-0.15	0.20
4	0.03	0.03	-0.04	0.01
5	0.01	0.01	0.38	0.37
Max	0.28	0.18	0.38	0.40
Min	0.01	0.01	0.04	0.01
Mean	-0.11	0.07	-0.03	0.25
SD	0.16	0.07	0.29	0.18

The Effect of Self-Calibration on Ground Check Points				
Point ID	**ΔrX [m]**	**ΔrY [m]**	**ΔrZ [m]**	**ΔrD [m]**
7	0.08	0.08	0.12	-0.11

11.1.2.2 Method 3

The Residual of the Ground Control Points of IOP Fixed and EOP Fixed using IDG				
Point ID	**rX [m]**	**rY [m]**	**rZ [m]**	**rD [m]**
3	-0.24	0.02	0.20	0.31

The Residual of the Check Points of IOP Fixed and EOP Fixed using IDG				
Point ID	**rX [m]**	**rY [m]**	**rZ [m]**	**rD [m]**
1	-0.32	0.05	-0.31	0.44
2	-0.24	0.21	0.19	0.37
4	-0.25	0.01	0.24	0.35
5	-0.23	0.00	0.24	0.34
Max	0.00	0.10	0.01	0.05
Min	0.00	0.00	0.01	0.01
Mean	-0.26	0.07	0.09	0.37
SD	0.04	0.10	0.27	0.05

Horizontal residuals of the X components at CPs are generally larger than Y components; X is easting (which is cross flight direction, which provides less overlap than along flight direction).

11.1.2.3 Method 4

The Residual of the Ground Control Points of Self-Calibration and EOP Fixed using IDG				
Point ID	**rX [m]**	**rY [m]**	**rZ [m]**	**rD [m]**
3	-0.24	0.02	0.19	0.30

The Residual of the Check Points of Self-Calibration and EOP Fixed using IDG				
Point ID	**rX [m]**	**rY [m]**	**rZ [m]**	**rD [m]**
1	-0.32	-0.06	-0.32	0.45
2	-0.24	0.11	0.17	0.31
4	-0.25	0.01	0.23	0.34
5	-0.23	0.00	0.24	0.33
Max	0.32	0.11	0.32	0.45
Min	0.23	0.00	0.17	0.31
Mean	-0.26	0.02	0.08	0.36
SD	0.04	0.07	0.27	0.06

Self-calibration does not show improvement on the results. Comparison of Methods 3 and 4 shows consistency, see Tables below.

The Effect of Self-Calibration on Ground Control Points				
Point ID	**ΔrX [m]**	**ΔrY [m]**	**ΔrZ [m]**	**ΔrD [m]**
3	0.00	0.00	0.01	0.01

The Effect of Self-Calibration on Ground Check Points				
Point ID	**ΔrX [m]**	**ΔrY [m]**	**ΔrZ [m]**	**ΔrD [m]**
1	0.00	0.10	0.01	-0.01
2	0.00	0.10	0.01	0.05
4	0.00	0.00	0.01	0.01
5	0.00	0.00	0.01	0.01
Max	0.00	0.10	0.01	0.05
Min	0.00	0.00	0.01	0.01
Mean	0.00	0.05	0.01	0.02
SD	0.00	0.06	0.00	0.03

11.1.2.4 Method 5

Ground Control Position Differences Using DG (Computed - Given)				
Point ID	**ΔX [m]**	**ΔY [m]**	**ΔZ [m]**	**ΔD [m]**
1	10.94	6.67	-0.81	12.84
2	4.48	2.58	-0.17	5.18
3	-0.21	0.00	0.34	0.40
4	-0.28	0.07	0.43	0.52
5	-0.27	0.02	0.28	0.39
Max	10.94	6.67	0.81	12.84
Min	0.21	0.00	0.17	0.39
Mean	2.93	1.87	0.02	3.86
SD	4.92	2.90	0.52	5.42

The differences are shown based on those computed using DG (provided by ODOT). The results are good for points 3, 4 and 5, while points 1 and 2 yield high differences. Points 1 and 2 are measured on images 1 and 2 and may have an EOP issue.

11.1.3 Test Block 3

11.1.3.1 Method 1

The Residual of the Ground Control Points of IOP Fixed and EOP Initial using IDG				
Point ID	**rX [m]**	**rY [m]**	**rZ [m]**	**rD [m]**
1	-0.04	-0.11	-0.23	0.26
4	-0.01	-0.01	0.13	0.13
5			-0.02	0.02
6	0.00	0.00	0.00	0.00
7	0.00	-0.05	-0.05	0.07
9	-0.06	0.06	0.15	0.17
Max	0.06	0.11	0.23	0.26
Min	0.00	0.00	0.00	0.00
Mean	-0.02	-0.02	0.00	0.11
SD	0.02	0.06	0.14	0.10

The Residual of the Check Points of IOP Fixed and EOP Initial using IDG				
Point ID	**rX [m]**	**rY [m]**	**rZ [m]**	**rD [m]**
3	-0.02	0.04	-0.03	0.06
8	0.03	-0.05	-0.40	0.40
Max	0.03	0.05	0.40	0.40
Min	0.02	0.04	0.03	0.06
Mean	0.00	-0.01	-0.21	0.23
SD	0.03	0.07	0.26	0.24

All residuals at GCPs are under 9 cm and 29 cm; the theoretical limit. Residuals on CPs are also acceptable, only residual on GCP 8 is large in the z-direction.

11.1.3.2 Method 2

The Residual of the Ground Control Points of Self-Calibration and EOP Initial using IDG				
Point ID	**rX [m]**	**rY [m]**	**rZ [m]**	**rD [m]**
1	-0.04	-0.11	-0.23	0.25
4	-0.01	-0.01	0.12	0.12
5			-0.02	0.02
6	0.00	0.00	0.00	0.00
7	0.00	-0.05	-0.06	0.08
9	-0.06	0.06	0.15	0.17
Max	0.06	0.11	0.23	0.25
Min	0.00	0.00	0.00	0.00
Mean	-0.02	-0.02	0.00	0.11
SD	0.02	0.06	0.14	0.10

The Residual of the Check Points of Self-Calibration and EOP Initial using IDG				
Point ID	**rX [m]**	**rY [m]**	**rZ [m]**	**rD [m]**
3	-0.02	0.04	-0.03	0.06
8	0.03	-0.05	-0.41	0.41
Max	0.03	0.05	0.41	0.41
Min	0.02	0.04	0.03	0.06
Mean	0.01	-0.01	-0.22	0.23
SD	0.03	0.07	0.26	0.25

Self-calibration does not show improvement in the results. Comparison of Methods 1 and 2 shows consistency in the results, see Tables below.

The Effect of Self-Calibration on Ground Control Points				
Point ID	**ΔrX [m]**	**ΔrY [m]**	**ΔrZ [m]**	**ΔrD [m]**
1	0.00	0.00	0.00	0.00
4	0.00	0.00	0.01	0.01
5			0.00	0.00
6	0.00	0.00	0.00	0.00
7	0.00	0.00	0.01	-0.01
9	0.00	0.00	0.00	0.00
Max	0.00	0.00	0.01	0.01
Min	0.00	0.00	0.00	0.00
Mean	0.00	0.00	0.00	0.00
SD	0.00	0.00	0.01	0.01

The Effect of Self-Calibration on Ground Check Points				
Point ID	**ΔrX [m]**	**ΔrY [m]**	**ΔrZ [m]**	**ΔrD [m]**
3	0.00	0.00	0.00	0.00
8	0.00	0.00	0.01	-0.01
Max	0.00	0.00	0.01	0.01
Min	0.00	0.00	0.00	0.00
Mean	0.00	0.00	0.01	-0.01
SD	0.00	0.00	0.01	0.01

11.1.3.3 Method 3

The Residual of the Ground Control Points of IOP Fixed and EOP Fixed using IDG				
Point ID	**rX [m]**	**rY [m]**	**rZ [m]**	**rD [m]**
1	-0.05	-0.03	0.18	0.19
3	-0.05	0.04	0.12	0.14
Max	0.05	0.04	0.18	0.19
Min	0.05	0.03	0.12	0.14
Mean	-0.05	0.01	0.15	0.17
SD	0.00	0.05	0.04	0.04

The Residual of the Check Points of IOP Fixed and EOP Fixed using IDG				
Point ID	**rX [m]**	**rY [m]**	**rZ [m]**	**rD [m]**
4	-0.14	0.11	0.82	0.84
5			0.50	0.50
7	-0.51	-0.03	0.57	0.77
8	-0.15	0.02	0.47	0.49
9	-0.66	0.05	0.22	0.70
Max	0.66	0.11	0.82	0.84
Min	0.00	0.00	0.22	0.49
Mean	-0.36	0.04	0.52	0.66
SD	0.26	0.06	0.22	0.16

Residuals, in general, at GCPs are acceptable, while at CPs 7 and 9 are larger, and vertical is also larger.

11.1.3.4 Method 4

The Residual of the Ground Control Points of Self-Calibration and EOP Fixed using IDG				
Point ID	**rX [m]**	**rY [m]**	**rZ [m]**	**rD [m]**
1	-0.16	-0.07	-0.06	0.18
3	-0.16	0.01	-0.11	0.20
Max	0.16	0.07	0.11	0.20
Min	0.16	0.01	0.06	0.18
Mean	-0.16	-0.03	-0.09	0.19
SD	0.00	0.05	0.04	0.01

The Residual of the Check Points of Self-Calibration and EOP Fixed using IDG				
Point ID	**rX [m]**	**rY [m]**	**rZ [m]**	**rD [m]**
4	-0.25	0.07	0.59	0.64
5			0.25	0.25
7	-0.40	0.00	0.33	0.52
8	-0.26	-0.02	0.23	0.35
9	-0.55	0.09	-0.02	0.56
Max	0.55	0.09	0.59	0.64
Min	0.00	0.00	0.02	0.25
Mean	-0.36	0.04	0.28	0.46
SD	0.14	0.05	0.22	0.16

Residuals are improved slightly when applying self-calibration, but residuals on GCPs are generally larger than the theoretical accuracy. Residuals at CPs are good; X component is larger, but Y and Z are good. Comparing Methods 3 and 4, the differences are acceptable and show consistency of self-calibration, see Tables below.

The Effect of Self-Calibration on Ground Control Points				
Point ID	**ΔrX [m]**	**ΔrY [m]**	**ΔrZ [m]**	**ΔrD [m]**
1	0.11	0.04	0.24	0.01
3	0.11	0.03	0.24	-0.06
Max	0.11	0.04	0.24	0.06
Min	0.11	0.03	0.24	0.01
Mean	0.11	0.03	0.24	-0.02
SD	0.00	0.00	0.00	0.05

The Effect of Self-Calibration on Ground Check Points				
Point ID	**ΔrX [m]**	**ΔrY [m]**	**ΔrZ [m]**	**ΔrD [m]**
4	0.11	0.03	0.24	0.20
5			0.24	0.24
7	-0.11	-0.03	0.24	0.25
8	0.11	0.04	0.24	0.14
9	-0.11	-0.03	0.24	0.14
Max	0.11	0.04	0.24	0.25
Min	0.11	0.03	0.24	0.14
Mean	0.00	0.00	0.24	0.20
SD	0.13	0.04	0.00	0.05

11.1.3.5 Method 5

Ground Control Position Differences Using DG (Computed - Given)				
Point ID	**ΔX [m]**	**ΔY [m]**	**ΔZ [m]**	**ΔD [m]**
1	-0.20	0.01	0.10	0.22
3	0.51	0.33	-0.84	1.03
4	-0.20	0.20	0.85	0.90
5	0.22	-2.20	0.47	2.26
7	-0.43	-0.11	0.57	0.72
8	-0.10	0.14	0.68	0.70
9	-0.59	-0.02	0.22	0.63
Max	0.59	2.20	0.85	2.26
Min	0.10	0.01	0.10	0.22
Mean	-0.11	-0.24	0.29	0.92
SD	0.37	0.88	0.56	0.64

11.2 Performance Evaluation of the Novel Registration Approach

The new registration method was tested on LiDAR intensity and optical images. The optical images refer to aerial images, satellite images and Google images. Two datasets were used in these experiences. The 1 m GSD ortho-rectified satellite images by GeoEye, acquired in January 2010, and 1 m GSD intensity images from airborne LiDAR data by Fugro-EarthData from 2009 covering the San Diego, CA, area, represent a typical mix of terrain topography and landscape, including residential areas, roads, and vegetated areas. The 0.2 m GSD high-resolution DMC aerial imagery and 1 m GSD intensity image from LiDAR data by ODOT cover the corridor area of highway I-70 in the Belmont County and highway 161 in Franklin County, OH. In addition, images from Google Earth covering the above-mentioned areas were also used.

Four Google/LiDAR, satellite/LiDAR and aerial/LiDAR intensity image pairs were selected to evaluate the registration performance. The overlap is more than 80% in all cases. The extents of the overlap areas of the test image pairs vary, and are shown in the result tables. The PDF region size is set to 110 pixels. Both affine and perspective models are used in the evaluation, and the RANSAC threshold value was set to 0.5 σ.

Table 17 Test results: Google vs. LiDAR

Google/LiDAR	A	B	C	D
Affine Model Position RMSE [pixel]	1.96	2.2	2.36	2.29
Affine Model Inlier/Matched	39/82	17/54	25/90	21/48
Perspective Model Position RMSE [pixel]	1.22	1.16	1.28	1.15
Perspective Model Inlier/Matched	37/82	18/54	24/90	20/48
Overlap Size [m^2] Width (E) × Height (N)	472×855	581×907	846× 682	231× 435

Table 18 Test results: Satellite vs. LiDAR.

Satellite/LiDAR	E	F	G	H
Affine Model Position RMSE [pixel]	2.19	1.05	1.99	2.44
Affine Model Inlier/Matched	9/28	74/101	35/88	46/87
Perspective Model Position RMSE [pixel]	0.96	0.97	1.22	1.16
Perspective Model Inlier/Matched	9/28	75/101	35/88	44/87
Overlap Size [m^2] Width (E) × Height (N)	324×305	694×347	1299×375	1197× 287

Table 19 Test results: Aerial vs. LiDAR.

Aerial/LiDAR	I	J	K	L
Affine Model Position RMSE [pixel]	1.64	2.16	1.05	1.38
Affine Model Inlier/Matched	40/111	38/94	32/101	38/101
Perspective Model Position RMSE [pixel]	1.4	1.4	1.29	1.29
Perspective Model Inlier/Matched	37/111	37/94	26/101	37/101
Overlap Size [m^2] Width (E) × Height (N)	463×813	460 × 810	477×829	462× 821

Tables 17, 18 and 19 summarize the registration results for the Google/LiDAR, satellite/LiDAR and aerial/LiDAR intensity image pairs, respectively. In all tests, the inliers after RANSAC are more than enough to estimate the affine and perspective models. The RMSE (Root Mean Square Error) of position error is used to judge the registration precision. Similarly to the re-projection error, the position error is computed as the position difference between the matched and transformed positions in the optical image. The RMSE is computed on a pixel basis. The matched points are shown in Figs. 53, 54 and 55.

Figure 53 Registration between Google and LiDAR intensity image pair (A) using perspective transformation.

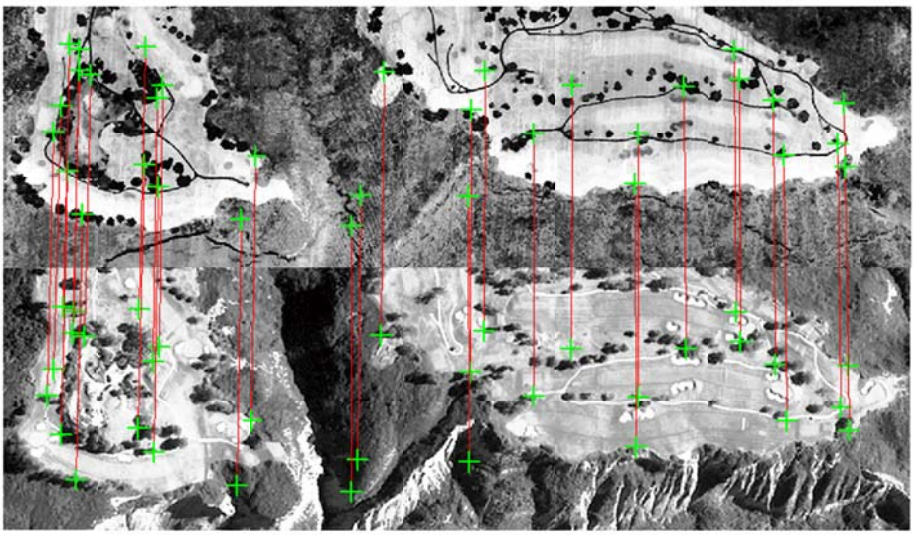

Figure 54 Registration between Satellite and LiDAR intensity image pair (G) using perspective transformation.

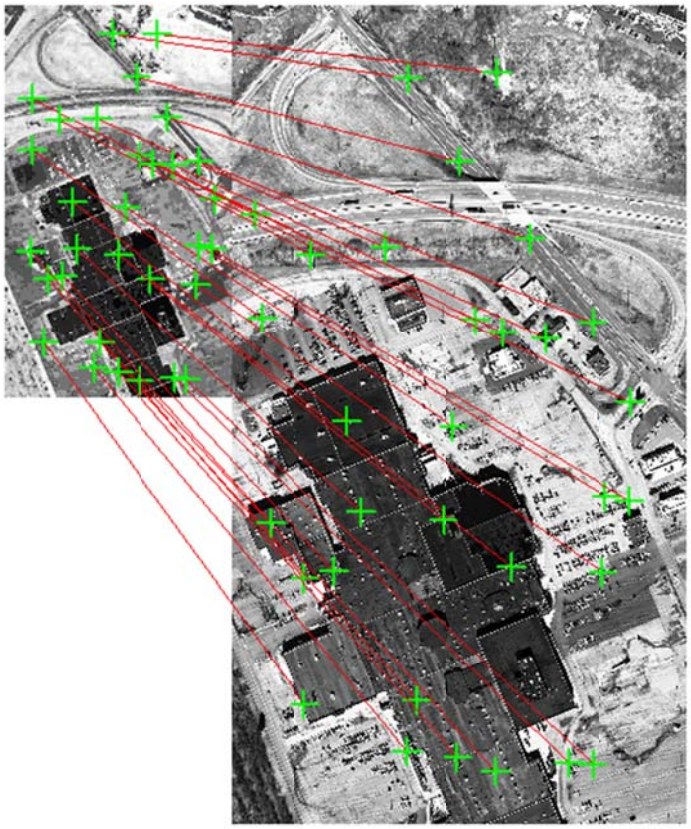

Figure 55 Registration between Aerial and LiDAR intensity image pair (K) using perspective transformation.

11.3 PDBM Samples

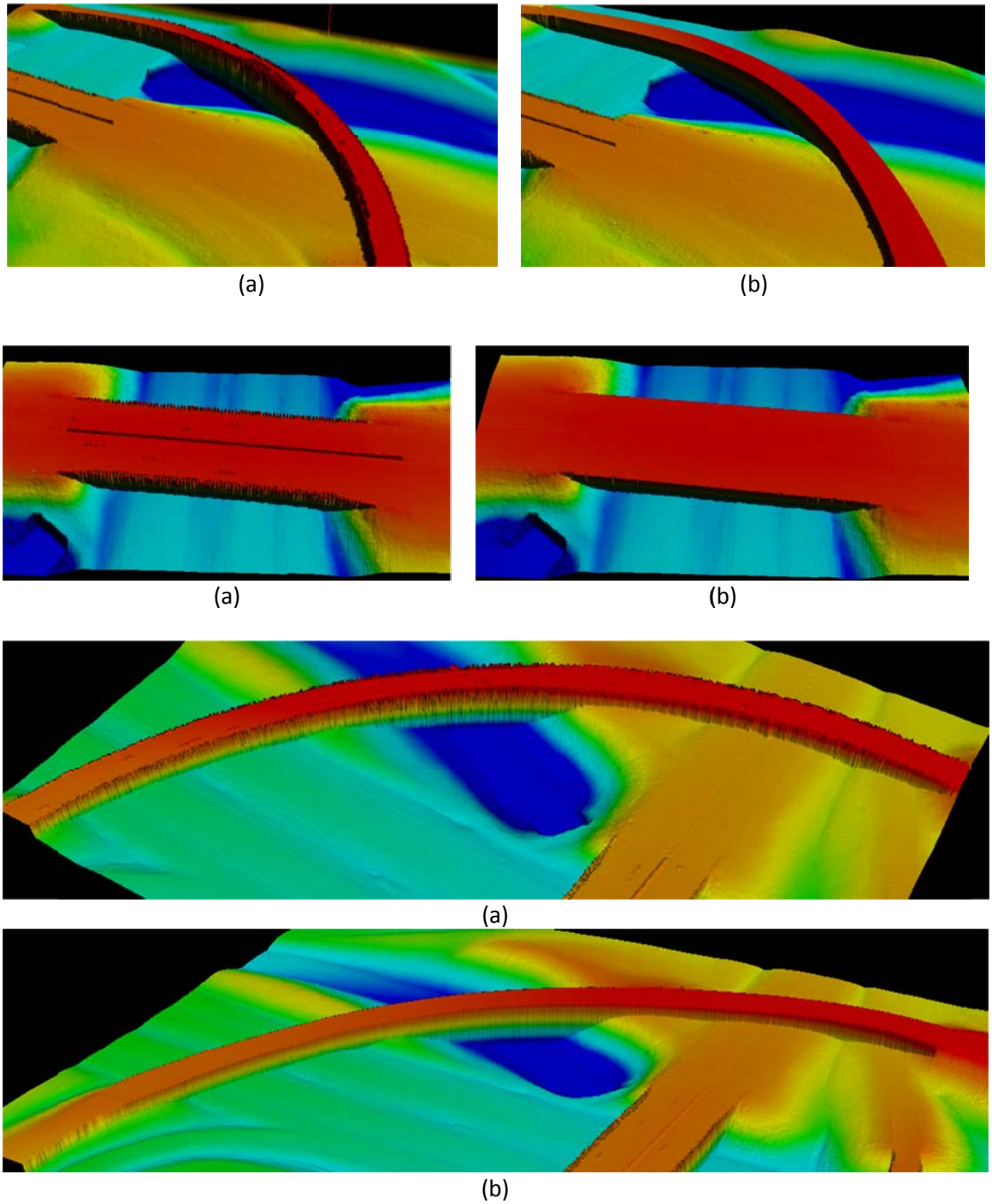

Figure 56 DTM from LiDAR points (a), and PDSM (b).

11.4 Software Modules Developed (digital version)

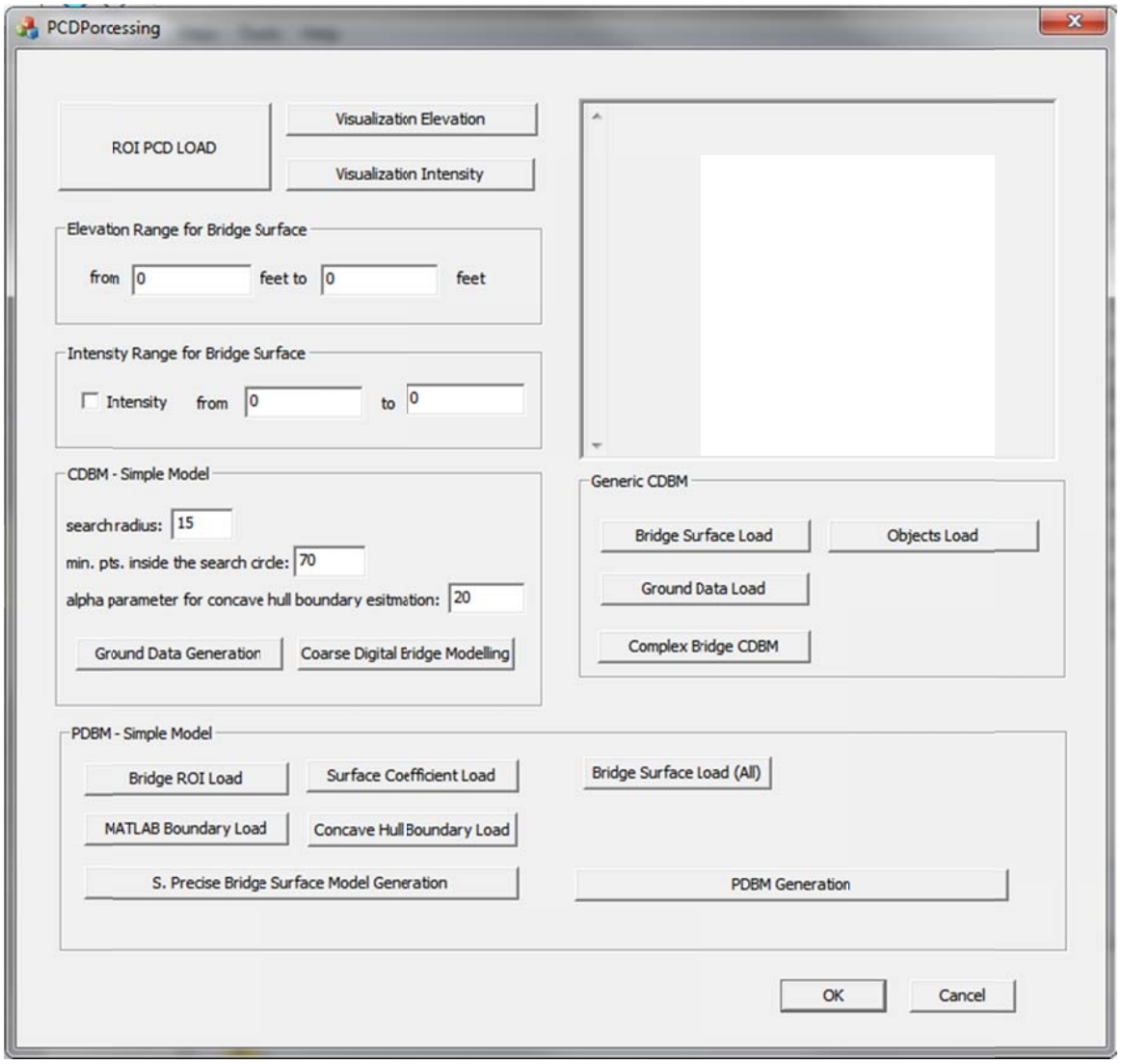

Figure 57 PCDProcessing GUI.

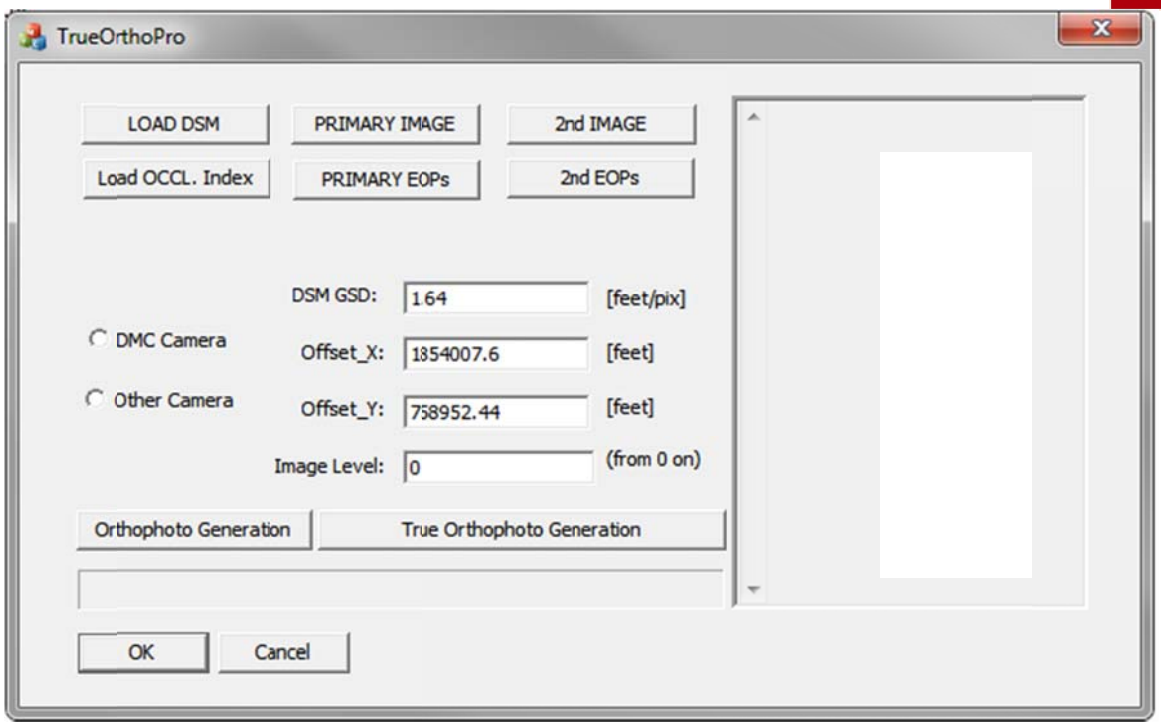

Figure 58 TrueOrthoPro GUI.